DEFENCE S&T TECHNICAL BULLETIN

VOL. 14 NUM. 1 YEAR 2021 ISSN 1985-6571

CONTENTS

Ministry of Defence
Malaysia

SCIENCE & TECHNOLOGY RESEARCH
INSTITUTE FOR DEFENCE (STRIDE)

AIMS AND SCOPE

The Defence S&T Technical Bulletin is the official journal of the Science & Technology Research Institute for Defence (STRIDE). The journal, which is indexed in, among others, Scopus, Index Corpenicus, ProQuest and EBSCO, contains manuscripts on research findings in various fields of defence science & technology. The primary purpose of this journal is to act as a channel for the publication of defence-based research work undertaken by researchers both within and outside the country.

WRITING FOR THE DEFENCE S&T TECHNICAL BULLETIN

Contributions to the journal should be based on original research in areas related to defence science & technology. All contributions should be in English.

PUBLICATION

The editors' decision with regard to publication of any item is final. A manuscript is accepted on the understanding that it is an original piece of work that has not been accepted for publication elsewhere.

PRESENTATION OF MANUSCRIPTS

The format of the manuscript is as follows:

a) Page size A4
b) MS Word format
c) Single space
d) Justified
e) In Times New Roman, 11-point font
f) Should not exceed 20 pages, including references
g) Texts in charts and tables should be in 10-point font.

Please e-mail the manuscript to:

1) Gs. Dr. Dinesh Sathyamoorthy (dinesh.sathyamoorthy@stride.gov.my)
2) Dr. Mahdi bin Che Isa (mahdi.cheisa@stride.gov.my)

The next edition of the journal (Vol. 14, Num. 2) is expected to be published in November 2021. The due date for submissions is 4 August 2021. **It is strongly iterated that authors are solely responsible for taking the necessary steps to ensure that the submitted manuscripts do not contain confidential or sensitive material.**

The template of the manuscript is as follows:

TITLE OF MANUSCRIPT

Name(s) of author(s)

Affiliation(s)

Email:

ABSTRACT

Contents of abstract.

Keywords: *Keyword 1; keyword 2; keyword 3; keyword 4; keyword 5.*

1. TOPIC 1

Paragraph 1.

Paragraph 2.

1.1 Sub Topic 1

Paragraph 1.

Paragraph 2.

2. TOPIC 2

Paragraph 1.

Paragraph 2.

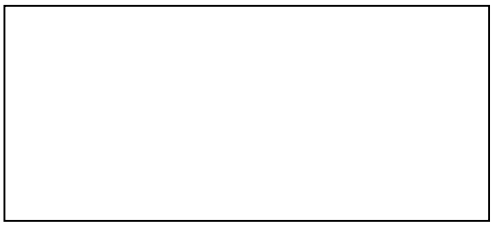

Figure 1: Title of figure.

Table 1: Title of table.

Content	Content	Content
Content	Content	Content
Content	Content	Content
Content	Content	Content

Equation 1 (1)
Equation 2 (2)

REFERENCES

Long lists of notes of bibliographical references are generally not required. The method of citing references in the text is 'name date' style, e.g. 'Hanis (1993) claimed that...', or '…including the lack of interoperability (Bohara *et al.*, 2003)'. End references should be in alphabetical order. The following reference style is to be adhered to:

Books

Serra, J. (1982). *Image Analysis and Mathematical Morphology*. Academic Press, London.

Book Chapters

Goodchild, M.F. & Quattrochi, D.A. (1997). Scale, multiscaling, remote sensing and GIS. *In* Quattrochi, D.A. & Goodchild, M.F. (Eds.), *Scale in Remote Sensing and GIS*. Lewis Publishers, Boca Raton, Florida, pp. 1-11.

Journals / Serials

Jang, B.K. & Chin, R.T. (1990). Analysis of thinning algorithms using mathematical morphology. *IEEE T. Pattern Anal.*, **12**: 541-550.

Online Sources

GTOPO30 (1996). *GTOPO30: Global 30 Arc Second Elevation Data Set*. Available online at: http://edcwww.cr.usgs.gov/landdaac/gtopo30/gtopo30.html (Last access date: 1 June 2009).

Unpublished Materials (e.g. theses, reports and documents)

Wood, J. (1996). *The Geomorphological Characterization of Digital Elevation Models*. PhD Thesis, Department of Geography, University of Leicester, Leicester.

APPLICATION OF DESIGN OF EXPERIMENT TECHNIQUE FOR OPTIMISATION OF LABORATORY SCALE SODA LIME PROCESSING

Mahdi Che Isa*, Nik Hassanuddin Nik Yusoff, Mohd Subhi Din Yati, Mohd Moesli Muhammad, Hasril Nain & Azmahani Sulaiman

Maritime Technology Division, Science & Technology Research Institute for Defence (STRIDE), Ministry of Defence, Malaysia

*Email: mahdi.cheisa@stride.gov.my

Design of experiments (DoE) is a systematic technique used to ensure the generation of valid, defensible and supportable engineering conclusions. In the DoE method, some statistical-based models can be proposed in the pre-stages of physical models. The statistical / numerical relations are used to predict the behaviour of the investigated systems as a function of various operating parameters. This paper discusses the application of DoE for analysing the influence of four processing parameters, which are hydration time (A), granules size (B), water content (C) and material bulk density (D) on the absorbency efficiency of soda lime material. The effect of these parameters on chemical activity was studied using a two level factorial design. It was found that all the soda lime preparation parameters had significant influence on the absorbency efficiency. Higher hydration time (A = 180 min) and smaller granule size (B = 1 mm) gave a positive effect on the percentage of absorbency efficiency. The presence of high water content (up to 25%) and higher bulk density (1.2 g/cm^3) also produced soda lime with higher absorbency efficiency. Soda lime with the best absorbency (29%) can be obtained by combining the optimised processing parameters, which are longer hydration time, high water content, bulk density and low granule size of soda lime materials.

Keywords: *Soda lime; design of experiment (DoE); absorbency efficiency; calcium oxide (CaO); carbon dioxide (CO_2).*

1. INTRODUCTION

As living and working environments all over the world are becoming more restrictive, mitigating the emission and control of atmospheric pollution has become an imperative international issue. Air quality issues caused by greenhouse effects, industrialisation processes and human activities have become a global concern and need serious attention from the point of an environmental and economic issue, advance in scientific research, and international policy regulation (Adams & Horst, 2003; Afroz *et al*., 2003; Barnett, 2003; Semazzi, 2003; Monks *et al*., 2009; Tollefsen *et al*., 2009). For example, carbon dioxide (CO_2) emissions into the atmosphere is widely known to be an important contributor to global warming. CO_2 emission was recorded at 36.4 billion metric tonnes in 2019 as compared to 24.4 billion metric tonnes in 1999, with this figure increasing over time (United Nations, 2010; Friedlingstein *et al*., 2019). In the 1970s, CO_2 concentration in the atmosphere increased by 1.3 ppm per year, with this figure increasing to 2.2 ppm per year by 2007. Scientists predicted that the safe value for CO_2 concentration in the atmosphere is 350 ppm, while the current CO_2 concentration of the atmosphere is more than 410 ppm (Canadell *et al*., 2008; Global Monitoring Laboratory, 2021).

In order to contain the increasing CO_2 concentration level, the most viable solution is to find cost-effective ways to capture or store CO_2 before it is released into the atmosphere. Currently, there are many technologies to capture or reduce the level of CO_2, such as capture and storage, membrane technology, aqueous amine, solid soda lime process, chemisorption, and physical absorption (Corti *et al*., 2004; Aaron & Tsouris, 2005; Loo *et al*., 2007; Pennline *et al*., 2008; Yang *et al*., 2008; Choi *et al*., 2009; Ma *et al*., 2009; Wilson *et al*., 2009; Abass, 2010; Duke *et al*., 2010; Herzog, 2011; Yu *et al*., 2017). The removal of CO_2 with solid adsorbents may be a more attractive approach than

conventional liquid absorbents because it could reduce the cost associated with the capture step (Khraisheh *et al*., 2020).

However, the success of this approach is dependent on the development of an easily regenerated and durable adsorbent with high CO_2 selectivity and adsorption capacity (Arenillas *et al*., 2005; Drage *et al*., 2007). Early studies have shown that materials such as calcium hydroxide ($Ca(OH)_2$) or calcium oxide (CaO) can play an important role in the absorption of CO_2 (Blum *et al*., 1952). These metal oxide/ hydroxide based sorbents have been the most promising candidates for CO_2 capture (Gupta & Fan, 2002; Manovic & Anthony, 2007; Grasa *et al*., 2008; Li *et al*., 2015). Soda lime is a granular mixture of $Ca(OH)_2$ and sodium hydroxide, and is categorised as a solid absorbent that contains carefully controlled level of water that will capture CO_2 gas leading to the formation of calcium carbonate ($CaCO_3$) (Mazurek, 2005). Lin *et al*. (2004) found that carbonation occurred via the hydroxide under the conditions of interest, which increased the reactivity of the absorbent.

Design of experiments (DoE) was introduced by Fisher (1935), who described the basic problem of experiment design as deciding what pattern of factors combination (the design points) will best reveal the properties of the response and how this response is influenced by the factors. It is a strategic, enabling methodology to improve process yields and product quality. The technique of DoE is an important link between the experimental and modelling world. It aims at obtaining the maximum information from an experimental apparatus being modelled by devising experiments that will yield the most informative data, in a statistical sense, for use in parameter estimation and model validation.

Before collecting the data, an experiment is designed, whereby it is decided how the system will be perturbed (initial conditions, which input variables are modified, when and how, etc.), and where, how and when the experimenter will observe the phenomena under investigation (which variables are measured, type and location of sensors, sampling schedules, etc.). It is a systematic route that may be followed so as to find solutions to industrial process problems with greater objectivity by means of experimental and statistical techniques (Coleman & Montgomery, 1993; Antony *et al*., 1998). Recently, the DoE procedure has been used to systematically investigate process variables or product variables that influence the quality of products. It is possible to identify the process conditions and product components that influence product quality and costs, which in turn enhance the product manufacturability, quality, reliability and productivity (Franceschini & Macchietto, 2008; Moseson *et al*., 2012).

The aim of this study is to apply DoE to simplify the experimental process, especially by minimising the number of test runs and by maximising the accuracy of the results. DoE will be used to determine the significant factors or parameters affecting laboratory scale soda lime processing and to highlight some possible interactions between the various processing parameters. In this study, a two level factorial design is selected to simultaneously study the effects of four numerical soda lime preparation variables, which are hydration time (A), granules size (B), water content (C) and bulk density of materials (D), on carbon dioxide absorbency efficiency prepared from local industrial grade CaO. An empirical model will be developed to correlate the absorbency efficiency to the soda lime preparation parameters. The reactivity of soda lime (absorbency efficiency) is also tested for its capability in absorbing CO_2.

2. MATERIALS & METHODS

2.1 Physical and Chemical Analyses

The raw material used for soda lime preparation was industrial grade CaO provided by CAO Industries, Rawang, Selangor, Malaysia. The phases present in the material were determined using an X-ray diffractometer (XRD) (Bruker D8-Advanced) housed at the School of Applied Physics, National University of Malaysia (UKM). The diffractogram was generated using a Cu Kα (λ = 1.543 Å) radiation source at scanning rate of 0.002 °/s with 2θ from 20 to 60º. The elemental composition of

the material was analysed using a wavelength dispersive X-ray fluorescence (XRF) spectrometer (Bruker SP 4 Pioneer, WDXRF) equipped with an Rh X-ray tube and 4 kW generator. The X-ray generator was operated at voltage of 20 - 50 kV and current of 5 - 20 mA. In order to prepare the XRF-pellets, a small metallic sample holder made of aluminium with diameter of 3 cm was used. The pellets were pressed for 30 s with pressure of 10 tons/cm^2 using a Specac hydraulic press machine (Isa *et al*., 2012). From this process, the total mass of each pellet gained was 10.8 g. Quantitative calculations were made using the accompanied software. The results of the analysis were expressed in weight percentage (*wt.%*). The chemical composition and main phase presence of the material are shown in Table 1 and Figure 1 respectively.

Table 1: Chemical composition of the raw material for soda lime preparation.

CaO	MgO	C	SiO_2	Fe_2O_3	Al_2O_3	Others
92.380	3.556	3.125	0.348	0.259	0.163	0.169

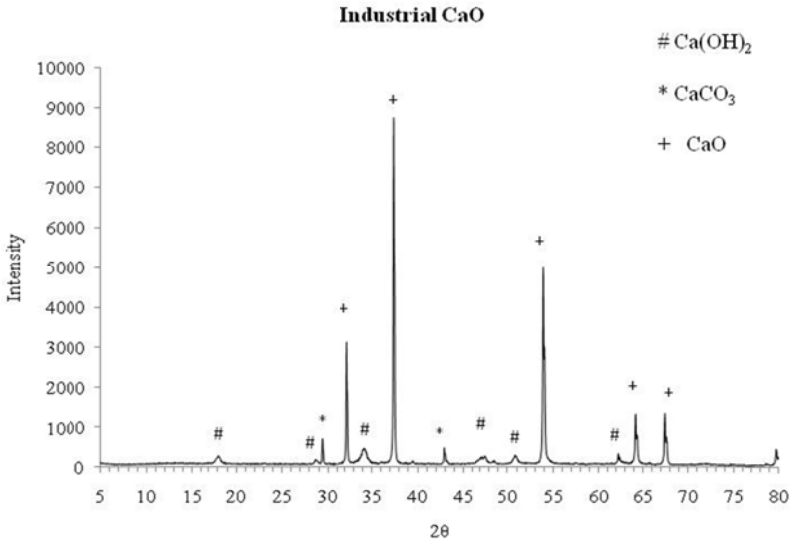

Figure 1: XRD analysis peaks of raw material for soda lime preparation.

2.2 Soda Lime Preparation

Granulated soda lime was prepared by mixing 1,000 g of CaO and 3 L of water at 27 °C. Upon stirring, the temperature of the slurry was increased to about 80 °C. The slurry was then left at room temperature for 30-180 min and then extruded to form granulated form, heated at 120 °C for 12 h. The adsorbent in granulated form were then crushed and sieved to produce the required particle size range (1 and 5 mm). The hydration period and the use of CaO as the starting materials were varied based on DoE.

2.3 Design of Experiments, Model Fitting and Statistical Analysis

The soda lime granules were prepared using the water hydration method by varying the adsorbent preparation variables using a two level factorial design. Four soda lime preparation variables were studied, which are hydration time (A), granules size (B), water content (C) and bulk density of granules (D), as shown in Table 2. For each categorical parameters, a half fractional factorial design for the four numerical parameters, consisting of eight factorial points (coded as −1 and +1), was employed, which indicated that eight experiments were required to be conducted.

Table 2: The independent parameters and values used in this study.

Parameters	Code	(unit)	Low level (−1)	High level (+1)
Hydration time	A	min	30	180
Granules size	B	mm	1	5
Water content	C	%	10	25
Density (bulk)	D	g/cm^3	0.5	1.2

The complete design matrix of the experiments employed and results are given in Tables 3 and 4 respectively. The experiment sequence was randomised in order to minimise the effects of uncontrolled factors. The response in Table 4 was used to develop an empirical model that correlates to the chemical activity or absorbency of the soda lime preparation parameters. Design Expert 6.0.6 (STAT-EASE Inc., Minneapolis, USA) was used for regression analysis of the experimental data to fit the second-degree polynomial equation and also for evaluation of the statistical significance of the equation developed.

Table 3: Experimental design matrix.

Samples code (run)	Soda lime preparation parameters (actual values)			
	Hydration time (min)	Granule size (mm)	Water content (%)	Bulk density (g/cm3)
1	180	5.0	10.0	0.50
2	180	1.0	10.0	1.20
3	180	1.0	25.0	0.50
4	30	1.0	25.0	1.20
5	30	1.0	10.0	0.50
6	30	5.0	25.0	0.50
7	30	5.0	10.0	1.20
8	180	5.0	25.0	1.20

Table 4: Experimental results.

Samples code (run)	Soda lime preparation parameters (coded values)				
	A	B	C	D	Absorbency efficiency (%)
1	1	1	-1	-1	21.13
2	1	-1	-1	1	28.56
3	1	-1	1	-1	25.37
4	-1	-1	1	1	20.48
5	-1	-1	-1	-1	18.23
6	-1	1	1	-1	21.56
7	-1	1	-1	1	26.17
8	1	1	1	1	24.39

2.4 Carbon Dioxide Absorption Efficiency Study

In order to determine the chemical absorbency of the sample, an amount of 33.3 g is placed inside a U-tube with 10 g of calcium chloride ($CaCl_2$) to trap the moisture produced by the neutralisation reaction and to simulate dry environments. 99.5% purified CO_2 gas was injected / inserted through the U-tube at the rate of 1,000 ml per min for 5 min to allow it to cool down. The initial and final weights of the U-tube were recorded to determine the permissible quantity of CO_2 that had been absorbed by the soda lime.

3. RESULTS AND DISCUSSION

3.1 Development of Empirical Model Equation

The complete design matrix and absorbency efficiency responses at various soda lime preparation variables are listed in Tables 3 and 4. As can be seen from Table 4, the absorbency efficiency was in the range of 18.23–28.56%. The absorbency efficiency responses in the table were correlated with the four soda lime preparation variables and the data obtained from the tests that were carried out. The coefficients of the empirical model equation and their statistical significance were determined and evaluated. The final empirical model in terms of coded value after excluding the insignificant terms (identified using Students' *t*-test) is presented as:

$$\text{Absorbency efficiency} = 23.24 + 1.63\text{A} + 1.66\text{D} - 2.18\text{AB} \quad (1)$$

where the measured response is the predicted absorbency efficiency (%), and A, B and D are the coded values of the adsorbent preparation variables. The positive signs in front of the terms indicate synergistic effect to the soda lime absorbency efficiency. The adequacy of the model was checked with analysis of variance (ANOVA) as shown in Table 5. The significance of the empirical model was indicated by the Fisher variance ratio (*F*-test value), which is a statistical means of measuring how well the empirical model describes the variation in the data about its mean. The greater the *F*-value is from unity, the more certain it is that the empirical model adequately explains the variation in the data about its mean and the estimated significant terms of the soda lime preparation variables are real (Lazic, 2004; Montgomery, 2005). Based on a 90% confidence level, Model *F*-value of 85.07 implies that the model is significant. There is only a 0.20% chance that Model *F*-Value could occur due to noise. Values of Prob > *F* of less than 0.05 indicate model terms are significant. In this case, A, hydration time; D, bulk density; and AB, interaction between hydration time-granule size are significant model terms or processing parameters. Values greater than 0.1 indicate that the model terms are not significant.

Table 5: Analysis of variance (ANOVA) for the empirical model and individual coefficients.

Source	Sum of squares	Degrees of freedom	Mean of square	*F*-test	Prob > *F*
Model	82.02	4	20.50	85.07	0.0020
A	21.16	1	21.16	87.79	0.0026
D	22.14	1	22.14	91.88	0.0024
AB	37.98	1	37.98	157.57	0.0011
AC	0.74	1	0.74	3.06	0.1784
Residual	0.72	3	0.24		

The quality of the model was further evaluated from the correlation coefficients (*R*). Pred R^2 of 0.9379 is in reasonable agreement with the Adj R^2 of 0.9796. The predicted and adjusted R^2 values are within 0.20 of each other, which indicates that there is no problem with either the data or model. The high value of *R* (close to 1) justifies an excellent correlation between the predicted and experimental absorbency tests. The fitness of the model was expressed by the coefficient of determination (R^2) and

its value was found to be 0.9913. It implies that the total variation in the absorbency efficiency responses could be explained by the empirical model developed as shown in Equation 1. From these statistical tests, it was found that the model is adequate for predicting the absorbency efficiency within the range of the variables studied.

3.2 Effects of Adsorbent Preparation Variable

The model developed in this study was found to have a maximum point of the response (29% absorbency efficiency) at the maximum range of its variables. Thus, the model developed will be utilised to construct three-dimensional response surfaces to facilitate the study of the effects of the various adsorbent preparation variables on the absorbency efficiency. Figure 2 shows the response surface of CO_2 absorbency efficiency with varying hydration time (A), granule size (B), water content (C) and bulk density (D) of soda lime materials prepared using CaO and distilled water. The soda lime materials prepared using longer hydration time, higher water content, smaller granule size and higher density produced adsorbent with the highest absorbency efficiency (29%) as compared to adsorbent prepared from short hydration time, lower water content, bigger granule size and low density (19%).

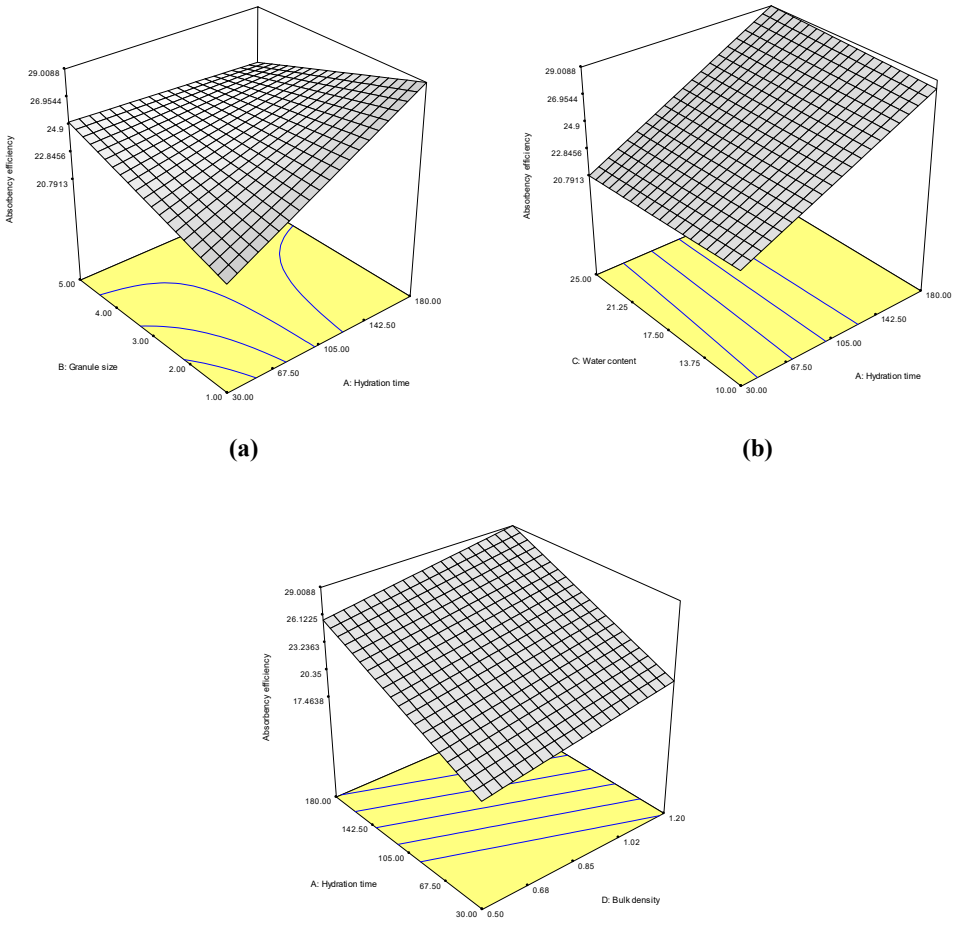

Figure 2: Response surface plots of absorbency efficiency for soda lime materials: (a) Granules size and hydration time. (b) Water content and hydration time. (c) Bulk density and hydration time.

The results in Table 4 show that the soda lime preparation variables have great effect on the absorbency efficiency. The highest absorbency capacity of the soda lime materials within the studied variables is 29%. These results illustrate that there is a great possibility in improving the absorbency of soda lime materials with proper selection of soda lime preparation variables. The soda lime granule size has been reported play a key factor in obtaining soda lime with high chemical activity (Carey *et al*., 1983; NATO, 2006).

The empirical model shown in Equation 1 shows that hydration time (A), granule size (B) and bulk density of soda lime materials (D) have a significant effect on absorbency capacity. Besides that, the effect of interaction between variables A and B also affects the absorbency capacity significantly. Shunji *et al*. (2003) reported that the addition of water vapour (H_2O) can promote the formation of the reactive species for soda lime prepared from CaO. More water content will promote the formation of reactive species by enhancing the reactivity of the $Ca(OH)_2$ (Shih *et al*., 1999; Carlos *et al.*, 2016)

Figure 2 shows that the absorbency efficiency of soda lime increases with higher hydration time, bulk density and smaller granule size. Apart from that, Equation 1 clearly shows that the coefficient for interaction between hydration time (A) and granule size (B) is the highest among the others. Based on these findings, it is possible to conclude that the effect of hydration time on the absorbency efficiency of soda lime is the most significant. In other words, the hydration time is the rate limiting factor for the formation of the reactive species with a higher absorption capacity.

Water content and bulk density of material also have positive effect on the surface area of the soda lime absorbency, as shown in Figures 2(b) and 2(c). From Table 4, at higher water content (C = 25%) the absorbency lies between 20.48 to 25.37%. However, the absorbency does not change significantly at lower water content (C = 10), where the efficiency only lies between 18.23 to 28.56%. The presence of water generally determines the amount of CaO to form the reactive species. At higher water content, there will be more CaO available to react with water to form the reactive species. This will produce a significant positive effect on the absorbency of the soda lime. The interaction between parameters A, B, C and D can also be seen clearly in Figure 2.

The effect of granule size, water content and bulk density on the absorbency efficiency were more pronounced at higher hydration period as compared to lower hydration period. This is because, at a lower hydration period, there is insufficient time for the chemical reaction to proceed completely. In other words, the hydration period becomes the limiting factor for the formation of the reactive species in the soda lime. Therefore, the amount of CaO available for the chemical reaction is not crucial in determining the total amount of reactive species formed in the soda lime. However, at a higher hydration period, there will be sufficient time for the chemical reaction to proceed completely (Yin *et al*., 2012). Thus, the use of higher water content and hydration period can produce more reactive species in the soda lime materials leading to higher absorbency efficiency when prepared with smaller granule size and higher density.

3.3 XRD Analysis

Figure 3 shows the XRD diffractograms for both samples No. 2 (28% efficiency) and No. 5 (18% efficiency) in the conditions of as-prepared and after reaction with CO_2. The absence of the starting material, CaO in the fresh samples of No. 2 and No. 5 shows that the starting material reacted completely to form reactive species of portlandite. Both samples showed XRD peaks that can be ascribed to portlandite or calcium hydroxide ($Ca(OH)_2$), and calcite or calcium carbonate ($CaCO_3$).

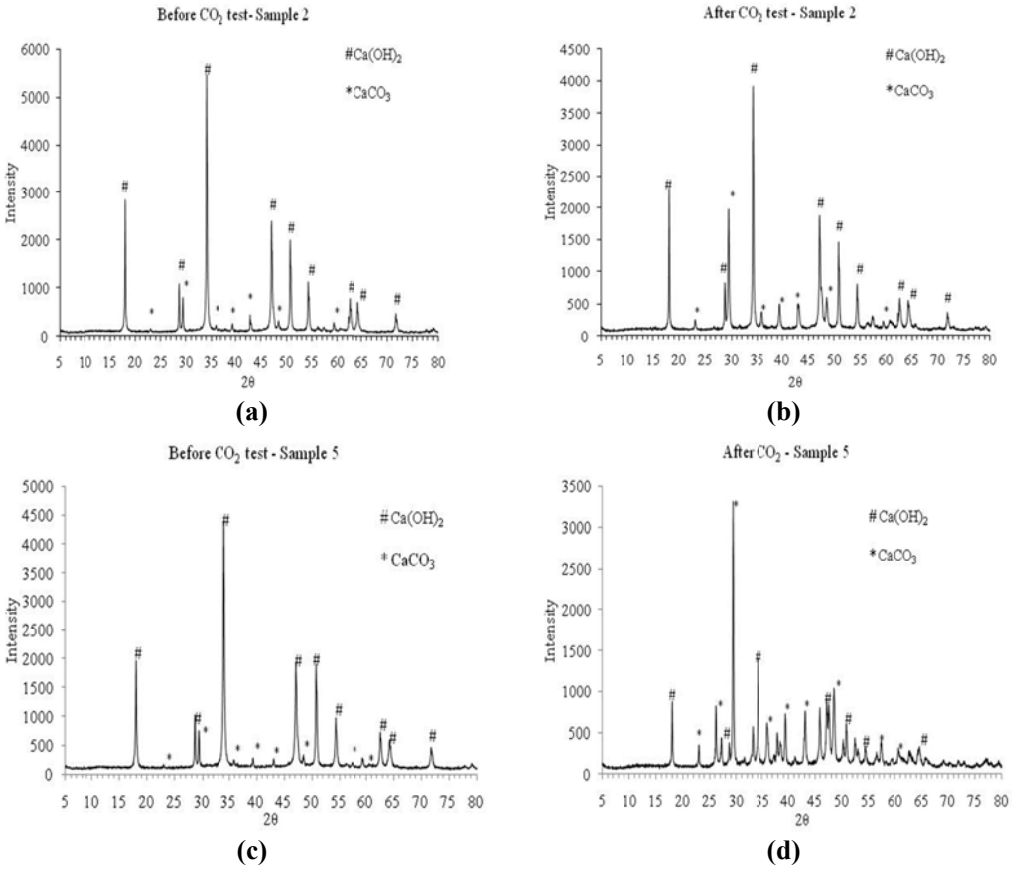

Figure 3: XRD analysis peaks of: (a) Fresh soda lime sample No. 2. (b) Sample No. 2 after CO_2 activity test. (c) Fresh soda lime sample No. 5. (d) Sample No. 5 after CO_2 activity test.

In the as-prepared soda lime materials (samples No. 2 and No. 5), $CaCO_3$ peaks were detected in both samples due to the reaction of $Ca(OH)_2$ with CO_2 presence in the air. In general, $Ca(OH)_2$ absorbs CO_2 from the atmosphere, giving the transition to $CaCO_3$ in the presence of water or humidity of 20–100% RH. In addition, the longer the soda limes were exposed to humid environment, the less the amount of portlandite phase and the more the amount of calcite phase were formed. The XRD patterns for the samples after exposed to CO_2 (Figures 3(b) and 3(d)) shows high intensity peaks for $CaCO_3$ due to the carbonisation process.

After being exposed to CO_2, the absorption process of CO_2 into the reactive species ($Ca(OH)_2$) resulted in low intensity peaks for $Ca(OH)_2$ and high intensity peaks for $CaCO_3$. Unreacted phase of $Ca(OH)_2$ from the soda lime was still detected based on the presence of XRD peaks. The formation of $CaCO_3$ in large quantity (based on the XRD intensity peaks) in the soda lime after the test showed that the soda lime contains reactive species that is effective in absorbing CO_2 (Liang *et al*., 2004). Similar results were also obtained from the soda lime sample No. 5, which were detected before and after the test (Figures 3(c) and 3(d)). The difference is only at the intensity peaks, which indicates qualitatively less formation of $CaCO_3$ for sample No. 5, which recorded lower absorbency efficiency. The XRD results is in a good agreement with the DoE model, which shows that absorbency efficiency is influenced by hydration time, granules size, water content and bulk density of materials.

4. CONCLUSION

As discussed in this article, DoE can be first applied to organise the tests in a rational way to save time during the experimental design and characterisation stages for conducting experiments in the processing of soda lime material. The DoE approach leads to simple and precise models that highlight the impacts of the processing parameters, in this case, hydration time, granule size, water content and bulk density, on absorbency efficiency of soda lime, and detect possible interactions between the processing parameters. A central composite design was used to develop an empirical model that correlates the absorbency efficiency and preparation parameters, which would be very useful for optimisation purposes in producing high absorbency efficient soda lime materials. This study also showed that soda lime for scrubbing CO_2 in the atmosphere was successfully prepared using local industrial grade CaO as a starting material and water through the hydration process. The maximum absorbency efficiency of soda lime obtained in this study was 29% with bulk density of 1.2 g/cm^3, water content of 25% and granule size of 1 mm, and prepared with maximum hydration time 180 min.

ACKNOWLEDGEMENT

The authors would like to thank the Government of Malaysia for financing this R&D project. We also wish to thank the Faculty of Science & Technology, National University of Malaysia (UKM) for conducting the XRD test. We are pleased to acknowledge the cooperation and technical assistance given by STRIDE's officers and staff in improving the quality of this manuscript.

REFERENCES

Aaron, D. & Tsouris, C. (2005). Separation of CO_2 from flue gas: A review. *Sep. Sci. Tech.*., **40**: 321–348

Abass, A.O. (2010). CO_2 capture and separation technologies for end-of-pipe applications – A review. *Energy*, **35**: 2610–2628

Adams, R.M. & Horst, R.L. (2003). Future directions in air quality research: economic issues. *Env. Int.*, **29**: 289-302

Afroz, R., Hassan, M.N. & Ibrahim, N.A. (2003). Review of air pollution and health impacts in Malaysia. *Env. Res.*, **92**: 71-77

Antony, J., Kate, M. & Frangou, A. (1998). A strategic methodology to the use of advanced statistical quality improvement techniques. *TQM Mag*., **10**: 169–176

Arenillas, A., Smith, K.M., Drage, T.C. & Snape, C.E. (2005). CO_2 capture using some fly ash-derived carbon materials. *Fuel*, **84**: 2204–2210

Barnett, J. (2003). Security and climate change. *Global Env. Change*, **13**: 7-17.

Blum, H.A., Stutzman, L.F. & Dodds. W. S. (1952). Gas absorption – absorption of carbon dioxide from air by sodium and potassium hydroxides. *Ind. Eng. Chem*., **44**: 2969–2974

Canadell, P., Ciais, P, Conway, T, Field, C.B, Quéré, C.L, Houghton, R.A, Marland, Raupach, G, (2008). *Recent Carbon Trends and the Global Carbon Budget*. Global Carbon Project, Canberra, Australia.

Carey, R., Gomezplata, A. & Sarich, A. (1983). An overview into submarine CO_2 scrubber development. *Ocean Eng.*, **10**: 227-233.

Carlos, R.N., Irene, V. & Encarnacion, R.A. (2016). Kinetics and mechanism of calcium hydroxide conversion into calcium alkoxides: Implications in heritage conservation using nanolimes. *Langmuir*, **32:** 5183−5194.

Choi, W.J., Seo, J.B., Jang, S.Y., Jung, J. H. & Oh, K.J. (2009). Removal characteristics of CO_2 using aqueous MEA/AMP solutions in the absorption and regeneration process. *J. Env. Sci.*, **21**: 907-913

Coleman, D.E. & Montgomery, D.C. (1993). A systematic approach to planning for designed industrial experiment. *Technometrics*, **35**: 1–12

Corti, A., Fiaschi, D. & Lombardi, L. (2004) Carbon dioxide removal in power generation using membrane technology. *Energy*, **29(12–15):** 2025-2043

Drage, T. C., Arenillas, A. M, Smith, K. M., Pevida, C., Piippo, S. & Snape, C. E. (2007). Preparation of carbon dioxide adsorbents from the chemical activation of urea–formaldehyde and melamine–formaldehyde resins. *Fuel*, **86**: 22–31

Duke, M., Ladewig, B., Smart, S., Rudolph, V. & Diniz da Costa. J. (2010). Assessment of postcombustion carbon capture technologies for power generation. *Front. Chem. Eng. China*, **4**: 184–195

Fisher, R.A. (1935). *The Design of Experiments*. Oliver & Boyd, Edinburgh

Franceschini, G. & Macchietto, S. (2008). Model-based design of experiments for parameter precision: State of the art. *Chem. Eng. Sci.*, **63**: 4846-4872

Friedlingstein, P. *et al.* (2019). Global Carbon Budget 2019. *Earth Syst. Sci. Data*, **11**: 1783–1838

Global Monitoring Laboratory (2021). Global Monthly Mean CO_2, National Oceanic & Atmospheric Administration, Earth System Research Laboratory (NOAA/ESRL) Available online at: http://www.esrl.noaa.gov/gmd/ccgg/trends/global.html (Last access date: 2 March 2021)Grasa, G. S., Abanades J. C., Alonso M. & González B. · (2008). Reactivity of highly cycled particles of CaO in a carbonation/calcination loop. *Chem. Eng. J.*, **137**: 561–567

Gupta, H. & Fan, L. S. (2002). Carbonation−Calcination cycle using high reactivity calcium oxide for carbon dioxide separation from flue gas. *Ind. Eng. Chem. Res.*, **41:**4035–4042

Herzog, H.J. (2011). Scaling up carbon dioxide capture and storage: From megatons to gigatons *Energy Eco.*, **33:** 597-604

Isa, Mahdi Che, Nik Hassanudin Nik Yusof. Mohd Subhi Din Yati, Mohd Moesli Muhammad, Nor Afizah Salleh, Mohd Fauzy Mohd Nor, Azmi Minal, Hasril Nain & Irwan Mohd Nor (2012). Characterisation of carbon dioxide absorbent material for enclosed space applications. *Defence S&T Tech. Bull.,* **5**: 1-10.

Khraisheh, M., Almomani, F. & Walker, G. (2020). Solid sorbents as a retrofit technology for CO_2 removal from natural gas under high pressure and temperature conditions. *Sci. Rep.*, **10:** 269

Lazic, Z. R. (2004). *Design of Experiments in Chemical Engineering: A Practical Guide*. Wiley VCH, Weinheim, Germany

Li, Z.,Wang, Y.,Yao, H. & Lin, S. (2015). Novel CO_2 sorbent: $Ca(OH)_2$ with high strength, *Fuel Process. Technol.*, **131**: 437-442

Liang, Y., Harrison, D.P., Gupta, R.P., Green, D.A. & McMichael, W.J. (2004). Carbon dioxide capture using dry sodium-based sorbents, *Energ. Fuel*, **18**: 569–575.

Lin, S., Harada, M., Suzuki, Y. & Hatano. H. (2004). Continuous experiment regarding hydrogen production by coal/CaO reaction with steam (I) gas products. *Fuel*, **83**: 869–874

Loo, S., van Elk, E.P. & Versteeg, G.F. (2007). The removal of carbon dioxide with activated solutions of methyl-diethanol-amine *J. Petrol. Sci. Eng.*, **55**: 135-145

Ma, X., Wang, X. & Song, C. (2009). Molecular basket sorbents for separation of CO_2 and H_2S from various gas streams. *J. Am. Chem. Soc.*, **131**: 5777–5783

Manovic, V. & Anthony, E. J. (2007). Steam reactivation of spent CaO-based sorbent for multiple CO_2 capture cycles. *Environ. Sci. Technol.*, **41**: 1420–1425

Mazurek, W. (2005). Submarine atmosphere. In Hocking, M.B. & Hocking, D. (Eds.), *The Handbook of Environmental Chemistry: Vol. 4, Part H (Air Quality in Airplane Cabins and Similar Enclosed Spaces)*. Springer-Verlag Berlin Heiderberg, Germany, pp. 351-382.

Monks, P.S., Granier, C., Fuzzi, S., Stohl, A., Williams, M.L., Akimoto, H., Amann, M., Baklanov, A., Baltensperger, U., Bey, I., Blake, N., Blake, R.S., Carslaw, K., Cooper, O.R., Dentener, F., Fowler, D., Fragkou, E., Frost, G.J., Generoso, S. & Ginoux, P. (2009). Atmospheric composition change – global and regional air quality. *Atmos. Env.*, **43**: 5268-5350

Montgomery, D. C. (2005). Design and analysis of experiments, John Wiley and Sons, New York

Moseson, A. J., Moseson, D. E. & Barsoum, M. W. (2012). High volume limestone alkali-activated cement developed by design of experiment. *Cement & Conc. Comp.*, **34**: 328-336

North Atlantic Treaty Organization (NATO) (2006). *NATO STANAG 1411: Standard to Quantify the Characteristics of Carbon Dioxide (CO_2) Absorbent Material for Diving, Submarine and Marine Applications*. North Atlantic Treaty Organization (NATO), Brussels.

Pennline, H.W., Luebke, D.R., Jones, K.L., Myers, C.R., Morsi, B.I., Heintz, Y.J., & Ilconich J.B. (2008). Progress in carbondioxide capture and separation research for gasification-based power generation point sources. *Fuel Process. Tech.*, **89:** 897–907

Semazzi, F. (2003). Air quality research: perspective from climate change modelling research. *Env. Int.*, **29**: 253-261

Shih, S. -M., Ho, C. S., Song, Y. S. & Lin, J. P. (1999). Kinetics of the reaction of $Ca(OH)_2$ with CO_2 at low temperature. *Ind. Eng. Chem. Res*., **38**: 1316–1322

Shunji, K., Hiromichi, B., Takasumi, K. & Shigehito, S. (2003). Effect of humidity in the circuit on the CO_2 absorption capacity of Amsorb and Sodasorb II. *J Anesth.,* **17**: 145-146

Tollefsen, P., Rypdal, K., Torvanger, A. & Rive, N. (2009). Air pollution policies in Europe: efficiency gains from integrating climate effects with damage costs to health and crops. *Environ. Sci. Policy*, **12**: 870-881

United Nations (2010). The millennium development goals report. Development Indicators Unit, Statistics Division, United Nations.

Wilson, E. J., Klass, A. B. & Bergan, S. (2009). Assessing a Liability Regime for Carbon Capture and Storage. *Energy Proc.*, **1**: 4575-4582

Yang, H., Xu, Z., Fan, M., Gupta, R., Slimane, R.B., Bland A.E., & Wright. I. (2008). Progress in carbon dioxide separation and capture: a review, *J. Env. Sci.*, **20**: 14–27

Yin, J., Zhang, C., Qin, C., Liu, W., An, H., Chen, G. & Feng, B. (2012). Reactivation of calcium-based sorbent by water hydration for CO_2 capture, *Chem. Eng. Jou.*, **198–199**: 38-44

Yu, Q., Delgado, J.,Veneman, R. & Brilman, W. (2017). Stability of a benzyl amine based CO_2 capture adsorbent in view of regeneration strategies. *Ind. Eng. Chem. Res.,* **56**: 3259–3269**.**

DECONTAMINATION OF CHEMICAL WARFARE AGENT BY NANOCOMPOSITE ADSORBENT: A GC-MS STUDY

Faris Rudi*, Norliza Hussein, Siti Noriza Kamel, Hidayah Aziz & Azlan Nor Rashed

Science and Technology Research Institute for Defence (STRIDE), Ministry of Defence, Malaysia

*Email: faris.rudi@stride.gov.my

ABSTRACT

The increase use of chemical warfare agents (CWA) as murder weapons in recent years despite its legal prohibition is alarming. Contamination of CWA to the victims and the environment poses serious health hazards, thus requires appropriate decontamination agents and methods to neutralise CWA into non-toxic products. Zeolites which are commonly used as adsorbents and catalysts have found new use as a decontamination agent. In this study, zinc oxide nanoparticles/silver nitrate-clinoptilolite zeolite (ZnO NPs/Ag-clinoptilolite zeolite) as a novel nanocomposite adsorbent was synthesised and tested as a decontamination agent for 2-chloroethyl ethyl sulphide (CEES) or commonly known as sulphur mustard simulant. The reaction of nanocomposite and nerve agent simulant was carried out in hexane solution and the decontamination process was monitored by gas chromatography mass spectrometer (GC-MS). From the GC-MS result, the hydrolysis product of CEES had been achieved, which is hydroxylethyl ethyl sulphide (HEES) indicating that decontamination of CWA was successful. This demonstrates that ZnO NPs/Ag-clinoptilolite has the potential to be used as a decontamination agent for CEES.

Keyword: *Chemical Warfare Agent (CWA); 2-chloroethyl ethyl sulphide (CEES); gas chromatography mass spectrometer (GC-MS); decontamination; sulphur mustard (HD); nanocomposite*

1. INTRODUCTION

The increase use of chemical warfare agents (CWAs) as murder weapons in recent years despite its legal prohibition is alarming. CWAs, including toxic chemicals and their precursors are prohibited to be used in munitions and devices as well as any equipment specially designed to caused death or harm to others (OPCW Technical Secretariat, 1997). These CWAs are now becoming more available including to non-state actor and terrorist to inflict harm to intended targets or victims (Szinicz, 2005). The assassination of the half-brother of North Korea's President at Kuala Lumpur International Airport 2 (KLIA2) in 2017 by using VX; one of the most hazardous chemical weapons has raised attention throughout the world (OPCW Executive Council, 2017; Rudi *et al*., 2018). While contamination of CWA is hazardous and can be life-threatening, decontamination of CWA is as much challenging. Conventional methods of decontamination of CWAs by using liquid decontaminant (aqueous or solvent) which contains bleaching agent such as hypochlorite, caustic alkali and super concentrated alkali proves to be an effective way to hydrolyze hazardous CWAs to less hazardous chemical (Bizzigotti *et al*., 2012). However, the side effect of using these decontaminants include toxicity to human, environmental pollution and accelerated corrosion to metals. Hence, current research is focused in finding out an alternative and a safe way to decontaminate CWAs without jeopardising the human life and environment (Verma *et al*., 2016).

Recent trends in research of chemical defence around the world are focusing on the alternative technologies for decontamination of CWA. The reasons are the issues related with current decontamination agents such as corrosion, toxic to human health, organic residue produced after

decontamination, decontamination agents which are incompatible to all weather and environmental conditions. At present, researchers are looking into solid inorganics for the decontamination of the CWAs (Yang *et al*., 1992). High surface area and high reactivity efficiency with regard to toxic chemical are the main reasons for this material to be selected for this application (Sadeghi & Yekta, 2015).

Several nanocrystalline metal oxides have also been synthesised such as MgO (Wagner *et al*., 1999; Dadvar *et al*., 2013), CaO (Wagner *et al*., 2000), Al_2O_3 (Wagner *et al*., 2001), ZnO (Mahato *et al*., 2009; Bisio *et al*., 2016) and TiO_2 (Naseri *et al*., 2013). It was found that metal oxide nanomaterials are reactive towards CWAs that have numerous edge and corners for the adsorption and activation of the reactant (Sadeghi *et al*., 2016). The destructive adsorption provides by these nanomaterials promote conversion of CWAs into less toxic chemical compound, thus eventually wiping out the threats of contamination. Despite good chemical reactivity towards these toxic chemicals, Prasad *et al*. (2010) reported that this single metal oxide has low surface area (28 m^2 g^{-1}) which was not efficient for decontamination process. In addition, decontamination of toxic mustard gas HD into non-toxic product with CuO nanoparticles (30 m^2 g^{-1}) only result in 85% of successful conversion rate. The leftover HD can still posed threat in the contamination area. Hence, this proves that high surface area nanoparticles are needed for an effective decontamination of CWAs (Mahato *et al*., 2011).

2. STUDIES ON ZEOLITES AS A DECONTAMINATION AGENT

Zeolites are among potential catalysts that have been studied by researcher as potential solid adsorbent for decontamination of CWAs application. One of it was the study on the effect of adsorption, desorption and thermal oxidation of 2-chloroethyl ethyl sulphide (CEES) on nanocrystalline zeolite which is silicate-1 and NaZSM-5. These two zeolites effectively adsorb sulphur mustard simulant and have potential to be an effective decontamination agent (Stout *et al*., 2007). The combination of zeolite and metal oxide nanoparticles was proven to render solid catalyst where the high surface area and adsorbent capacity provided by zeolite, come together to enhance the efficiency of catalytic process (Qinghu *et al*., 2004). Nickel oxide nanoparticles (NiO NPs) is among transition metal oxides that were used for variety of application such as electrochemical super capacitor (Kalsani *et al*., 2016), electrochromic films (Huang *et al*., 2006) and magnetic properties (Ichiyanagi *et al*., 2003) because of its convenient characteristics (Khalaji, 2013).

Sadeghi *et al*. (2016) successfully synthesised NiO NPs/Ag-clinoptilolite zeolite composite adsorbent as decontamination agent against sulphur mustard and nerve agent simulants. The combination of silver (Ag)-clinoptilolite as host and NiO NPs as guest materials was proven to increase the efficiency of the catalytic process of CWA. In addition, Ag has an advantage to provide strong influence on the absorption properties of zeolites (Marek *et al*., 2016). Mustard gas (HD), a toxic CWA also known as a bis 2-chloroethyl sulphide is a strong vesicant chemical compound that can cause erythema, edema and blistering after an exposure (Florent *et al*., 2020). 2- Chloroethyl ethyl sulphide (CEES) is the surrogate of a mustard gas that has the same functional group (SCH_2CH_2Cl) with HD and is often used in an academic laboratory research due to less toxicity (Cao *et al*., 2018). Chemical structure of HD and CEES are described in Figure 1 below. HD and CEES have sulphur and chlorine functionalities separated by a two-carbon chain; the only differences are that HD has an extra chlorine atom compared to CEES which makes simulant less toxic compared to the real agent HD (Cao *et al*., 2018). Therefore, CEES was used to replace sulphur mustard for this decontamination of nanocomposite study.

Figure 1: Chemical Structure of HD (left) and CEES (right)

To the best of our knowledge, there are no papers reporting the application of ZnO NPs/Ag-clinoptilolite zeolite composite as decontamination agent for sulphur mustard simulants. ZnO NPs has quite a number of Lewis and Bronsted acid-base reactive sites that show high adsorption capacity and is widely suitable to be used in industrial and environmental application (Kiani & Dastafkan, 2016). Among the applications that involved ZnO NPs are gas sensing as a surface acoustic wave (SAW) sensor (Constantinoiu & Viespe, 2020), chemical stability and biocompatibility (Dehkordi *et al*., 2018), hydrothermal method (Zezeng *et al*., 2015), sputtering (Maity *et al*., 2016), solvothermal (Jin *et al*., 2013) and sol-gel (Dhahri *et al*., 2015). Zinc oxide nanoparticles have been successfully established as potential and favourable materials reactive adsorbents for the decontamination of CWAs due to their characteristics (Verma *et al*., 2016). Hence the objective of this study is to synthesise ZnO NPs/Ag-clinoptilolite zeolite as a new decontamination agent for sulphur mustard simulant.

3. METHODOLOGY

3.1 Materials and Reagent

Natural clinoptilolite (NCp) zeolite was purchased from Multavita Company with structural formula of $[(Na, K, Ca)_6 (Si, Al)_{36} O_{72}.20 H_2O]$. Sodium chloride (NaCl), silver nitrate ($AgNO_3$), hydrochloric acid (HCl), zinc nitrate hexahydrate $[(Zn (NO_3)_2.6H_2O]$, hexane and toluene were purchased from Merck, Germany. Chloroethyl ethyl sulphide (CEES) was purchased from Sigma-Aldrich, USA. All chemical used were of analytical grade. Deionised water was used throughout sample preparation.

3.2 Preparation of Na-clinoptilolite Zeolite

The methodology was adopted from Sadeghi *et al*. (2016). 5 g of clinoptilolite zeolite was calcined (heated at high temperature below its melting point) at 300°C for 2 hours. Na-clinoptilolite was obtained by chemically treated with 250 ml of 1 M (NaCl) at 90°C for overnight and washed with deionised water several times until chloride ions was removed. Na-clinoptilolite was then dried at 80°C for 5 hours.

3.3 Preparation of Ag-clinoptilolite Zeolite

4.5 g of previously prepared Na-clinoptilolite was added to 50 ml of 0.1 M silver nitrate ($AgNO_3$). The mixture was stirred continuously at 60°C for 5 hours to perform ion exchange process. The synthesis product obtained was filtered and washed with deionised water and 0.1 M hydrochloride solution (HCl) to remove the excess of silver ions from zeolite framework. The product was dried at 110°C for 16 hours prior to calcination at 400°C for 4 hours. This process was repeated three times to reach a significant ion exchange process.

3.4 Reaction of ZnO NPs/Ag-clinoptilolite Zeolite Composite

3 g of prepared Ag-clinoptilolite was added to 0.5 M zinc nitrate hexahydrate ($Zn(NO_3)_2$. $6H_2O$) reagent in 250 ml deionised water. The solution was stirred at room temperature for 6 hours. The powder obtained was filtered and then washed with deionised water and dried overnight at 110°C. The powder obtained was ZnO NPs/Ag-clinoptilolite zeolite composite after calcination at 500°C for 4 hours.

3.5 Sulphur Mustard Chemical Warfare Agent Simulant Challenge on ZnO NPs/Ag-Clinoptilolite Zeolite Composite

10 µL of toluene as the internal standard and 10 µL of a 4:1 ratio of CEES/H_2O were added to 5 ml of hexane in 20 ml of Erlenmeyer flask. Aluminium foil was used to seal the flask in order to prevent solvent vapourisation. The solution was then vortexed for 1 minute. Approximately 0.3 g of prepared ZnO NPs/Ag-clinoptilolite zeolite composite was added to the solution. The mixture was shaken for 12 hours and no effort was made to control the light and the humidity. After agitation was completed, 10 µL of upper solution was taken out and analysis was performed using GC-MS Agilent 7890 gas chromatograph couple with Agilent 5977B mass spectrometer in electron ionisation (EI) mode.

4. RESULTS AND DISCUSSION

The reaction of ZnO NPs/Ag-clinoptilolite zeolite composite with 2-chloroethyl ethyl sulphide (CEES) was studied by GC-MS. Figure 2 shows the mass spectra of CEES with m/z values of 27, 47, 61, 75, 89, 109 and 124 respectively. Figure 3 meanwhile shows the hydrolysis product of CEES which is HEES after reacting with the nanocomposite with m/z values of 29, 47, 61, 75, 91 and 106 respectively. From our observation, the atomic mass has decreased from 124 to 106, indicating that hydrolysis process has successfully occurred with new and less toxic compound produced. The mechanism schemes of decontamination reaction (adsorption and destruction) of the CEES to the formation of hydrolysis product are shown in Figure 4. Figure 4 below shows two possible route of decontamination and it can occur simultaneously. Referring to (a), adsorption reactions towards CEES simulant happened via nucleophilic bombardment of the Bronsted (hydroxyl groups (Zn-OH)) acid sites via ZnO nanoparticles of the composite to chlorine and sulphur atoms of CEES molecule. In the first instance, cyclic sulfonium, which in non-volatile form, is likely to form an intermediary.

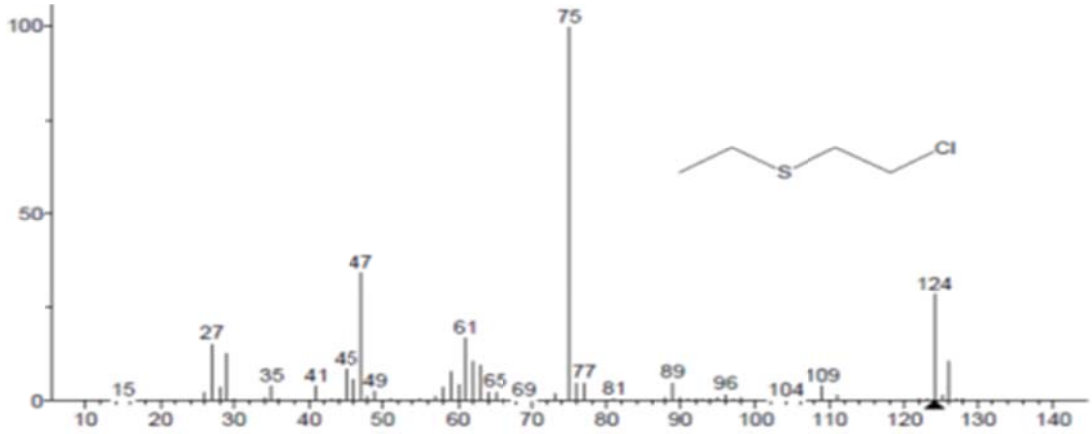

Figure 2: Mass spectra of 2-chloroethyl ethyl sulphide (CEES)

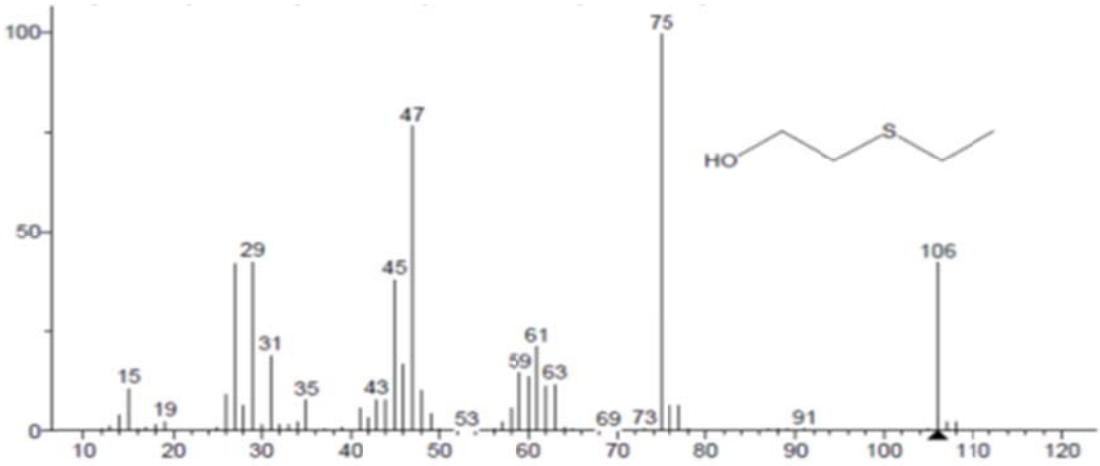

Figure 3: Mass spectra of hydroxylethyl ethyl sulphide (HEES)

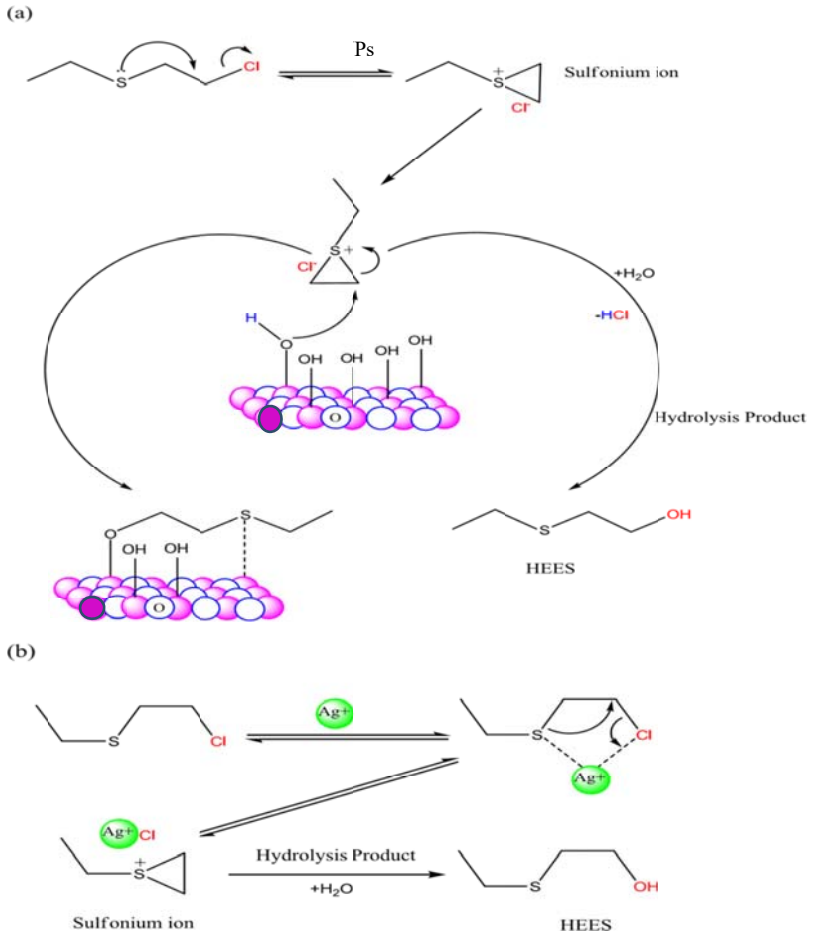

Figure 4: Reaction mechanisms decontamination of CEES on the surface of the ZnO NPs/Ag-clinoptilolite zeolite composite: (a) zinc and (b) silver as the Bronsted and Lewis acid sites (Sadeghi *et al*., 2016).

Chlorine atom in CEES molecules is detached through the process of dehalogenation chemical reaction. Immediate of H_20 molecule will gave a discrete reaction for hydrolysis process to take part on the surface of the zinc species (Zn^{2+}) and the Lewis acid sites is released. Hydroxylethyl ethyl sulphide (HEES) is acquired during the hydrolysis reaction as the reaction process removed the decontamination of the CEES. For instance, with reference to route (b), the electrophilic attacks on positive silver (Ag+) of the zeolite structure to sulphur mustard simulant agent like chlorine and sulphur atom produce CEES molecule that can be adsorbed on the surface of the solid and the composite. The transition states for the formation of S–Ag+ –Cl bonds will further lead to the formation of cyclic sulfonium ions which act as the intermediate. These unstable intermediates will subsequently turn into hydroxylethyl ethyl sulphide (HEES) regardless in the presence or absence of water, as the hydrolysis product on the surfaces of silver species (Ag^{+}) as the Lewis acid sites of the adsorbent composite.

5. CONCLUSION

As a conclusion, ZnO NPs/Ag-clinoptilolite zeolite composite was successfully synthesised as nanocomposite for the decontamination of sulphur mustard simulant. ZnO NPs/Ag-clinoptilolite converted 2-chloroethyl ethyl sulphide (CEES) to hydroxylethyl ethyl sulphide (HEES) by means of hydrolysis process that replaced chlorine with hydroxyl group. GC-MS results show that there is a formation of this less toxic product with molecular ion peak at 106 which was different with CEES molecular ion peak at 124 indicating the synthesis of ZnO NPs/Ag-clinoptilolite zeolite composite was successful. The decontamination properties of ZnO NPs/Ag-clinoptilolite zeolite composite are relatively promising, hence making it a potential candidate as a modern decontamination agent of CWA.

REFERENCES

Bisio, C., Carniato, F., Palumbo, C., Safronyuk, S.L., Starodub, M.F, Katsev, A.M., Marchese, L. & Guidotti, M. (2016). Nanosized inorganic metal oxides as heterogenous catalyst for the degradation of chemical warfare agents. *Catal. Today*, **277:** 192-199.

Bizzigotti, G.O., Rhoads, R.P., Lee, S, J., & Smith, B.M. Handbook of chemical and biological warfare agent decontamination. ILM Publications, 2012.

Cao, Y., Hui, X., Zhu, H., Elmahdy, A. & Maibach, H. (2018). In vitro human skin permeation and decontamination of 2-chloroethyl ethyl sulfide (CEES) using derrmal decontamination gel (DDGel) and reactive skin decontamination lotion (RSDL). *Toxicol. Lett.*, **291:** 86-91.

Constantinoiu, I. & Viespe, C. (2020). ZnO metal oxide semiconductor in surface acoustic wave sensors: A review. *Sensors*, **20:** 5118.

Dadvar, S., Tavanai, H., Morshed, M. & Ghiaci, M. (2013). A study on the kinetics of 2-chloroethyl ethyl sulfide adsoprtion onto nanocomposite activated carbon nanofibers containing metal oxide nanoparticles. *Sep. Puriff. Technol*, **114:** 24-30.

Dehkordi, H.A., Mokhtari, A., Dastafkan, K. & Soleimanian, V. (2018). Sol-gel spin-coating followed by solvothermal synthesis of nanorods-based ZnO thin films: Microstructural, optical, and gas sensing properties. *J. Electron. Mater*, **48:** 1258-1267.

Dhahri, R., Hijri, M., Ei Mir, L., Bonavita, A., lannazzo, D., Leonardi, S.G. & Neri, G. (2015). CO sensing properties under UV radiation of Ga-doped ZnO nanopowders. *Appl. Surf. Sci.*, **355:** 1321-1326.

Florent, M., Giannakoudakis, D.A. & Bandosz, T.J. (2020). Detoxification of mustard gas surrogate on ZnO_2/g-C_3N_4 composites: Effect of surface features' synergy and day-night photocatalysis. *Appl. Catal.*, **272:** 119308.

Huang, X.H., Tu, J.P., Zhang, B., Zhang, C.Q., Li, Y., Yuan, F. & Wu, H.M. (2006). Electrochemical properties of NiO-Ni nanocomposite as anode material for lithium-ion batteries. *J. Power. Sources*, **161:** 541-544.

Ichiyanagi, Y., Wakabayashi, N. & Yamazaki, M. (2003). Magnetic properties of NiO nanoparticles. *J. Phys. B Condens. Meter*., **329:** 862-863.

Jin, C.H., Sze, M.L., Keat, T.L. & Mohamed, A.R. (2013). Preparation and photocatalytic properties of visible light-driven samarium-doped ZnO nanorods. *Ceram. Int*., **39:**5833-5843.

Kalsani, V., Schmittel, M., Listorti, A., Accorsi, G. & Armaroli, N. (2016). Novel phenanthroline ligands and their kinetically locked copper(I) complexes with unexpected photophysical properties. *Inorg. Chem*., **45:** 2062-2067.

Khalaji, A.D. (2013). Preparation and characterization of NiO nanoparticles via solid-state thermal decomposition of Ni(II) complex. *J. Clust. Sci*., **24:** 189-195.

Kiani, A., & Dastafkan, K. (2016). Zinc oxide nanocubes as a destructive nanoadsorbent for the neutralization chemistry of 2-chloroethyl phenyl sulfide: A sulfur mustard simulant. *J. Colloid Interface Sci*., **478:** 271-279.

Maity, S., Bhunia, C.T. & Sahu, P.P. (2016). Reduction in defect levels and improvement in optical and structural properties by modifying ZnO based thin film into nanorods. *Optik*, **127:** 3471-3473.

Mahato, T.H., Prasad, G.K., Singh, B., Acharya, J., Srivastava, A.R. & Vijayaraghavan, R. (2009). Nanocrystalline zinc oxide for the decontamination of sarin. *J. Hazard. Mater*, **165:** 928-932.

Mahato, T.H., Singh, B., Srivastava, A.K., Prasad, G.K. & Srivastava, A.R. (2011). Effect of calcinations temperature of CuO nanoparticle on the kinetics of decontamination and decontamination products of sulphur mustard. *J. Hazard. Mater*., **192:** 1890-1895.

Marek, K.G., Tarach, K.A., Piwowarska, Z., Kaniecki, M. & Chmielarz, L. (2016). Ag-loaded zeolites Y and USY as catalyst for selective ammonia oxidation. *Catal. Sci. Technol*., **6:** 1651-1660.

Naseri, M.T., Sarabadani, M., Ashrafi, D., Saeidian, H. & Babri, M. (2013). Photoassisted and photocatalytic degradation of sulfur mustard using TiO_2 nanoparticles and polyoxometalates. *Environ. Sci. Pollut. Res*., **20:** 907-916.

OPCW Executive Council (2017). Decision Chemical Weapons Incident in Kuala Lumpur, Malaysia. *Documents from the Seventy-Ninth Session of the Executive Council.*, Organisation for the Prohibition of Chemical Weapons (OPCW), The Hague, Netherlands.

OPCW Technical Secretariat (1997). *Convention on the Prohibition of the Development, Production, Stockpiling and Use of Chemical Weapons and on their Destruction.* Organisation for the Prohibition of Chemical Weapons (OPCW), The Hague, Netherlands.

Prasad, G.K., Ramacharyulu, P.V.R.K., Batra, K., Singh, B., Srivastava, A.R., Ganesan, K. & Vijayaraghayan, R. (2010). Decontamination of Yperite using mesoporous mixed metal oxide nanocrystals. *J. Hazard. Mater.*, **183:** 847-852.

Qinghu, T., Qinghong, Z., Ping, W., Ye, W. & Huilin, W. (2004). Characterizations of cobalt oxide nanoparticles with faujasite zeolite and the formation of metallic cobalt. *Chem. Master*, **16:** 1967-1976.

Rudi, F., Aziz, H., Hussein, N., Zahari, N, Bakar, S.A. & Ismail, S. (2018). Identification of spiking chemicals related to the chemical weapons convention in water sample during an interlaboratory competency test. *Defence S& T Technical Bulletin*, **11:** 317-330.

Sadeghi, M. & Yekta, S. (2015). Adsorption and neutralization chemistry of dimethyl methyl phosphonate (DMMP) as an organophosphorus pollutant (OPP) on the surface of nanostructured CO_3O_4 and $MnCO_2O_4$ catalyst. *Iran, Chem. Commun*., **3:** 21-41.

Sadeghi, M., Ghaedi, H., Yekta, S. & Babanezhad, E. (2016). Decontamination of toxic chemical warfare sulfur mustard and nerve agent simulants by NiO NPs/Ag-clinoptilolite zeolite composite adsorbent. *J. Environ. Chem. Eng*., **4:** 2990-3000.

Stout, S,C., Larsen, S.C. & Grassian, V.H. (2007). Adsorption, desorption and thermal oxidation of 2-CEES on nanocrystalline zeolites. *Micropor Mesopor Mat*, **100:** 77-86.

Szinicz, L. (2005). History of chemical and biological warfare agents. *Toxicol.*, **214**:167-181.

Verma, M., Chandra, R. & Gupta, V.K. (2016). Decontamination of 2-chloro ethyl ethyl sulphide and dimethyl methyl phosphonate from aqueous solutions using manganese. *J. Mol. Liq*., **215:** 285-292.

Wagner, G.W., Bartram, P.W., Koper, O. & Klabunde, K.J. (1999). Reactions of VX, GD, and HD with nanosize MgO. *J. Phys. Chem. B*, **103:** 3225-3228.

Wagner, G.W., Koper, O.B., Lucas, E., Decker, S. & Kenneth. J. (2000). Reactions of VX, GD, and HD with nanosize CaO: Autocatalytic dehydrohalogenation of HD. *J. Phys. Chem. B*, **104:** 5118-5123.

Wagner, G. W., Procell, L.R., O' Connor, J.R., Munavalli, S., Carnes, C.L., Kapoor, P.N. & Klabunde, K.J. (2001). Reaction of VX, GB, GD, and HD with nanosize Al_2O_3, formation of aluminophosphonates. *J. Am. Chem. Soc*, **123:** 1636-1644.

Yang, Y.C., Baker, J. A. & Ward, R.J. (1992). Decontamination of chemical warfare agents. *Chem. Rev,* **92:** 1729–1743.

Zezeng, F., Rui,F., Bingfei, D., Haofeng, L., Zhi, J., Xinyu, L., Feng, L., Wei, Z. & Chenyang, W. (2015). Fabrication and properties of ZnO nanorods within silicon nanostructures for solar cell application. *Appl. Phys. Lett*., **106:**3118.

COMPARISON OF PHYSICAL ACTIVITY RATIO OF SPECIFIC PHYSICAL ACTIVITIES PERFORMED BY MILITARY PERSONNEL IN MALAYSIA USING A SELECTION OF PREDICTION EQUATIONS FOR BASAL METABOLIC RATE

Brinnell Caszo[1], Hanapi Johari[2] & Justin Gnanou[1*]

[1]School of Medicine, International Medical University, Malaysia
[2]Faculty of Medicine and Defence Health, National Defence University of Malaysia (UPNM), Malaysia

[*]Email: justingnanou@gmail.com

ABSTRACT

Maintaining energy balance is one of the key aspects of good health. Personnel in the armed forces are faced with unique challenges as they may be in active duty and perform tasks that are strenuous and difficult. Physical activity ratio (PAR) values may be used to calculate energy requirements in order to provide adequate dietary intake. The primary aim of this study was to determine the effect of using different basal metabolic rate (BMR) prediction equations to determine the PAR of specific physical activities taken up by cadet officers during their training. The subjects were recruited by advertisement among military personnel and cadet officers within the ages of 20 to 35 years. Volunteers who were healthy non-smokers with no history of diabetes mellitus or hypertension were included. Written informed consents were obtained from all the subjects and the research study was approved by the university research committee. The recruited subjects underwent an anthropometric assessment, including assessment of height and weight. Predicted BMR was calculated using a set of validated prediction equations. Energy expenditure was measured while performing a set of activities using indirect calorimetry. PAR values were calculated as a ratio of the predicted BMR using each of the different equations. The data was expressed as means and averages, with the different PARs obtained compared using the Friedman's test for nonparametric analyses. The PAR values calculated using the five-prediction equation did not significantly differ from each other. Predicted BMR was used to determine the PAR for each activity. This value should be confirmed in a larger study population before it can be accepted to compute calorie requirements.

Keywords: *Energy expenditure; basal metabolic rate (BMR); military personnel; physical activity ratio (PAR); prediction equation.*

1. INTRODUCTION

Personnel in the armed forces are faced with unique challenges as they may be in active duty and perform tasks that are strenuous and difficult (Ramsay *et al*., 2016; Rice *et al*., 2017; Boffey *et al*.,2019). While performing these tasks, they may be required to carry loads including food rations, which may add to the difficulty of the task at hand (Larsen *et al*., 2014; Talarico *et al*., 2018). Due to the difficulty of the tasks and the environment, maintaining adequate dietary intake to meet the variation in energy expenditure is very important as insufficient energy intake is associated with poor health outcomes (Robertson *et al*., 2000). Though the energy cost of activities performed by military personnel has been documented by others (Johnson *et al*., 2018; Ahmed *et al*., 2019; Ahmed *et al*., 2020), the conditions under which they are recorded, and the particular tasks themselves, differ. Local ambient conditions may vary and differ from place to place. In addition, the study populations sampled should also be representative. Thus, a

measurement performed at site or as near to and under similar conditions in which the measurements would be utilised would provide the most accurate information (Burstein *et al*., 1996).

The total energy intake is determined by energy expenditure, including energy expenditure due to physical activity of an individual. Measures of energy expenditure of individual activities and persons may be obtained using different methods (Hills *et al*., 2014). An indirect calorimeter is often used, measuring exhaled gases via a mask or mouthpiece. Alternately, breath collected in a Douglas bag may be used. Other methods include whole body calorimetry and labelled isotope techniques (Okubo *et al*., 2008). An indirect calorimeter, measuring energy expenditure which is mobile affords several advantages, especially since it may be used in the field.

Estimates of energy expenditure may also be made based on the principle of using multiples of either resting metabolic rate (RMR) or basal metabolic rate (BMR) for an activity. Since these are based on BMR, they allow for controlling the effect of differences arising due to body weight. When expressed as a multiple of BMR, it is known as a physical activity ratio (PAR) (Vaz *et al*., 2005). Assigning a PAR value to an activity allows for the calculation of the energy cost of that activity after factoring in its duration. Thus, knowledge of the PAR allows for accuracy and ease while calculating energy intake to obtain these ratios, a reliable measurement of BMR is needed. In addition to the fact that measuring BMR is an exacting and technically challenging experiment, the conditions under which it is measured, and the methodology used are important factors that affect BMR measurements (Shetty, 2005).

Therefore, in this study, we aimed to investigate the effect of using different predicted equations to estimate BMR values instead of using actual measurements of BMR to calculate the PAR values of activities measured, since BMR is relatively constant especially for male subjects (Henry *et al*., 1989). Since there are contradictory views regarding the effect of ethnicity on predicted BMR values, (de Boer *et al*., 1988; Camps *et al*., 2016), this study looked at the effect of using different BMR prediction equations on PAR values.

2. METHODOLOGY

2.1 Subject Selection and Baseline Measurements

Subjects (n=10) between 20 to 35 years of age who were non-smokers with no history of diabetes mellitus and hypertension were recruited by advertisement among military cadet-officers. Written informed consents were obtained from all the subjects who agreed to participate. The study protocol was approved by the university research committee. A physical activity readiness questionnaire was administered at the time of enrolment and before each experiment to ensure their preparedness to take part in the study.

2.2 Experimental Protocol

After an 8 h overnight fast and without performing any other activity, the subjects reported to the lab at 7:00 am and rested for 30 min. Height was measured to the nearest cm (Seca, Hamburg, Germany), weight to the nearest g, and waist and hip circumference to the nearest cm. Table 1 provides the basic anthropometric data of the subjects.

The energy expenditures of the specific activities listed in Table 2 were measured. These measurements were made using a K4B portable metabolic system (COSMED, Italy) with the use of a closely fitting face mask connected to a flowmeter that is capable of measuring airflow in breath by breath (BXB) mode. Data of O2 and CO2 volumes thus measured were exported to an Excel sheet for analysis. These values,

corrected for body temperature and pressure were substituted into Weir's equation (Weir, 1949) to calculate energy expenditure:

$$\text{Energy expenditure (kcal per day)} = 1.44\,(3.94\,VO2 + 1.11\,VCO2) \quad (1)$$

As PAR represents the ratio of the energy cost of an activity to BMR of the individual, the values were then calculated as follows:

$$PAR = \frac{\text{Energy expended}}{\text{Predicted BMR}} \quad (2)$$

Table 1: Subject characteristics.

Characteristics	Average	Standard Deviation
Age (years)	20.4	0.52
Height (cm)	175.7	5.1
Weight (kg)	68.6	10.6
Mid-arm circumference (MAC, cm)	28.3	2.9
waist (cm)	76.4	11.9
hip (cm)	89.8	13.3

Table 2: Details of the different activities measured.

	Activity	Speed / Distance / Repeats
1	Walking	3.5 m/s
2	With load	3.5 m/s
3	Lift	50 repeats
4	Lift and carry	50 m

2.3 Statistical Analysis

The results were expressed as means ± standard deviation. The means were compared using Friedman's Test for repeated measures and p-value < 0.05 was considered to be statistically significant. The analyses were performed using SPSS version 16.1.

3. RESULTS AND DISCUSSION

The average predicted BMR of the subjects was 1,751.4 ± 162.9 kcal/day. Predicted BMRs based on other predicted equations developed by Mifflin *et al*. (1990), Camps *et al*. (2016), WHO (1985), Owen *et al*. (1986) and Liu *et al.* (1995) were calculated to compare the values recorded in our lab. Among these equations, the ones from Camps *et al*. (2016) and Liu *et al*. (1995) were derived from populations within a similar geographic region. Table 3 provides the BMR values calculated using these equations. Using these BMR values, the PAR values of the four specific activities were calculated (Table 4). It is found that the PAR values differed very little when using the different equations for BMR calculation.

Table 3: BMR Data (kcal/day)

	Mean	SD
Predicted BMR	1,751.4	162.9
Mifflin *et al*. (1990)	1,687.5	128.4
Camps *et al*. (2016)	1,594.7	142.3
WHO (1985)	1,725.4	158.9
Owen *et al*. (1986)	1,574.9	107.6
Liu *et al*. (1995)	1,613.5	161.0

Table 4: PAR values.

	Present study	Mifflin *et al.* (1990)	Camps *et al.* (2016)	WHO (1985)	Owen *et al*. (1986)	Liu *et al.* (1995)
Walking	4.9±2.0	5.1±2.1	5.4±2.2	5.0±1	5.4±2.2	5.3±2.2
With load	4.1±0.6	4.2±0.6	4.5±0.6	4.1±0.7	4.5±0.7	4.2±0.6
Lift	7.0±1.7	7.2±1.8	7.7±1.9	7.1±1.9	7.8±1.9	7.6±1.8
Lift and carry	6.5±1.2	6.7±1.2	7.1±1.4	6.6±1.4	7.2±1.4	7.0±1.3

Daily energy requirements must be sufficient to cover the energy cost of basal metabolism as well as all activities performed daily. BMR or the basal metabolic rate is the energy spent while a person is at rest and not asleep or active. In conditions requiring increased energy expenditure, maintaining adequate calorie and nutrient intake is vital. This ensures that the individual can maintain good health and perform the duties well. This becomes much more important for military personnel. Optimising the quantity of food supplies carried by personnel while working in the field will reduce the load that would have to be carried. This would also impact the amount of calories required by personnel. Historically, persons in the armed forces have had to carry increasing loads in order to wear protective armour, weapons and clothing. In addition to this, adequate food supplies would add to the burden. This may affect readiness in the performance of military duties (Viravathana & Sirichakwal, 2005). Recent studies on troops deployed in, for example, Afghanistan (Fallowfiled, 2014) revealed a loss of weight of 4.6% on average, with partial recovery later on (Margolis *et al*., 2013). Though the troops were able to maintain physical and cardiorespiratory fitness, they did undergo a period of adaptation to the tasks at hand. In a systematic review of studies covering deployment durations from 3 to 34 days, continuous use of combat rations resulted in loss of weight that could affect troop performance (Tassone & Baker, 2017). A 64-day study of a simulated real-world combat situation as part of special forces training in the US demonstrated a loss in body weight of about 4.2 kg, including loss of lean mass of 2.8 kg (Margolis *et al*. 2013). Similarly, a study of female recruits during basic army training also showed that dietary requirements were not met by intakes of candidates as compared to non-military control subjects (Etzion-Daniels *et al*. 2008). A study of Polish soldiers showed a diet of 4,504 kcal/day was used during nine months of infantry training (Tomczak *et al*. 2016). A somewhat different picture appears to emerge based on a review pertaining to seafaring personnel. In a review by Sargent *et al*. (2017), several countries report that seafaring personnel have increased body weight, and that percentage appears to increase as these individuals age.

Thus, it is clear that energy balance is disturbed by changes in physical activity patterns and that it is important to adjust calorie intake in order to maintain energy balance. Thus, measuring actual energy cost of tasks is relevant. It will help to make accurate predictions regarding energy requirement. This will immediately impact several areas, namely provisions for adequate supplies of food, health and well-being

of personnel in order to maintain the efficiency of their work and improve outcomes, reduce the cost needed to treat, as well as rehabilitate personnel from nutrition-related illnesses / conditions.

The PAR values reported in the literature are usually measured as ratios to measured BMR. The impact of using predicted BMR rather than measured BMR in the calculation of PAR was the main focus of this study. The PAR values derived from this data set did not differ significantly. Though this may not appear important, when extrapolated to energy expenditure over 24 h, differences of approximately 500 kcal/day were observed with the example of the PAR values for walking for 24 h in this study set. Comparison with recorded BMR values for these subjects would help to clarify this issue and this is a major caveat in this study.

4. CONCLUSION

In conclusion, this study has provided some useful information on PAR. An effort to further document and compile these values for common activities performed by defence personnel is needed to achieve accurate estimates of daily energy expenditure. Supplying adequate nutrition, with an eye on logistics to maintain food supply would help to optimise nutritional status.

REFERENCES

Ahmed, M., Mandic, I., Desilets, E., Smith, I., Sullivan-Kwantes, W., Jones, P.J., Goodman, L., Jacobs, I. & L'Abbé, M. (2020). Energy balance of Canadian Armed Forces personnel during an Arctic-like field training exercise. *Nutrients*., **12**:1638.

Ahmed, M., Mandic, I., Lou, W., Goodman, L., Jacobs, I. & L'Abbé, M.R. (2019). Comparison of dietary intakes of Canadian Armed Forces personnel consuming field rations in acute hot, cold, and temperate conditions with standardized infantry activities. *Mil. Med. Res*., **16**:26.

Boffey, D., Harat, I., Gepner, Y., Frosti, C.L., Funk, S. & Hoffman, J.R. (2019). The physiology and biomechanics of load carriage performance. *Mil. Med*., **184**:e83-e90.

Burstein, R., Coward, A.W., Askew, W.E., Carmel, K., Irving, C., Shpilberg, O., Moran, D., Pikarsky A., Ginot, G., Sawyer, M., Golan, R. & Epstein, Y. (1996). Energy expenditure variations in soldiers performing military activities under cold and hot climate conditions. *Mil. Med*., **161**:750-754.

Camps, S.G., Wang, N.X., Tan, W.S &, Henry, C.J. (2016). Estimation of basal metabolic rate in Chinese: are the current prediction equations applicable? *Nutr. J*., **15**:79.

de Boer, J.O., van Es, A.J., Voorrips, L.E., Blokstra, F. & Vogt, J.E. (1988). Energy metabolism and requirements in different ethnic groups. *Eur. J. Clin. Nutr*., **42**:983-997.

Etzion-Daniel, Y., Constantini, N., Finestone, A.S., Shahar, D.R., Israeli, E., Yanovich, R. & Moran, D.S. (2008). Nutrition consumption of female combat recruits in army basic training. *Med. Sci. Sports. Exerc*., **40**: S677-84.

Fallowfiled, J.L. (2014). Energy expenditure, nutritional status, body composition and physical fitness of Royal Marines during a 6-month operational deployment in Afghanistan. *Br. J. Nutr*., **112**, 821–829.

Henry, C.J., Hayter, J. & Rees, D.G. (1989). The constancy of basal metabolic rate in free-living male subjects. *Eur. J. Clin. Nutr*., **43**:727-731.

Hills, A.P., Mokhtar, N., & Byrne, N.M. (2014). Assessment of physical activity and energy expenditure: an overview of objective measures. *Front. Nutr*., **1**:5.

Johnson, C.D., Simonson, A.J., Darnell, M.E., DeLany, J.P., Wohleber, M.F. & Connaboy, C. (2018). Energy expenditure and intake during Special Operations Forces field training in a jungle and glacial environment. *Appl. Physiol. Nutr. Metab*., **43**:381-386.

Larsen, B., Netto, K. & Aisbett, B. (2014). Task-specific effects of modular body armor. *Mil. Med*., **179**:428-34.

Liu, H.Y., Lu, Y.F. & Chen. W.J. (1995). Predictive equations for basal metabolic rate in Chinese adults: a cross-validation study. *J. Am. Diet. Assoc*., **95**:1403–8.

Margolis, L.M., Rood, J., Champagne, C., Young, A.J. & Castellani, J.W. (2013). Energy balance and body composition during US Army special forces training. *Appl. Physiol. Nutr. Metab*., **38**:396-400.

Mifflin, M.D., St Jeor, S.T., Hill, L.A., Scott, B.J., Daugherty, S.A., & Koh, Y.O. (1990). A new predictive equation for resting energy expenditure in healthy individuals. *Am. J. Clin. Nutr*., **51**, 241–247.

Okubo, H., Sasaki, S., Rafamantanantsoa, H.H., Ishikawa-Takata, K., Okazaki, H. & Tabata, I. (2008). Validation of self-reported energy intake by a self-administered diet history questionnaire using the doubly labeled water method in 140 Japanese adults. *Eur. J. Clin. Nutr*., **62**:1343-50.

Owen, O.E., Kavle, E., Owen, R.S., Polansky, M., Caprio, S., Mozzoli, M.A., Kendrick, Z.V., Bushman, M. C. & Boden, G. (1986). A reappraisal of caloric requirements in healthy women. *Am. J. Clin. Nutr*., **44:**1–19.

Ramsay, J.W., Hancock, C.L., O'Donovan, M.P. & Brown, T.N. (2016). Soldier-relevant body borne loads increase knee joint contact force during a run-to-stop maneuver. *J. Biomech*., **49**:3868-3874.

Rice, H., Fallowfield, J., Allsopp, A. & Dixon, S. (2017). Influence of a 12.8-km military load carriage activity on lower limb gait mechanics and muscle activity. *Ergonomics*., **60**:649-656.

Robertson, J., Emerson, E., Gregory, N., Hatto, C., Turner, S., Kessissoglou, S. & Hallam, A. (2000). Lifestyle related risk factors for poor health in residential settings for people with intellectual disabilities. *Res. Dev. Disabil*., **21**:469-86.

Sargent, C.1., Gebruers, C. & O'Mahony, J. (2017). A review of the physiological and psychological health and wellbeing of naval service personnel and the modalities used for monitoring. *Mili. Med. Res*., **4**:1-28.

Shetty, P. (2005). Energy requirements of adults. *Public. Health. Nutr*., **8**:994-1009.

Talarico, M.K., Haynes, C.A., Douglas, J.S. & Collazo, J. (2018). Spatiotemporal and kinematic changes in gait while carrying an energy harvesting assault pack system. *J. Biomech*., **74**:143-149.

Tassone, E.C. & Baker, B.A. (2017). Body weight and body composition changes during military training and deployment involving the use of combat rations: a systematic literature review. *Br. J. Nutr*., **117**: 897-910.

Tomczak, A., Bertrandt, J., Kłos, A. & Kłos, K. (2016). Influence of Military Training and Standardized Nutrition in Military Unit on Soldiers' Nutritional Status and Physical Fitness. *J. Strength. Cond. Res*., **30**:2774-2780.

Vaz, M., Karaolis, N., Draper, A., & Shetty, P. (2005). A compilation of energy costs of physical activities. *Public. Health. Nutr*., **8**:1153-1183.

Viravathana, N. & Sirichakwal, P. (2005). Energy and nutrients intake of Thai active duty army personnel at the Army Special Warfare Command Unit. *J. Med. Assoc. Thai*., **88**:S110-5.

Weir, J.B. (1949). New methods for calculating metabolic rate with special reference to protein metabolism. *J. Physiol*. **109**:1-9.

WHO (World Health Organization) (1985). *Energy and Protein Requirements*. World Health Organization, Geneva, Switzerland.

CHARACTERISATION OF MECHANICAL-ELECTRICAL PROPERTIES OF GRAPHENE NANOPLATELETS FILLED EPOXY AS CONDUCTIVE INK

Maizura Mokhlis[1], Mohd Azli Salim[1,2,*], Nor Azmmi Masripan[1], Adzni Md. Saad[1], Feng Dai[3], Azmi Naroh[4] & Mohd Nizam Sudin[1]

[1]Fakulti Kejuruteraan Mekanikal, Universiti Teknikal Malaysia Melaka (UTeM), Malaysia
[2]Advanced Manufacturing Centre, Universiti Teknikal Malaysia Melaka (UTeM), Malaysia
[3]China Railway Eryuan Engineering Group Co., China
[4]Department of Mechanical Engineering, Politeknik Ungku Omar, Malaysia

[*]Email: azli@utem.edu.my

ABSTRACT

With the accelerating pace of development in printed electronics, the fabrication and application of conductive ink have been brought into sharp focus in recent years. The discovery of graphene also unfolded a vigorous campaign on its application. The purpose of this study was to determine the effect of graphene ink when the heat was applied to obtain the optimised formula and prepare graphene conductive ink with good conductivity. In this paper, graphene conductive ink was prepared using a simple method involving mixing, printing, and curing processes to produce conductive ink according to the formulation. Different compositions of a mixture that contained filler, binder, and hardener were put inside a vacuum to remove bubbles and the ink was cured at 150°C for 30 minutes. This research also studied the effect of the temperature on electrical and mechanical properties, and surface roughness of the hybrid conductive ink using a varying amount of filler for graphene nanoplatelets (GNP) inks. The electrical and mechanical properties were assessed using a four-point probe complying with the ASTM F390 and a Dynamic Ultra Microhardness complying with the ASTM E2546-15. The experimental results demonstrated an improvement in electrical conductivity. GNP showed resistivity around 0.0456 Mohm/sq. The correlation between the material hardness with different percentages of filler loading for GNP ink with and without thermal effect conditions was presented. Both of the two GNP ink conditions exhibited similar graph trends, where the hardness was found to increase as the filler loading in the ink was increased.

Keywords: *Graphene ink; sheet resistivity; surface roughness; cross-section; hardness.*

1. INTRODUCTION

In the last few years, the development of technologies for conductive ink grew significantly. Conductive ink has been pushed forward by the progress of printed and flexible electronics (Rosa *et al.,* 2015). Printed electronics are involved in the development of electrical and electronic system printing techniques on different types of substrates. It is an emerging technology, which grows rapidly due to its wide application in radio frequency identification (RFID) (Huang *et al.,* 2015; Leng *et al.,* 2016), chemical sensors (Singh *et al.,* 2017; Tortorich *et al.,* 2018) and wearable electronics (Van Den Brand *et al.,* 2015; Gao *et al.,* 2017). There is an ever-increasing need to develop and produce electronic devices with new characteristics, which have low manufacturing costs, long-endurance time, environmentally sustainable production methods, recycling ability, lower energy consumption, and higher efficiency.

To meet all the requirements, a new manufacturing technique must be developed, and new advanced materials must be taken into use. One of the promising manufacturing techniques for electronic production is printing. Printing is an additive method, which can be used to prepare conductive pattern

directly on flat or even with differently shaped and curved surfaces. Different printing techniques like screen printing, gravure printing, and flexographic printing have been used to fabricate electronic circuits. These printing techniques offer a way to manufacture electronic circuits onto several materials such as paper, plastic, and fabric and make the integration process possible.

Conductive ink consists of conductive materials, polymer matrix, solvents, and additives. Generally, the conductive materials used involve metal nanoparticles (Vasiljevic *et al.,* 2013), carbon nanotubes (Lau *et al.,* 2013), and graphene (Eawwiboonthanakit *et al.,* 2017). Nanomaterials, which possess high career mobility, optical transparency, mechanical robustness and flexibility, lightweight and environmental stability have been in immense demand. Graphene is one of the nanomaterials that fulfill all these requirements, along with other inherently unique properties and convenience to fabricate into different morphological nanostructure, from atomically thin single layers to nanoribbon (Atif *et al.,* 2016; Mokhlis *et al.,* 2020). So far, three kinds of graphene-related conductive ink have been fabricated, which are pristine graphene (PG) ink (Wajid *et al.,* 2013), graphene oxide (GO) ink (Abdullah & Ansari, 2015), and reduced graphene oxide (RGO) ink (Huang *et al.,* 2011). Each kind of ink has its pros and cons.

This research is focusing on graphene nanoplatelets (GNP). GNP consist of a small stack of graphene sheet with a platelet shape as shown in Figure 1 and are highly used as filler in the study of polymer composites. The geometrical structure of GNP, with the particle size of nanoscale thickness and micron-scale lateral surface area allows a high surface contact area. By embedding the polymer matrix at low filler loading, it improves the properties of the polymer matrix without sacrificing any intrinsic properties. To form conductive ink, epoxy resin is the most compatible polymer binder due to its viscosity behaviors. It is also the most extensively used thermoset polymer in the composite industry. It is frequently used in demanding applications due to excellent chemical and corrosion resistance, outstanding adhesion properties, low shrinkage, and low price (Wei *et al.,* 2015). As for hardener, it is a solvent that is added to the ink mixture to harden and produce strong and more durable ink as well as a curing agent for epoxy.

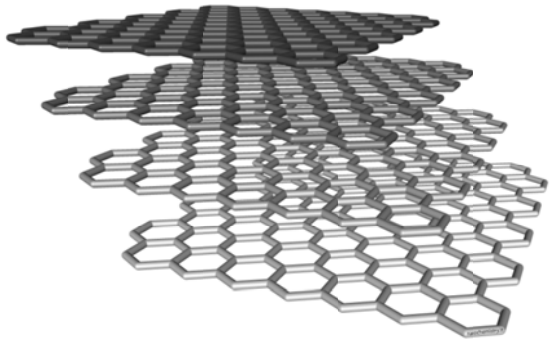

Figure 1: Crystal structure of GNP (Kucinski *et al*., 2013).

In general, conductive ink is composed of a conductive phase with ink binder and additives in a solvent. The conductive phase plays the role of conducting current and ink binder dissolves in a solvent to connect the conductive phase, while additives are used to adjust the printability of conductive ink. The major issue to be resolved in the formulation of conductive ink should not only focusing on the synthesis of raw material but also the ink formulation to improve the stability and dispersion of the ink. The ink originally comes in liquid form and will be drawn on a substrate and cured afterward. The ink draws on the substrates is usually cured with an oven. These processes use heat to evaporate binders and unwanted solvent in conductive ink polymers, which leave only the nanoparticles contents that are already been hardened and stick onto the substrate. Curing is the process to crosslink the polymer materials that can form a good composition with excellent properties.

One of the major challenges is to formulate suitable inks that can be printed using printing technologies in order to replace conventional technologies, which create a limitation in terms of an environmental issue (Faddoul *et. al*., 2012; Wu, 2017). Up to now, numerous kinds of conductive ink with different fillers such as silver, copper, and carbon-based material have been developed for the formation of conductive ink. Typically, silver and copper inks have been globally commercialised and used in electronic industries due to their excellent electrical conductivity performance. However, the problems with silver ink are the high cost, low content, and electromigration behaviour that limit their widespread industrial application.

Other than that, copper is an attractive alternative material to silver due to its comparable bulk conductivity. However, copper is easily oxidised, and the presence of copper oxide increases sintering temperature and reduces conductivity (Lee *et. al*., 2008; Nie *et. al*., 2012; Yang *et. al*., 2016). Thus, there is still a need to develop new types of conductive ink to solve the above-mentioned problem. Therefore, carbon-based material is utilised in this study as the filler material, which is graphene nanoplatelets (GNP) with different filler percentages to investigate the role of those properties in the enhancement of functionality and reliability of the conductive ink (Ismail *et al.,* 2020).

2. METHODOLOGY

2.1 Materials

Graphene nanoplatelets with a surface area of 500 m^2/g were used as the main filler in this study. Binder system bisphenol, an epoxy resin BE-188 (BPA) was used as a binder to bind the particles together, and ACR Hardener H-2310 polyamide amine to harden the mixture.

2.2 Ink Preparation

The fabrication of graphene conductive ink involves formulating the ink composition, preparing the ink sample, printing the ink on the compatible substrate, and curing at the temperature of 150°C for 30 minutes. For the first condition, namely mixing without thermal effect, the stirring process took 15 minutes continuously at room temperature (25°C) by using a glass rod. For the second condition, namely mixing with thermal effect, the stirring process took 15 minutes continuously with the addition of heat at 70°C. The preheated mixture was taken into the vacuum to remove the bubbles. The conductive ink was prepared with six (6) different percentages of filler loading: 10, 15, 20, 25, 30, and 35 wt.% with the hardener in the ratio of 100:30. The composition of the filler loading is tabulated in Table 1.

Table 1: The composition of graphene ink.

Sample	Filler		Binder		Hardener	Total
	(%)	(g)	(%)	(g)	(g)	(g)
1	10	0.2	90%	1.8	0.54	2
2	15	0.3	85%	1.7	0.51	2
3	20	0.4	80%	1.6	0.48	2
4	25	0.5	75%	1.5	0.45	2
5	30	0.6	70%	1.4	0.42	2
6	35	0.7	65%	1.3	0.39	2

The ink was prepared by manual mixing that involved a stirring process by using a glass rod. Stirring plays an important role in ensuring the uniform distribution of epoxy in the mixture and it can break up the agglomerates of GNP and epoxy resin to produce high GNP/epoxy dispersion. The experiment started with the deposition of the inked track onto a glass substrate using the doctor blade technique. A doctor blade method was used to deposit the ink, in which a metal stencil and low tack tape were applied on a polymer substrate. The stencil was placed on the tape polymer substrate and a knife was

used to cut the tape accordingly to leave a negative shape of the track image. The stencil was then removed, and the negative track of the tape was then flooded with ink and a scraper was used to draw across the surface of the tape. Once it had properly flooded and scraped with the excess ink removed, the tape was peeled off and left a positive image of ink (Nash *et al*., 2015).

The ink track samples were then transferred into the oven to undergo ~~a~~ curing process. During the curing process, it produces a highly-cross-linked microstructure that provides high modulus and strength, good resistance to creep, and good performance at elevated temperatures. Then, the cured sample was cooled down slowly to room temperature inside the oven. The curing process had been set up at 150°C for 30 min with an increment of the filler loading. The result turned out to be as expected, in which the higher the filler loading resulting in better performance of ink track. The resistance of the inked track increased as the filler loading increased, which gave better conductivity. Optimised graphene conductive ink was printed on a glass slide with a size of 7.5 cm x 0.3 cm and cured to test the resistance value using uniformity and continuity tests. For the uniformity test, the printed graphene ink was divided into six-point as shown in Figure 4. The resistance value was tested for each centimetre along the length direction. Then the test length was increased per centimetre for the continuity test. All the data for each of the graphene printed ink samples were collected for three repetitions and the average values and standard deviations (error bar) were obtained.

2.3 Sample Characterisation

This study is focusing on examining the morphological, electrical, and mechanical properties of the graphene nanoplatelets (GNP) reinforced epoxy composite. In order to evaluate these properties, the samples were prepared specifically according to each relevant testing standard. Nine marks were constructed at each ink layer in one sample to specify upper, middle, and lower positions as shown in Figure 2. The average values from these marks became the results and the details were discussed.

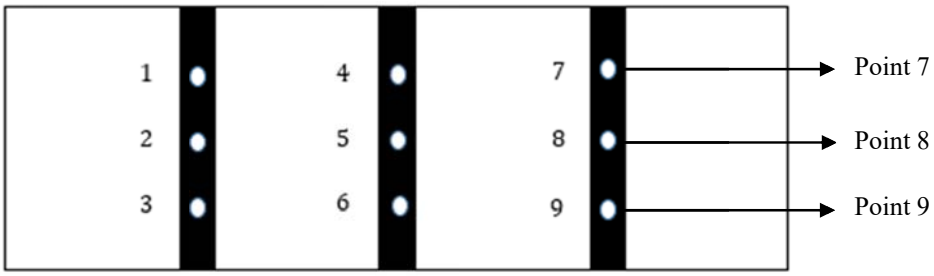

Figure 2: Schematic diagram of printed ink on a glass slide.

2.3.1 Morphology Properties

Scanning electron microscopy (SEM) was used to investigate and evaluate the cross-section of the printed sample. Furthermore, the auto fine machine coating was used to coat the printed sample in order to avoid charge accumulation. SEM employs electron beams to get information from a sample at the nanoscale. The main signals that are detected are the backscattered (BSE) and secondary electron (SE), which generate a grayscale image of the sample at very high magnification. However, there are many other signals which can be the products of electron-matter interaction, and these can provide additional information about the sample such as energy dispersive x-ray (EDX). The data that is generated by EDX analysis consists of spectra with peaks corresponding to all the different elements that are present in the sample. This study investigated the distribution between filler reinforced binder at different filler loadings. The distribution state of nanofillers is crucial to the nanocomposites. Chandrasekaran *et al*. (2014) reported that the homogenous dispersion of nanofillers was an important factor affecting the mechanical properties of the composites (Chandrasekaran, 2014).

2.3.2 Electrical Properties

The electrical properties of cured samples were measured to determine their functions. In this study, the sheet resistance of the conductive ink was determined using JANDEL In-Line Four Point Probes with a 1 mm distance between each probe by referring to ASTM F390 as shown in Figure 3. To measure the resistance of the cured ink, the probe was held in firm contact with the inked track. The four-point probe works by forcing a constant current along with two outer probes and the voltage is read out from the two inner probes. Each data point was obtained as an average of twelve different measurements on the sample.

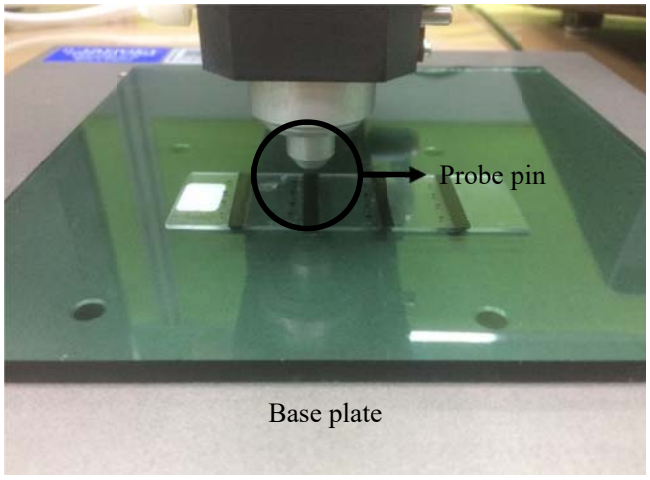

Figure 3: Four-point probe sample preparation.

2.3.3 Mechanical Properties

Nanoindentation analysis was carried out using Dynamic Ultra Micro Hardness testing using a three-sided pyramidal (Berkovich) diamond tip. The nanoindenter test was conducted to describe the elastic behavior of the printed ink. The test method used was the continuous stiffness method (CSM), which able to plot the curve of hardness and modulus by continuously varying indentation depth. The nine indentations had been made for each sample. Each sample was measured at nine different positions. During each test run, a personal computer collected and stored data for the load and displacement as the indenter was driven into the sample. Then, the raw data was used to construct the load-displacement graph.

2.3.4 Surface Roughness

A 3D non-contact profilometer was used to measure the surface profile to quantify its roughness. It greatly depended on the surface geometry of the printed pattern such as thickness and roughness. The leading method of this type of technique is light. Emitted light from the instrument is reflected and read to measure without touching the sample. The thickness was measured using I-solution lite software connected to an optical microscope. The thickness values were the average values from nine different measurement points on the ink tracks. Minimum, maximum, and standard deviation were also calculated by the software. The surface roughness values of Ra and Rz of the substrate were measured using a profilometer.

3. RESULTS & DISCUSSION

All the collected data and results obtained from the experiment and tests were analysed and recorded. The resistivity, stability, and microstructure of ink were discussed to find out the best ink formulation based on the recorded data. The result turned out to be as expected in which the higher the filler loading resulting in better performance of the ink track. The resistance of the inked track increased as the filler loading increased and it gave better conductivity.

3.1 Morphological Properties

The enhancement of the properties is strongly correlated with nanocomposite microstructure. Effective characterisation of morphology is important to establish a structure-property relationship for these materials. Scanning electron microscopy (SEM) had been used to evaluate the dispersion of GNP as well as to examine the surface for filler pull out, which could give insight into the strength of interfacial adhesion. There were six samples as shown in Figures 4 (a) and (b) and Figures 5 (a) and (b). It shows that 10 wt.% and 15 wt.% of GNP inks with and without thermal effect have brighter images and uneven distribution on the cross-sectional area. The micrograph also shows bad dispersion with many small and black clusters of GNP inks.

Comparatively, the dispersion of low filler loading of 10 wt.% and 15 wt.% between the GNP inks with and without thermal effect does not change significantly, but the aggregate size indeed becomes smaller as shown in Figures 4 (a) and (b) and Figures 5 (a) and (b). Hence, they do not show the existence of resistivity as they contain a low percentage of filler loading (Chatterjee *et al*., 2012). Starting from 20 wt.% of filler loading as shown in Figures 4 (c) and Figure 5 (c), the cross-sectional images have shown smooth, homogeneous, and continuous cross-sectional areas on the GNP inks. In the same figures, they illustrate that the GNP inks distribute uniformly on the substrate and even further, GNP ink can be dispersed and stabilised well in the conductive ink.

From Figures 4 (e) and (f) and Figures 5 (e) and (f), they show a smooth surface, which reveals the nature of weak resistance to crack initiation and propagation. On the other hand, composite containing a high percentage of filler loading exhibits relatively rough with some river-like structure. Comparatively, the composite with the highly dispersed GNP inks exhibits a rougher surface and numerous tortuous and fine river-like structures with hackles and ribbons. This result was similar to one of the studies that had been reported (Tang *et al.,* 2013). Therefore, Figures 4 and 5 show the cross-sectional area of GNP ink without thermal effect and GNP ink with thermal effect.

In EDX, the y-axis depicts the number of counts and the x-axis illustrates the energy of x-rays as shown in Figures 6 and 7. The position of the peaks leads to the identification of the element concentration in the sample. Samples of 10 wt.% of graphene ink with and without thermal effect have an atomic weight of 74.88 % and 69.00 %, while for the samples of 35 wt.% are 84.00 % and 100.00% respectively. The higher the atomic weight of graphene, the lower the resistance of conductive ink track because the lesser amount of carbon particle that obstructs the movement of electron between graphene particles.

Electrical conductivity is the measurement regarding the ability of a material to transfer or conduct an electric current. Lower resistance means that the material will conduct electricity more easily than a material with high resistance.

$$\sigma = \frac{1}{\rho} \tag{2}$$

where σ is conductivity.

Filler loading	GNP ink without thermal effect	
	x300	x1000
(a) 10 wt.%	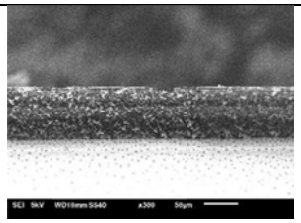	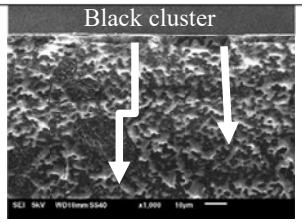
(b) 15 wt.%	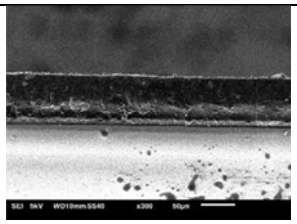	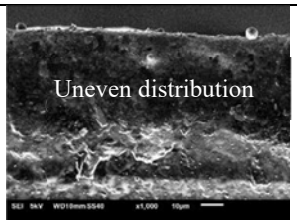
(c) 20 wt.%	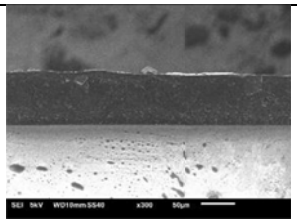	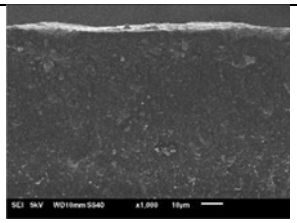
(d) 25 wt.%	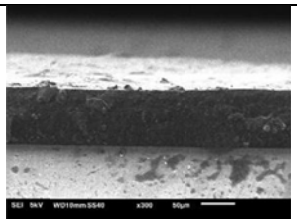	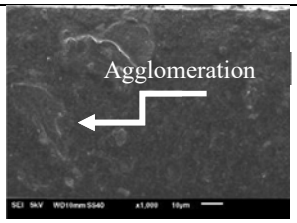
(e) 30 wt.%	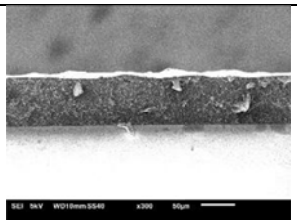	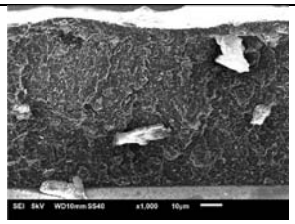
(f) 35 wt.%	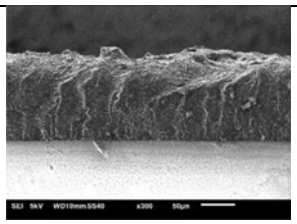	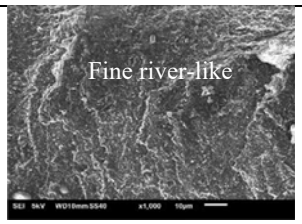

Figure 4: The cross-sectional areas of GNP ink without thermal effect.

Filler loading	GNP ink with thermal effect	
	x300	x1000
(a) 10 wt.%	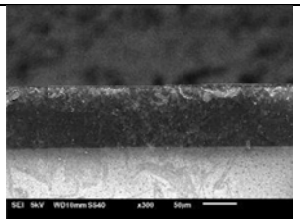	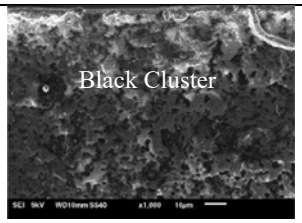
(b) 15 wt.%	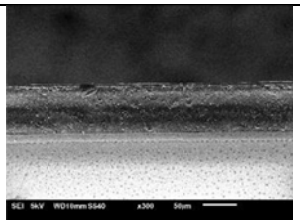	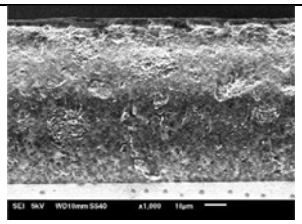
(c) 20 wt.%	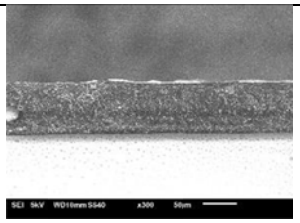	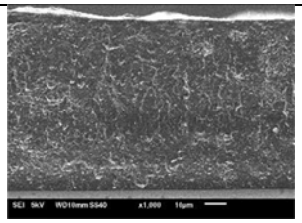
(d) 25 wt.%	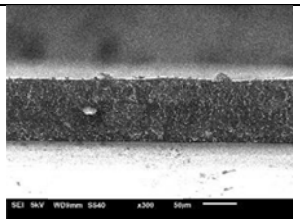	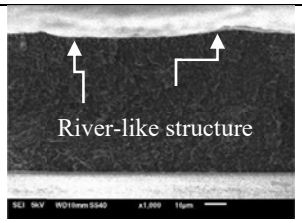
(e) 30 wt.%	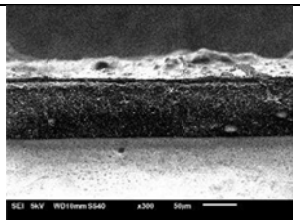	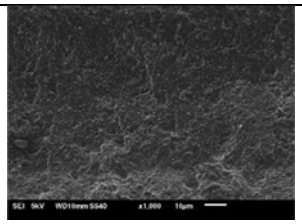
(f) 35 wt.%	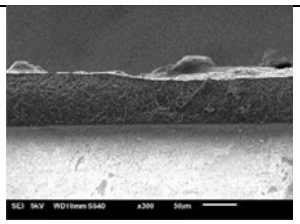	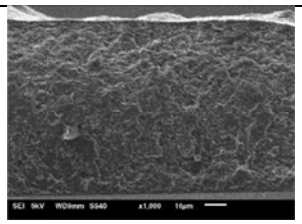

Figure 5: The cross-sectional areas of GNP ink with thermal effect.

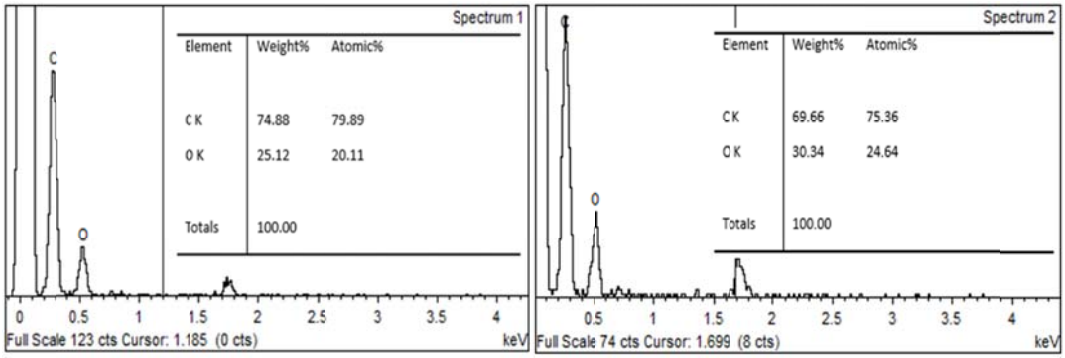

(a) **(b)**

Figure 6: EDX analysis showing the content of sample 10 wt.%: (a) GNP ink without thermal effect (b) GNP ink with thermal effect.

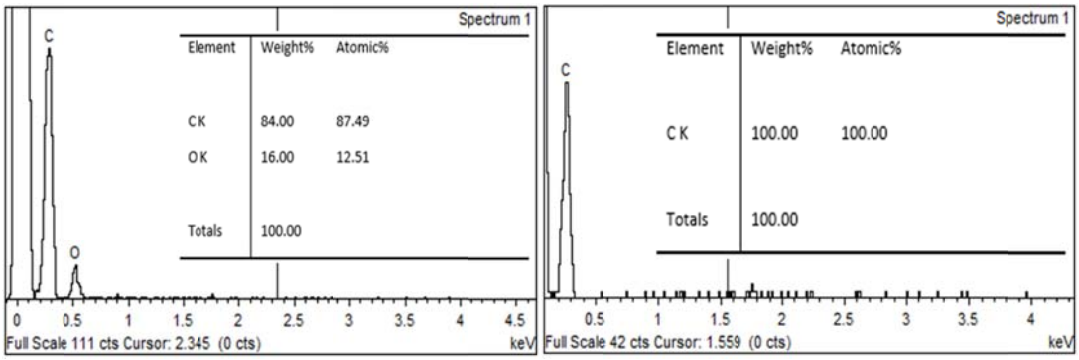

(a) **(b)**

Figure 7: EDX analysis showing the content of sample 35 wt.%: (a) GNP ink without thermal effect (b) GNP ink with thermal effect.

3.2 Electrical Properties

For the printed samples of both GNP ink with and without thermal effect, the resistance is opposing the flow of electrons through the material in response to an applied voltage. Conductors have very small resistances and allow electrons to flow easily if a voltage is applied. Insulators have large resistance and do not allow electrons to flow easily. In order to prove how easily the sample conduct electricity, a device called a four-point probe was used to measure the resistance. When the probe was connected to the printed samples, the voltage was supplied and then the current through the ink was measured at the given voltage. The relationship between resistance and resistivity is important to be understood when describing the printable conductor. Resistance is a measurement for an object to resist or oppose an electric current that flows through it. The electrically resistive nature of the material is an intensive property, which is known as resistivity. The resistance depends on the physical shape and pattern, but the resistivity depends on the nature of the material. The relationship between resistance and resistivity is shown below:

$$\rho = \frac{A}{L} R \tag{1}$$

where ρ is volume resistivity, A is cross-sectional area, L is length, and R is resistance.

Table 2 shows the average value of sheet resistance and the standard deviation for six (6) percentages of filler loading. Each sample consists of six points to measure the uniformity of the printed GNP ink. Therefore, there is no standard benchmark in determining the standard deviation, but the lowest value indicates the best standard deviation. It presents how tightly the data is gathered around the mean or average or how far the data is spread out from the mean or average. The table below shows that 20 wt.% of GNP ink without thermal effect has a very large standard deviation as compared to 20 wt.% of GNP ink with thermal effect.

Table 2: The sheet resistance value of GNP ink.

	Filler loading	10wt.%	15wt.%	20wt.%	25wt.%	30wt.%	35wt.%
Sheet resistance (MΩ/sq)	GNP without thermal effect	0	0	308.88	42.324	3.3519	0.0456
	Std	0	0	15.444	2.1162	0.1675	0.00228
	GNP ink with thermal effect	0	0	11.909	2.2913	0.1616	0.1431
	Std	0	0	0.5954	0.1145	0.00808	0.00715

Figure 8 shows the sheet resistivity against the percentage of filler loading for both graphene inks in two conditions, with and without thermal effect. In general, regardless of adding the temperature to the mixture, the sheet resistivity of the ink decreases with an increase in the filler loading from 10 wt.% to 35 wt.%. In other words, better electrical conductivity is achieved by increasing the filler loading. Such observation is supported by percolation theory, which states that filler content in conductive polymer composite reaches its critical volume that varies, based on the filler's physical properties such as shape and size. Upon reaching the critical volume, the filler forms a three-dimensional conductive network within the polymer matrix and resulting in a dramatic decrease in the sheet resistance (Saad *et al*., 2020).

From all the prepared samples, the results reveal that only four samples have the existence of resistivity, which are from 20 wt.% to 35 wt.%. For 10 wt.% and 15 wt.%, there is no existence of resistivity due to the small amount of filler loading. A small amount of filler loading leads to an agglomeration effect. No electrical conductivity is produced due to the agglomeration effect. Therefore, there are no resistivity values can be obtained. The different range of resistivity at different filler loadings on the samples is shown in Figure 8. From the graph, 35 wt.% of the ink mixture shows lower resistivity. It is proven that the higher the percentage of filler loading, the lower the resistivity.

There is a major difference between the values of resistivity of 20 wt.% to 25 wt.% for GNP ink without thermal effect. It is because of the possibility that the ink is not well-distributed all over the gap between the scotch tape on the glass slide when the blade is moved across the gap due to the speed or the viscosity of the ink. When the speed of the blade increases, the ink may lose and not covering all the gap area. As for the viscosity of the ink, it increases with higher filler content. Ink with high viscosity is hard to print in compliance with the texture of the ink. Thus, it causes the inconsistent thickness of printed inks on the glass side. Some regions may have different thickness, which leads to different spreads of conducting material.

There is a significant difference in values before and after 15 wt.% of filler loading, which are 327.95 MΩ/sq for ink without thermal effect and 16.54 MΩ/sq for ink with thermal effect. However, when the loading reaches approximately 30 wt.%, it can be clearly seen that the sheet resistance has reached a plateau. This trend suggests that the conductive ink has been transformed from bulk insulator to bulk electrical conductor by the percolated network. In addition, during this state, the electrical performance of the ink is determined by intrinsic filler material properties (Lu, 2012). Furthermore, the higher content of filler loading is needed to make good physical contact with other fillers to building up the conductive network.

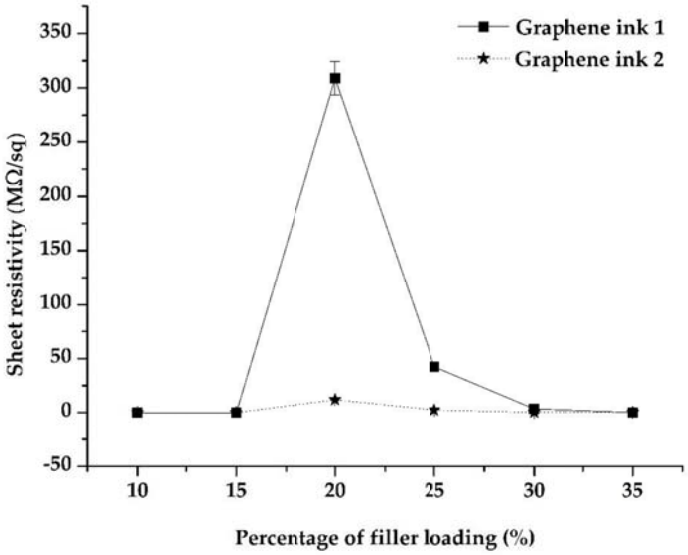

Figure 8: The graph of sheet resistance against filler loading.

3.3 Mechanical Properties

Graphene has excellent mechanical properties, particularly high Young's modulus. These exceptional properties make graphene an ideal candidate as a filler for nanocomposites materials. This Graphene ink is aimed to be exploited due to remarkable mechanical enhancement effect with the possibilities to introduce further functionalities such as electrical conductivity. For this study, nanoindentation analysis was carried out using the method described by Deng in 2013. Two frequently measured mechanical properties are Young's modulus and hardness. As the indenter is driven into the material, both elastic and plastic deformations cause the formation of hardness. After the indenter is withdrawn, only the elastic portion of the displacement is recovered, thus this recovery enables one to determine the elastic properties of a material. Therefore, the first step of measurement was preparing the sample by mounting it on a sample disk (Oliver *et al.,* 2004). The load-displacement graph shows the typical load-indentation depth curve obtained by nanoindentation for screen printed graphene ink. There is a possibility that the curve shows a similar trend, but the indentation and elastic behaviour are not the same.

Table 3 shows the maximum force, maximum depth, hardness, and elastic modulus for GNP ink without thermal effect (graphene ink 1) and GNP with thermal effect (graphene ink 2). The maximum penetration depth of all the graphene ink samples starting from 10 wt.% to 35 wt.% is at the same curing temperature. It clearly shows that the higher the percentage of filler loading causes a lower penetration depth. The lower the penetration depth indicates that the printed graphene ink is getting hardened.

As for Figure 9, it shows that when the filler increases, the hardness level of the printed graphene ink sample is also increasing accordingly. For GNP without thermal effect (graphene ink 1), the value increases in parallel with the increase of filler loading with 12.6 HV to 35.6 HV. While for GNP with thermal effect (graphene ink 2), the value of hardness also increases from 12.3 HV to 37.4 HV respectively. Similarly, this study is consistent with the result of Chatterjee in 2012, who reported an increase of approximately 0.266 GPa for the neat epoxy up to 0.290 GPa for 20 wt.% of GNP loading.

Table 3: The result from nanoindentation for GNP ink

Filler loading	Maximum force, Fmax (mN)		Maximum depth, hmax (μm)		Hardness (HV)		Elastic Modulus, Eit (GPa)	
	GNP ink without thermal effect	GNP ink with thermal effect	GNP ink without thermal effect	GNP ink with thermal effect	GNP ink without thermal effect	GNP ink with thermal effect	GNP ink without thermal effect	GNP ink with thermal effect
10wt.%	323.16	334.1	10.7	10.5	12.6	12.3	5.324	12.01
15wt.%	351.15	398.6	10.7	10.4	13.1	15.1	7.341	14.07
20wt.%	601.4	572.1	10.4	10.3	27.5	23.2	7.128	13.28
25wt.%	633.3	593.6	10.2	10.1	31.1	30.1	6.863	6.315
30wt.%	713.2	655.3	10.2	10.1	34.7	34.5	8.047	6.374
35wt.%	744.6	759.5	10.2	10.1	35.6	37.4	8.722	8.531

In short, the nanoindentation results show an improvement in hardness for GNP ink without thermal effect (graphene ink 1). Therefore, hardness value also has a similar tendency with sintering temperature. This increment is closely associated with grain growth at a higher temperature. More grain growth at higher temperature improves the mechanical properties. Moreover, based on the nanoindentation result, it confirms that the toughness of the ink increases when the heat is applied during the mixing method.

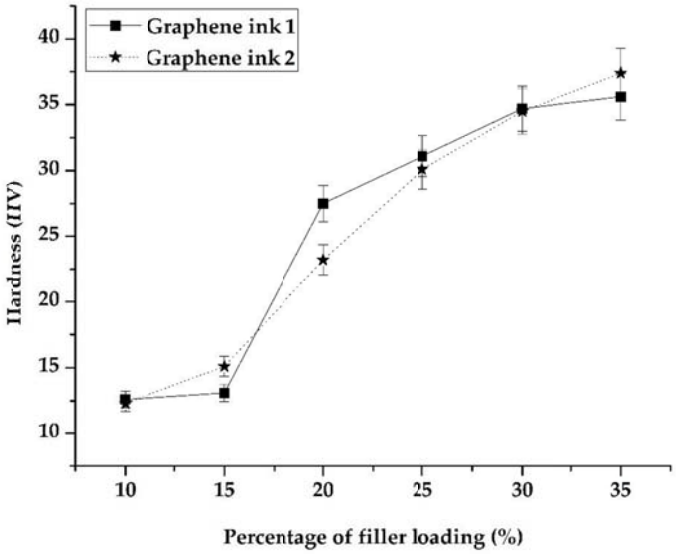

Figure 9: The graph of hardness against filler loading.

Moreover, Figure 10 indicates the result of Young's modulus of the samples of GNP ink without thermal effect (graphene ink 1) and GNP ink with thermal effect (graphene ink 2). As can be seen from Figure 10, it is expected that higher curing temperature leads to higher hardness and Young's modulus of the printed graphene ink. The elastic begins to degrade by increasing the curing temperature. This study assumes that, by adding the temperature, the properties of graphene ink will change from brittle to ductile. Therefore, graphene ink that cures at a higher temperature is likely to be stiffer. The result of this study was also compared with the findings of previous work. Previous

researchers had reported that the obtained values of Young's modulus were approximately 3.9 GPa to 4.2 GPa, which were lower than this study (Chatterjee *et al.,* 2012).

On the other hand, Figures 11 and 12 exhibit the maximum and minimum penetration depths achieve by the samples with lower and higher percentages of filler loading. The maximum penetration depth occurs at 10 wt.% with h_{max}=10.7 um, meanwhile 35 wt.% acquires minimum penetration depth with h_{max}=10.2 um at the different peak load. As a result, the load indentation depth curve indicates that a lower percentage of filler loading yields a softer surface while for a higher percentage of filler loading yields a hardened surface. In summary, Figures 11 and 12 also gives a clear view that when the percentage of filler loading increases, the penetration of the indenter decreases steadily.

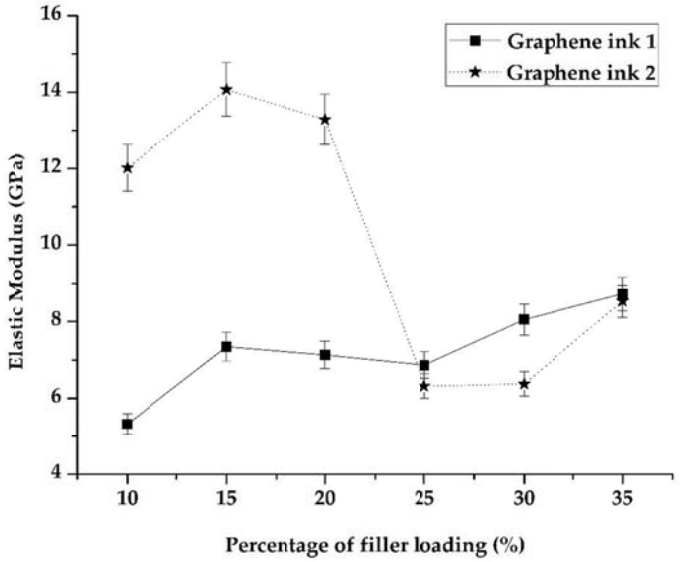

Figure 10: The graph of elastic modulus against filler loading

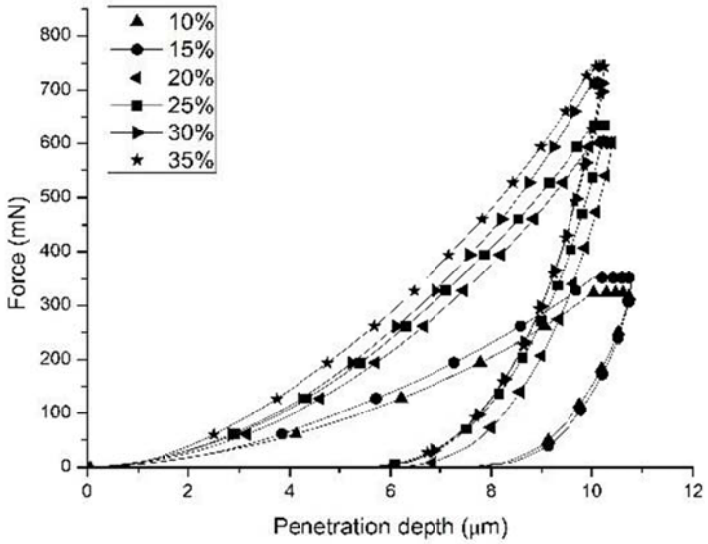

Figure 11: The load indentation curve for GNP ink without thermal effect (graphene ink 1)

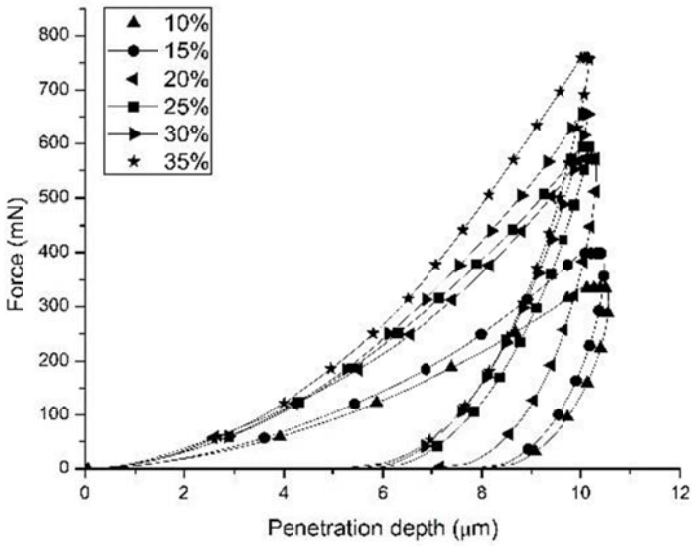

Figure 12: The load indentation curve for GNP ink with thermal effect (graphene ink 2)

3.4 Surface Roughness

In this study, the parameter used to assess the surface roughness was the average of roughness, Ra. Ra is the arithmetic average of surface height that is measured across a surface. In addition, it is a simple average of the height across the microscopic peaks and valleys. The result of surface roughness for six (6) filler loadings is shown in Table 4. Based on this table, the value of the surface roughness obtained is not consistent and uniform. The filler for 10 wt.% and 15 wt.% GNP ink without thermal effect have low surface roughness, which are 1.422 μm and 1.524 μm as compared to the surface roughness of GNP ink with thermal effect, which are 2.984 μm and 1.750 μm. The results for 10 wt.% to 20 wt.% of GNP ink without thermal effect also have stable consistency as compared to GNP ink with thermal effect. The lowest surface roughness, which means that it has the smoothest surface for GNP ink without thermal effect is 30 wt.% with 0.511 μm while for GNP ink with the thermal effect is 25 wt.% with 0.400 μm. The results for higher filler loading are slightly increasing for both conditions with 1.178 μm and 1.075 μm.

Figure 13 shows the graph of surface roughness against the filler loading. The surface roughness is barely the same for both conditions due to the thixotropic behavior of the ink and poor leveling. These lead to pore formation and very large height and depth between the two-line edge (Faddoul *et. al*., 2012). Surface roughness is one of many factors affecting electrical properties. According to Faddoul in 2012, it was estimated that surface roughness increases with the increase of filler content and viscosity. Furthermore, a study by Suherman in 2013 showed that the surface regularity, flatness, and microstructure are dependent on ink viscosity. Smooth surface allows continuous conductive line

formation without shorting risk, hence the hybrid shows a lower resistance compared to single fillers (Faddoul *et. al*., 2012).

Table 4: The values of surface roughness

Filler loading	Surface roughness, (μm)			
	GNP ink without thermal effect	Average	GNP ink with thermal effect	Average
10 wt.%	0.981	1.422	3.421	2.984
	2.125		2.799	
	1.160		2.733	
15 wt.%	0.993	1.524	2.0145	1.750
	2.993		0.677	
	0.588		2.558	
20 wt.%	1.327	1.543	0.358	0.446
	1.650		0.487	
	1.654		0.494	
25 wt.%	1.306	1.051	0.315	0.400
	1.084		0.360	
	0.763		0.524	
30 wt.%	0.652	0.511	0.748	1.106
	0.523		1.361	
	0.359		1.209	
35 wt.%	0.863	1.178	1.671	1.075
	0.601		0.646	
	2.071		0.908	

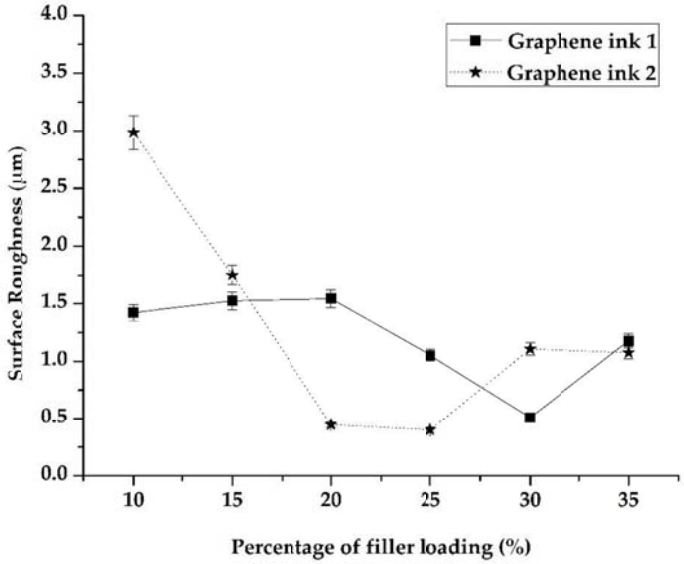

Figure 13: The graph of surface roughness against filler loading

4. CONCLUSION

Through the formulation of ink, all the processes including mixing, printing, and curing processes can be performed to fabricate the ink on the substrate. After the fabrication had been carried out, the behavior of conductive ink was investigated through electrical, mechanical, and morphological tests for GNP/epoxy conductive ink including the electrical and mechanical properties affected by

temperature, which was supplied during the mixing method, and the percentage of filler loading. However, the temperature of the mixing method did not give significant changes in mechanical properties and surface roughness. The percolation threshold for GNP was 30 wt.% at room temperature. Furthermore, the hardness increased with an increased percentage of elastic modulus. The trend contradicted for the hardness as the percentage of loading increased.

5. ACKNOWLEDGEMENT

Special thanks to the Advanced Manufacturing Centre (AMC) and Fakulti Kejuruteraan Mekanikal (FKM), Universiti Teknikal Malaysia Melaka (UTeM) for providing the laboratory facilities.

REFERENCES

Abdullah, S.I. & Ansari, M.N.M. (2015). Mechanical properties of graphene oxide (GO)/epoxy composites. *HBRC J.*, **11**: 151-156.

Atif, R., Shyha, I. & Inam, F. (2016). Mechanical, thermal, and electrical properties of graphene-epoxy nanocomposites—A review. *Polym.*, **8**,: 281.

Chandrasekaran, S. (2014). *Development of nano-particle modified polymer matrices for improved Improved fibre reinforced composite.* Doctoral dissertation, Universitätsbibliothek der Technischen Universität Hamburg-Harburg, Germany.

Chatterjee, S., Nafezarefi, F., Tai, N.H., Schlagenhauf, L., Nüesch, F A. & Chu, B.T.T. (2012). Size and synergy effects of nanofiller hybrids including graphene nanoplatelets and carbon nanotubes in mechanical properties of epoxy composites. *Carbon*, **50**: 5380-5386.

Deng, D., Jin, Y., Cheng, Y., Qi, T. & Xiao, F. (2013). Copper nanoparticles: aqueous phase synthesis and conductive films fabrication at low sintering temperature. *ACS Appl. Mater. Infer*, **5**: 3839-3846.

Eawwiboonthanakit, N., Jaafar, M., Ahmad, Z., Ohtake, N. & Lila, B. (2017). Fabrication of PEDOT: PSS / graphene conductive ink printed on flexible substrate. *Solid State Phenom.* 264: 70-73.

Faddoul, R., Reverdy-Bruas, N. & Blayo, A. (2012). Formulation and screen printing of water based conductive flake silver pastes onto green ceramic tapes for electronic applications. *Mater. Sci. Eng.*, 177: 1053-1066.

Gao, M., Li, L. & Song, Y. (2017). Inkjet printing wearable electronic devices. *J. Mater. Chem. C*, **5**: 2971-2993.

Huang, L., Huang, Y., Liang, J., Wan, X. & Chen, Y. (2011). Graphene-based conducting inks for direct inkjet printing of flexible conductive patterns and their applications in electric circuits and chemical sensors. *Nano Resear.*, **4**:675-684.

Huang, X., Leng, T., Zhang, X., Chen, J.C., Chang, K. H., Geim, A.K. & Hu, Z. (2015). Binder-free highly conductive graphene laminate for low cost printed radio frequency applications. *Appl. Phys. Lett.*, **106**: 203105.

Ismail, N., Salim, M. A., Naroh, A., Saad, A.M., Masripan, N.A., Donik, C. & Dai, F. (2020). The behaviour of graphene nanoplatelates thin film for high cyclic fatigue. *Int. J. Nanoelectr. Mater.*, **13**: 305-326.

Kucinskis, G., Bajars, G. & Kleperis, J. (2013). Graphene in lithium ion battery cathode materials: A review. *J. Power. Sources*, **240**: 66-79.

Lau, P.H., Takei, K., Wang, C., Ju, Y., Kim, J., Yu, Z. & Javey, A. (2013). Fully printed, high performance carbon nanotube thin-film transistors on flexible substrates. *Nano Lett.*, **13**: 3864-3869.

Lee, Y., Choi, J.R., Lee, K.J., Stott, N.E. & Kim, D. (2008). Large-scale synthesis of copper nanoparticles by chemically controlled reduction for applications of inkjet-printed electronics. *Nanotech*, **19**: 415604.

Leng, T., Huang, X., Chang, K., Chen, J., Abdalla, M.A. & Hu, Z. (2016). Graphene nanoflakes printed flexible meandered-line dipole antenna on paper substrate for low-cost RFID and sensing applications. *IEEE Antenn. Wirel. Propag. Lett..*, **15**: 1565-1568.

Lu, K. (2012). *Nanoparticulate Materials: Synthesis, Characterization, and Processing*. John Wiley & Sons, Hoboken, New Jersey.

Mokhlis, M., Salim, M.A., Masripan, N.A., Saad, A.M., Sudin, M.N., Omar, G. & Caridi, F. (2020). Nanoindentation of graphene reinforced epoxy resin as a conductive ink for microelectronic packaging application. *Int. J. Nanoelectr. Mater.*, **13**: 407-418.

Nash, C., Spiesschaert, Y., Amarandei, G., Stoeva, Z., Tomov, R.I., Tonchev, D. & Glowacki, B.A. (2015). A comparative study on the conductive properties of coated and printed silver layers on a paper substrate. *J. Electron. Mater.*, **44**: 497-510.

Nie, X., Wang, H. & Zou, J. (2012). Inkjet printing of silver citrate conductive ink on PET substrate. *Appl. Surf. Sci.*, **261**: 554-560.

Oliver, W.C. & Pharr, G.M. (2004). Measurement of hardness and elastic modulus by instrumented indentation: Advances in understanding and refinements to methodology. *J. Meter. Res.*, **19**: 3-20.

Rosa, P., Câmara, A. & Gouveia, C. (2015). The potential of printed electronics and personal fabrication in driving the internet of things. *Open J. Internet Things*, **1**: 16-36.

Saad, H., Salim, M.A., Masripan, N.A., Saad, A.M. & Dai, F. (2020). Nanoscale graphene nanoparticles conductive ink mechanical performance based on nanoindentation analysis. *Int. J.Nanoelectr. Mater.*, **13**: 439-448.

Singh, E., Meyyappan, M. & Nalwa, H.S. (2017). Flexible graphene-based wearable gas and chemical sensors. *ACS. Appl. Mater. Inter.*, **9**: 34544-34586.

Suherman, H., Sahari, J. & Sulong, A. B. (2013). Effect of small-sized conductive filler on the properties of an epoxy composite for a bipolar plate in a PEMFC. *Ceram. Int.*, **39**: 7159-7166.

Tang, L. C., Wan, Y. J., Yan, D., Pei, Y. B., Zhao, L., Li, Y.B. & Lai, G.Q. (2013). The effect of graphene dispersion on the mechanical properties of graphene/epoxy composites. *Carbon*, **60**: 16-27.

Tortorich, R.P., Shamkhalichenar, H. & Choi, J.W. (2018). Inkjet-printed and paper-based electrochemical sensors. *Appl. Sci.*, **8**: 288.

Van Den Brand, J., de Kok, M., Koetse, M., Cauwe, M., Verplancke, R., Bossuyt, F. & Vanfleteren, J. (2015). Flexible and stretchable electronics for wearable health devices. *Solid-State Electr.*, **113**: 116-120.

Vasiljevic, D.Z., Menicanin, A.B. & Zivanov, L. D. (2013, April). Mechanical characterization of ink-jet printed ag samples on different substrates. *Doctoral Conf. Comput. Electr. Ind. Syst.*. Springer, Heidelberg, Germany, pp. 133-141.

Wajid, A.S., Ahmed, H.T., Das, S., Irin, F., Jankowski, A.F. & Green, M.J. (2013). High-performance pristine graphene/epoxy composites with enhanced mechanical and electrical properties. *Mactomol Mater. Eng.*, **298**: 339-347.

Wei, J., Vo, T. & Inam, F. (2015). Epoxy/graphene nanocomposites–processing and properties: a review. *RSC Adv.*, **5**: 73510-73524.

Wu, W. (2017). Inorganic nanomaterials for printed electronics: a review. *Nanoscale*, **9**: 7342-7372.

MEASUREMENT OF OPTIMAL STRETCHABILITY GRAPHENE CONDUCTIVE INK PATTERN BY NUMERICAL ANALYSIS

Ameeruz Kamal Ab Wahid[1,2], Mohd Azli Salim[2,3*], Murni Ali[4], Nor Azmmi Masripan[2,3], Feng Dai[5] & Adzni Md. Saad[3]

[1]Jabatan Kejuruteraan Mekanikal, Politeknik Sultan Azlan Shah (PSAS), Malaysia
[2]Advanced Manufacturing Centre, Universiti Teknikal Malaysia Melaka (UTeM), Malaysia
[3]Fakulti Kejuruteraan Mekanikal, Universiti Teknikal Malaysia Melaka (UTeM), Malaysia
[4]NanoMalaysia Berhad, 157 Hampshire Place Office, Kuala Lumpur, Malaysia
[5]China Railway Eryuan Engineering Group Co., China

[*]Email: azli@utem.edu.my

ABSTRACT

This study determines the optimal stretchability performance of graphene conductive patterns by using maximum principal elastic strain and Von Mises stress analysis. It was performed by using experimental and finite element analysis (FEA) modelling approaches. The experimental work was initiated by obtaining the optimal formulation of the conductive ink based on the resistivity values and 20 wt.% of graphene nanoplatelets (GNP) was selected. Then, the Young's modulus and Hardness values for this formulation were determined to become the input for the FEA modelling. Six different types of pattern were developed for FEA analysis, which are the straight-line, sine wave, semi-circle, serpentine, zigzag and horseshoe as the straight-line pattern becomes the baseline. The sine wave pattern produced the best results as the percentage different with the baseline pattern in terms of maximum principal elastic strain and Von Mises stress were the largest with the value of 37 times lower. This is due to the fact that the sine wave has more edge and depicts the spring-like behaviour which produces better stretchability. The increased length of the pattern also contributes to stretchability performance. Furthermore, this study shows that the FEA approach can be utilised in investigating the stretchability performance of conductive ink.

Keywords: *Graphene conductive ink; stretchability; maximum principal elastic strain; Von Mises; ink pattern.*

1. INTRODUCTION

Stretchable and conductive materials have been widely used in electronic equipment and health care (Ha *et al.*, 2018). It is also expected to be widely used for electronic equipment in the future especially in automotive safety. Stretchable conductive ink (SCI) is one of the automotive safety applications of stretchable and conductive materials. Numerous forms of conductive inks with specific fillers such as polymers, carbon nanotubes, and metal nanoparticles or organic metal complexes for the creation of conductive patterns have been produced (Yang & Wang, 2016). Among these, graphene-based inks have been the most favoured metal inks and are under rapid development for flexible electronics applications. Because of the strong van der Waals forces between adjacent layers, the graphene sheets are inherently stacked together. Then, it is difficult to exfoliate and distribute graphite nanosheets evenly into a polymer matrix (Xue *et al.*, 2019).

Flexibility and expandability are the main features of the SCI while maintaining high conductivity levels. The layout of a standard driver health monitoring system is designed to continuously monitor parameters related to drivers, vehicles, and the environment by obtaining data from a variety of sensors and taken from the driver's body, interior, and exterior of the vehicle. Different types of drivers give different results due to the detection of mechanical pressure and strain, temperature variations, and bio-potential changes in the human body (Ha *et al.*, 2018).

A sine wave screen printed pattern using a stretchable conductive ink on a stretchable substrate is more stretchable than a similarly fabricated straight line pattern. Stretchability in the printed conductor context is defined as the percentage change in resistance of the printed conductor when exposed to induced uni-axial stress. The lower the change in resistance is better for the stretchability (Zhang *et al.*, 2018). The employment of wavy patterns is an intuitive mechanical technique to enhance the stretchability of stretchable electronics. The hypothesis is that the wavy or meandering patterns will behave like a spring coil, which will open up when they are stretched and should exhibit higher stretchability (Mohammed, 2017). It can be stretched with the same amount as a straight-line pattern but depicts a smaller increase in resistivity.

Hsu *et al.* (2010) published a paper describing the stretching behaviour of horseshoe-shaped wavy conductor copper lines which were created using a photolithographic process and covered on both sides within a Polydimethylsiloxane (PDMS) substrate. They have stretchability up to 100% before exhibiting electrical rupture. Jahanshahi *et al.* (2013) also discussed the horse-shoe patterns, which demonstrated that the meandering patterns with circular shapes exhibit a lower amount of plastic strain. The samples were prepared using a printed circuit board (PCB) approach and a thin film-based, polyimide supported approach. Both papers demonstrated that the horseshoe pattern exhibits lower stress than a straight-line and the highest stress concentration can be found in the crest of the horseshoe (Hsu *et al.*, 2010; Jahanshahi *et al.*, 2013).

The use of conductive nanomaterials for printed electronics must overcome two major challenges: first, similar to bulk metal, the printed patterns need high electrical conductivity and second, the nature of the substrate material is not affected (especially for plastic electronics) and needs to achieve high electrical conductivity under relatively light conditions (Kamyshny & Magdassi, 2019). Both of these challenges are important for conductive ink because the conductive nanomaterial content needs to be high. The higher its concentration in the ink, the better electrical conductivity which also needs flexible substrates compatibility and excellent bending stress tolerance (Yang & Wang, 2016).

Graphene has the greatest potential as high-performance absorption material due to its many attractive properties, including unique structure effects, high specific surface area, and high conductivity (Saad *et al.*, 2020). Graphene as a filler is capable of enhancing the performance, functionality as well as durability of many applications for the next generation of electronic devices, composite materials, and energy storage devices due to its outstanding electrical, mechanical, and thermal properties (Olabi *et al.*, 2021). The use of graphene as a filler element is because of its low cost and high conductivity, which is suitable for industrial-scale production. Most processes of graphene ink use organic solvents such as N-methyl-2-pyrrolidone (NMP) and Dimethylformamide (DMF), which are hazardous, low-concentration, and unsustainable which prohibits their usage in industrial production (Pan *et al.*, 2018). The use of GNP mixing with epoxy resin and hardener is sufficient to formulate a simple and low-cost high yield electrical conductive adhesives (ECA) route production process that is highly desirable for the practical application of graphene inks (Tran *et al.*, 2018).

The research work aimed to demonstrate the comparative difference in strain and stress caused by stretching the screen printed straight-line pattern (baseline) and a curving wave pattern. An experimental investigation was conducted to explore the resistivity of the conductive inks**.** By using experimental results as the input parameter for material properties in FEA modelling, the estimation of the maximum principal elastic strain can be calculated. The differential in strain and stress during stretching could also be optimised by determining the fatigue in different pattern lines. It can be estimated using the maximum principal elastic strain and equivalent stress (Von Mises stress) obtained through FEA modelling. Von Mises stresses were used to evaluate the stress distribution in the conductive ink patterns because a higher Von Mises stress provides a strong indication of a greater possibility of failure (Spazzin *et al.*, 2013). After achieving the stated aim above, an attempt was also made to determine the best-printed conductor pattern with the most optimal stretchability by using maximum principal elastic strain and Von Mises stress obtained from FEA modelling.

2. METHODOLOGY

2.1 ECA Sample Preparation

The epoxy / graphene ink formulations were prepared using a planetary centrifugal mixer. The curing process or the annealing of ECA after the mixing process used the high temperature oven. The new formulation of stretchable conductive ink was characterised in terms of electrical and mechanical behaviours. The formulation of graphene with different filler loadings was characterised to determine and select the suitable ECA, which can satisfy the functionality. The ECA was fabricated with the most basic shape or pattern and tested with electrical and mechanical behaviours (Strehmel *et al*., 2015). In this research, there were three main materials used to formulate the conductive ink. The main materials for ECA formulation are shown in Table 1.

Table 1: Main materials of conductive inks.

Materials	**Descriptions**
Graphene nanoplatelets (GNP) powder	As filler elements
Araldite M or CY 212 (epoxy resin)	As binder elements (to bind the particles)
Huntsman polytheramine D230 (hardener)	To harden or dry the mixtures

GNP as filler element, Araldite® as epoxy resin, and Huntsman polytheramine as hardener were used as the main material for this research which received without further modification. All the raw materials (GNP, epoxy, and hardener) were precisely weighed using an analytical balance. The properties of GNP available from the product datasheet were presented in Table 2.

Table 2: Properties of GNP.

Specification	
Form	**Powder**
Surface area	50-80 m^2/g
Average flake thickness	15 nm
Average particle size	5 µm
Density	0.03 – 0.1 g/cm^3

For the filler loading experiment, the change in the percentage of graphene mass mixed with the epoxy as a binder was to determine the resistance of the ECA. All samples were tested according to each applicable test to evaluate certain characterisations and the average data of these samples become the final result. The conductive ink typically includes between about 40-60 % of conductive particles and between about 30-50 % of binder. The stretchable conductive ink patterns may be stretched more than twice of their length without breaking or rupturing (Longinotti & Aliverti, 2017). The formulation contained 0.5 g of resin and hardener was prepared using a planetary centrifugal mixer. To obtain the filler percentage, the filler domain was divided into 5 samples starting with 10 wt.% with each sample interval representing 5 wt.% and followed by mixing with 70-90 wt.% of binder (epoxy) and hardener (30% of epoxy weight) respectively.

Table 3 tabulates the formulation of the materials in the development of the ECAs, in which the GNP was varied, between 10 wt.% to 30 wt.%. The hardener (30% of epoxy weight) as a curing agent was mixed with graphene and epoxy to obtain the total amount of formulations, followed by a mixing process with all involving materials using a planetary centrifugal mixer at 2000 rpm for three minutes. The planetary centrifugal mixing was used to achieve a uniform dispersion and to enable high precision in the desecration of high-viscosity adhesives and materials whose viscosities are increased by added fillers. After the mixing process, the formulation was done by the doctor blading method on the glass slide substrate before the curing process. Figure 1 shows the thickness (t_s), width (w), and length (l) of the conductive inks with the values of 0.1, 3.0 and 25.4 mm respectively.

Table 3: Formulation of the materials in the development of the ECAs.

Sample	GNP		Epoxy		Hardener (g)
	(wt.%)	(g)	(wt.%)	(g)	
S10	10	0.050	90	0.450	0.135
S15	15	0.075	85	0.425	0.128
S20	20	0.100	80	0.400	0.120
S25	25	0.125	75	0.375	0.113
S30	30	0.150	70	0.350	0.105

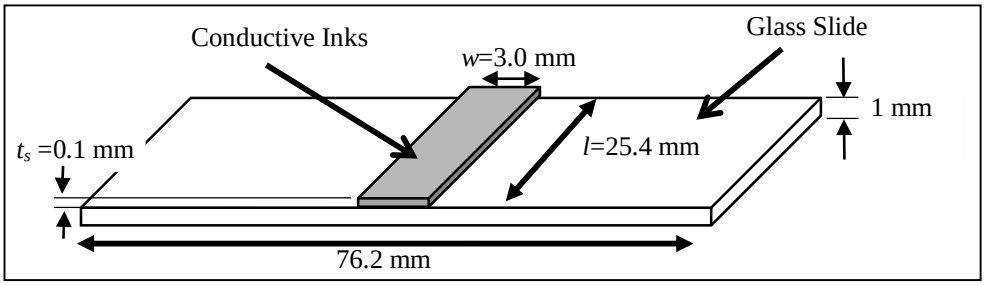

Figure 1: Pattern thick layer dimension of ECA on the glass slide.

All formulations were cured in a high temperature oven at 150 °C for 30 min. Higher temperatures or longer annealing times are required in order to increase conductivity (Karagiannidis *et al.*, 2017). But there is a risk of using higher temperatures and longer annealing times e.g. higher than 300 °C with sintering time over 3 hours are not practical to be implemented on flexible substrates (Yang & Wang, 2016). After the curing process, all specimens were normalised at room temperature for about 24 h. Figure 2 shows the specimen of 20 wt.% (S20) on a glass slide with three minutes of mixing times.

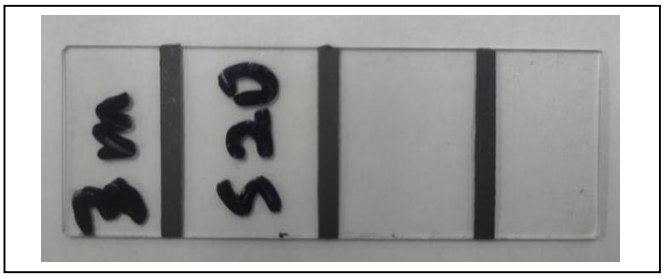

Figure 2: Specimen with three layers on the glass slide.

2.2 ECA Experimental

After all the samples had been prepared, each of these samples underwent an electrical characterisation analysis to obtain the sheet resistance values by using the In-Line Four-Point Probe. The input was ranged between 10 nA to 100 mA at three different locations per stripes, which equals to nine data per sample (refers to Figure 3 for the sample marking points). Then, the data was analysed to get the volume of resistivity for all the samples and the average of the volume of resistivity and standard deviation values were determined. All samples were tested according to each applicable test standard to evaluate certain characterisation in which the average data of these samples become the final result.

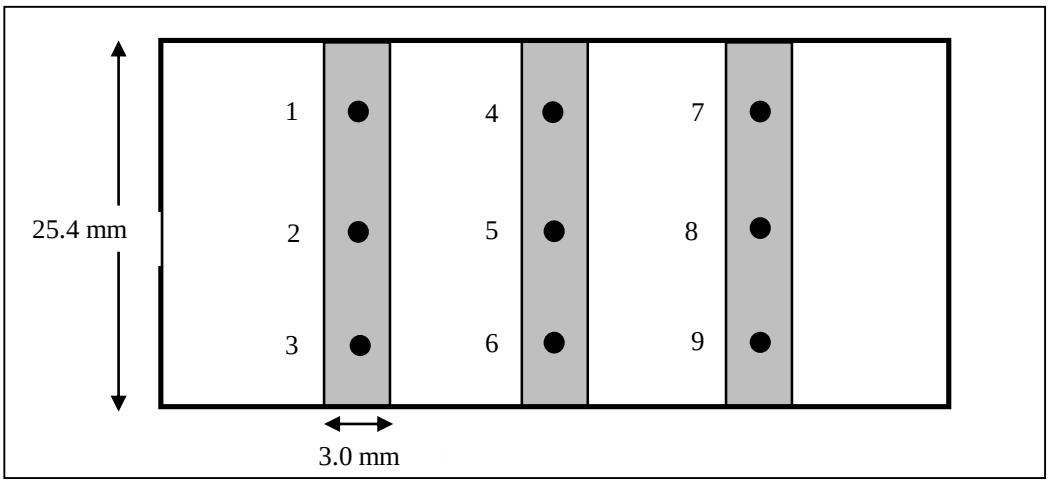

Figure 3: Schematic of printed conductive ink on a glass slide with 9 marking points.

The measurement of resistivity (average sheet resistance, the average volume of resistivity and, standard deviation values) of the filler loading percentage measurements are presented in Table 4. S10 and S15 samples represent GNP of 10 wt.% and 15 wt.% respectively showed very high values of sheet resistance, volume of resistivity, and standard deviation. The loss modulus was higher for both 10 wt.% and 15 wt.% of graphene than the storage modulus throughout the range of the measured stresses, indicating that these formulations displayed liquid-like behaviour. This makes the ratio of 10 wt.% and 15 wt.% are not suitable for use in the circuit because of their high resistance value. Samples S20, S25, and S30 did not show a significant difference between all the results because the use of binder content was less for the three samples. It makes the samples possess less liquid behaviour after the curing process. Salim *et al*. (2020) stated that the higher the vehicle (binder polymer and solvents) content of the ink, the more uneven the printed ink layer surface when produced using the offset lithography method.

Table 4: Measurement of resistivity of the test samples.

Sample	Sheet Resistance, Average (R/sq)	Volume of Resistivity, Average (Ω.cm)	Standard Deviation (Ω.cm)
S10	55.5161×10^6	330.7764×10^3	296.8148×10^3
S15	1.1436×10^6	6.8139×10^3	1.5557×10^3
S20	4.1799×10^3	24.9046	4.4328
S25	3.9784×10^3	23.7043	3.5152
S30	2.1655×10^3	12.9024	3.2456

Figure 4 illustrates a very high volume of resistivity for a sample of 10 wt.% with the value of 330.7764 x 10^3 Ω.cm as compared to other samples. This makes the sample of 10 wt.% was rejected. There was a significant difference in the average volume of resistivity between 15 wt.% with the value of 6.81396 x 10^3 Ω.cm, and 20 wt.% with the value of 24.9046 Ω.cm. This makes the GNP at 15 wt.% was also rejected because of high resistance recorded. Samples 20, 25 and 30 wt.% did not show significant differences in terms of the average volume of resistivity. This indicates that the resistance found in samples 20, 25 and 30 wt.% did not significantly affect the flow rate in the circuit.

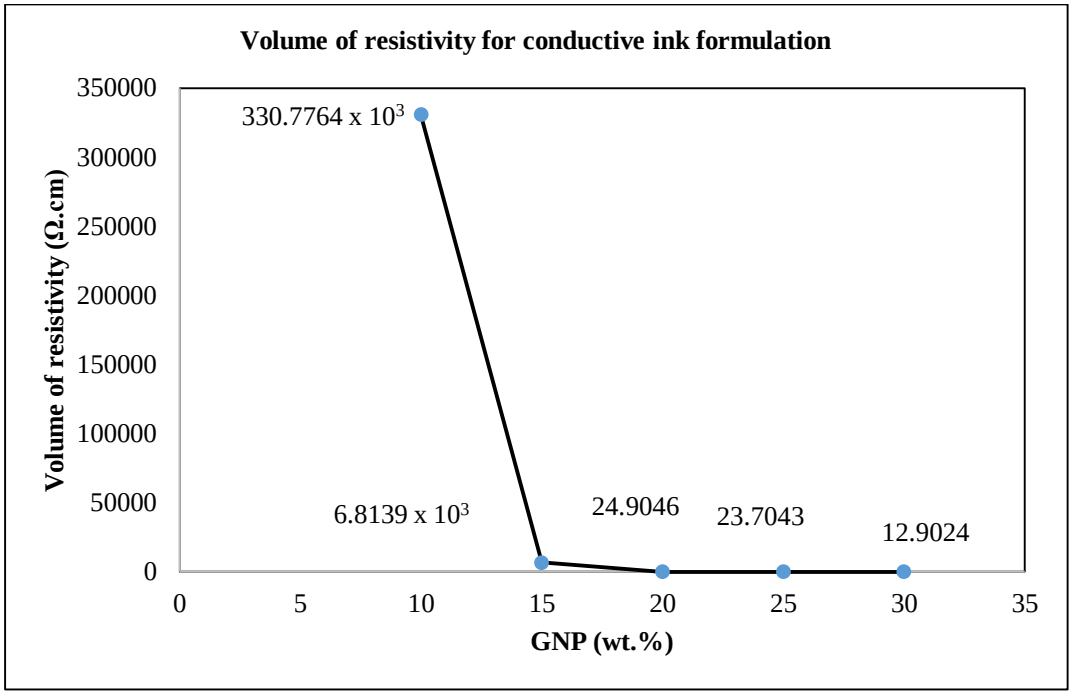

Figure 4: Volume of resistivity (Ω/cm) on conductive ink formulation.

2.3 Mechanical Characterisation Analysis

From the data in the filler loading experiment, sample S20 was selected for mechanical characterisation analysis because it is more economical in terms of material usage. Most studies on graphene and its application are focused on the reduction of graphene materials since graphene can be produced cost-effectively on an industrially accessible scale, and the graphene functional groups enable its hydrophilicity and processability of formulations (Tran *et al.*, 2018). For this experiment, the main focus is on the mechanical properties, which can determine the strength of the material. The hardness of ECAs samples was tested using a nano-indentation machine. In determining the suitable maximum force for this experiment, several force values were tested by using the selected sample from the filler loading experiment. Nano-indentation depth was carefully adjusted to avoid cracking and rupture of the formulation and consequently loss of protective effect. Table 5 shows the Young's Modulus and hardness values with different maximum forces.

Table 5: Young's Modulus and hardness value for determining suitable maximum force.

Sample	Maximum Force (mN)	Maximum Depth (μm)	Young's Modulus, E (GPa)	Hardness (MPa)
S20	50	2.8261	10.27	28.932
	60	3.0399	9.569	30.772
	80	4.5182	7.621	17.555
	100	4.2886	8.698	25.19
	150	5.5434	15.49	20.318
	175	12.4837	1.912	4.956

From the same table, 150 mN was a suitable maximum force to perform this experiment because the value of Young's Modulus was the highest as compared to other maximum forces. The maximum load was measured as a function of penetration depth of the indenter into the surface (Batakliev *et al.*, 2018), and may penetrate too deep if the load is too high, but a major concern when measuring thin films because the results would then be influenced by the substrate's properties. On the other hand, if the load

is too low, then the roughness of the specimen surface will affect the results. The maximum force of 175 mN as compared to others has a maximum depth that is too high. This allows the depth of penetration to get too deep and results in a sharp decrease in the Young's Modulus and hardness values. The Young's Modulus can determine the physical properties of the formulation by allowing the bending or stretching of conductive ink circuits. The Young's modulus values from this experiment then were used as the input parameter in FEA of graphene formulation.

2.4 Finite Element Pre-Processing Analysis

The numerical workbench software was used for the FEA of the Knuckle joint. At first, the Knuckle Joint was designed in design **s**oftware, CATIA and then the file was saved as IGES format and imported into the workbench software. The next step was to mesh the model with fine mesh option and a reasonable time was required for the computational process as shown in Figure 5. The finite element was generated using the element size of 1.9 x 10^{-4} mm which makes it from 6915 to 18148 elements depending on the shape of the patterns.

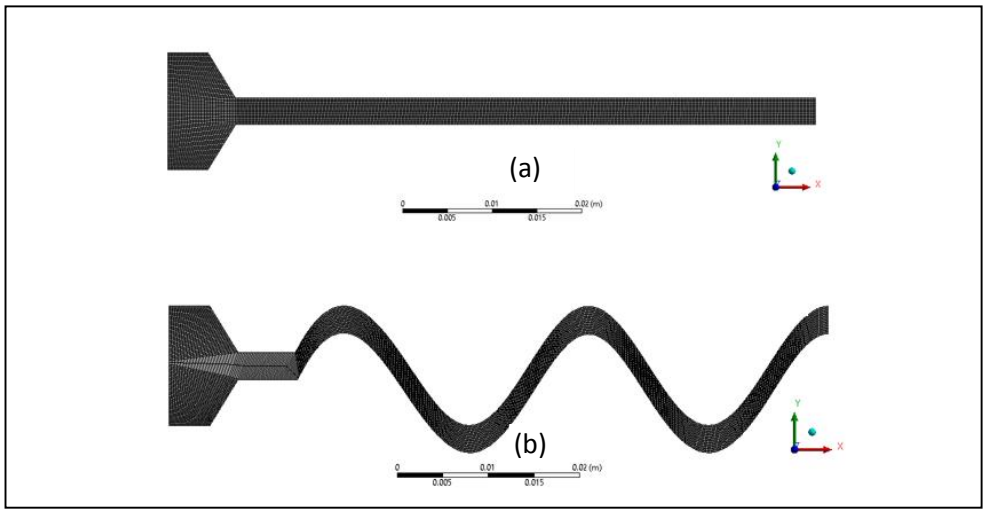

Figure 5: Mesh model of samples. (a) Straight-line pattern. (b) Sine wave pattern

2.5 FEA

The FEA of ink stresses on a wavy pattern and a straight-line screen-printed pattern was analysed using ANSYS software to simulate strain and stress behaviour of the circuit under mechanical loading. The ink was modelled as a layered structure to simulate the screen-printed process. The objective of the analysis was to assess the influence of the six different printed shapes, straight-line (baseline), sine wave, semi-circle, serpentine, zigzag and horseshoe on the resultant stresses on the printed pattern. The shapes were printed on the same substrate using similar printing and curing processes. This analysis was designed to estimate which shape would exhibit lower stress by its percentage value. The material properties obtained from the previous experimental results and ink supplier were shown in Table 6. Then, the numerical results were compared with the experimental results.

Table 6: Material properties used for simulation analysis.

Materials	Properties				
	Young's modulus (Pa)	Poisson's ratio	Density (kg/m^3)	Thermal conductivity (W/m °K)	Resistivity (Ω.m)
Graphene	15.49 x 10^9	0.149	2200	5300	0.249

The FEA model was developed with 0.1 mm ink thickness for all patterns. Because of symmetrical

geometry along the X direction, a half model was deployed. According to Mohammed (2017), the stretch reliability test requires a few percent stretch, e.g. 10% or 20% to determine the estimated lifetime under a particular strain of the stretchable conductors. The 20% of elongation stress was deployed uni-axially along the X-axis as shown in Figure 6.

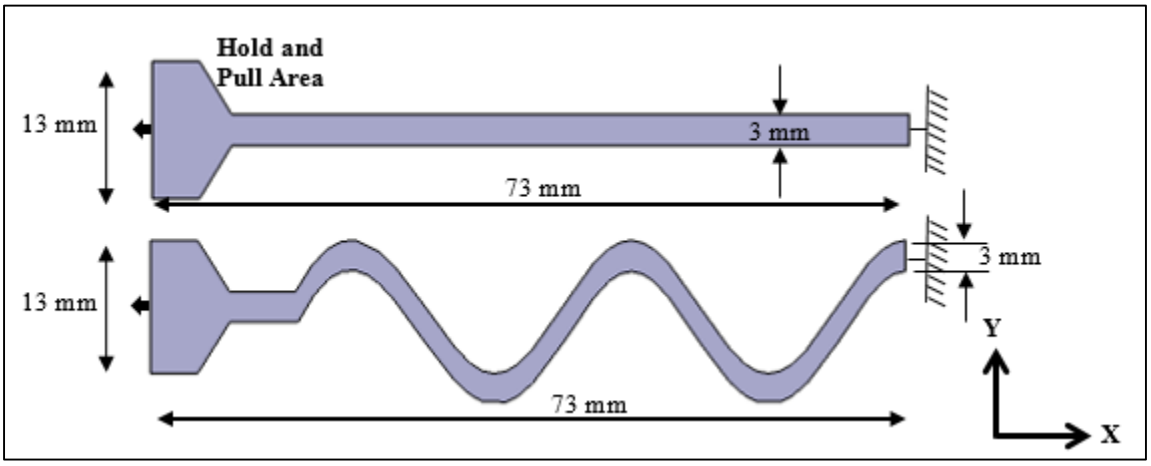

Figure 6: FEA symmetrical half model.

3. RESULTS AND DISCUSSIONS

3.1 Comparison between Straight Line (Baseline) and Other Wavy Patterns

Table 7 shows the percentage difference between straight line (baseline) and other patterns on the maximum principal elastic strain and Von Mises stress. Percentage difference is used to evaluate the difference between other patterns with the straight line (baseline) pattern. The negative value generated indicates the lack of other pattern values against the straight line (baseline) pattern. The comparison of the percentage to the straight line (baseline) shows that the sine wave is the lowest and is followed by horseshoe, zigzag, semi-circle, and serpentine. The percentage difference value of sine wave is -189.57% for maximum principal elastic strain and -187.62% for Von Mises stress. It can also be stated that the sine wave percentage value is 189.57% lower at maximum principal elastic strain and 187.62% lower at Von Mises stress than a straight line (baseline). This can be seen through the observation in Figures 7 and 8, where the curves found in the wavy pattern greatly reduce the value of strain and stress on the pattern. All percentage differences are solved using the following equation:

$$\%\ \ Difference = \frac{V_1 - V_2}{\left(\frac{V_1 + V_2}{2}\right)} \times 100 \tag{1}$$

where:

V_1 = Other patterns (maximum principal elastic strain or Von Mises stress) value
V_2 = Straight line (maximum principal elastic strain or Von Mises stress) value

Figures 7 and 8 show the comparisons of the maximum principal elastic strain and Von Misses stress for six patterns. It can be seen that the maximum principal elastic strain and equivalent stress (Von Mises stress) behaviours are different for all the patterns. Based on the result, the maximum principal elastic strain and equivalent stress are lower on a more curving pattern because the curving pattern has the edge. The type (b) pattern in Figures 7 and 8 attain the smallest amount of maximum principal elastic strain and Von Mises stress among all the six types because of the sine wave pattern depicting the spring coil behaviour. The length of the pattern also gives an effect to the stress and strain value. If the length increases, the Von Mises stress value is reduced below 1000 MPa, thus improving the mechanical reliability of the device (Zulkefli *et al.*, 2017). However, type (a) attains the highest value of stress among all the patterns because it does not possess high stretchability behaviour.

Table 7: FEA results summary for the half model.

Component	Type	Pattern	Maximum Principal Elastic Strain	% Difference to Baseline (%)	Von Misses Stress (MPa)	% Difference to Baseline (%)
Ink	a	Straight Line (Baseline)	0.5452	0	8060	0
	b	Sine Wave	0.0146	-189.57	257.34	-187.62
	c	Semi-Circle	0.0839	-146.65	1300.1	-144.44
	d	Serpentine	0.1777	-101.67	2552.1	-103.80
	e	Zigzag	0.0263	-181.59	396.21	-181.26
	f	Horseshoe	0.0193	-186.32	298.55	-185.71

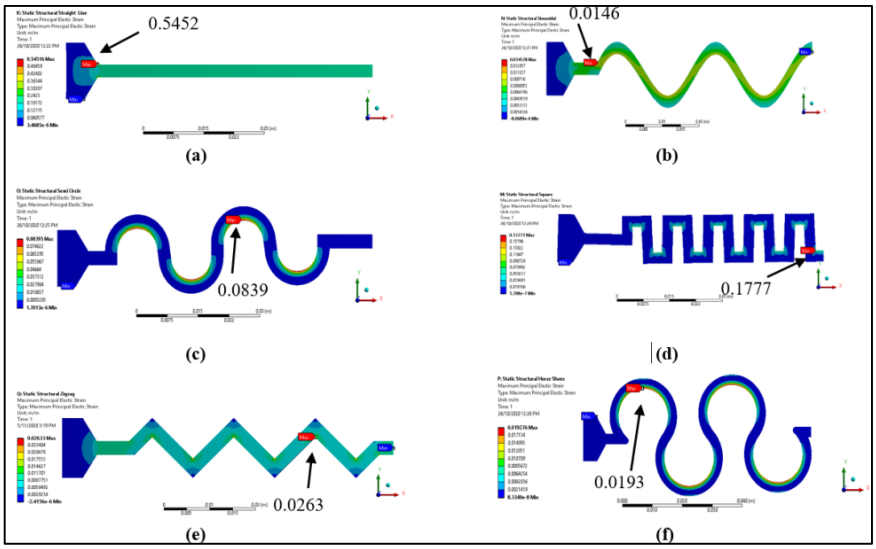

Figure 7: Maximum Principal Elastic Strain. (a) Straight line trace; (b) Sine wave trace; (c) Semi-circle trace; (d) Serpentine trace; (e) Zigzag trace; (f) Horseshoe trace.

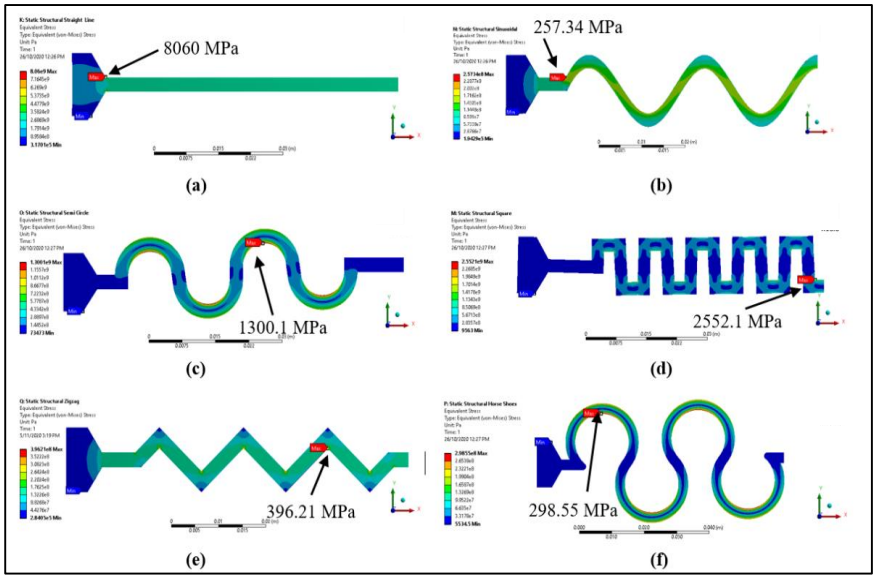

Figure 8: Von Mises Stress. (a) Straight line trace; (b) Sine wave trace; (c) Semi-circle trace; (d) Serpentine trace; (e) Zigzag trace; (f) Horseshoe trace.

From the FEA performed, the maximum principal elastic strain for each of the six patterns was calculated by assuming that the lowest maximum principal elastic strain would offer the best stretchability performance. From the observation in Figure 7, the straight-line pattern can withstand more stress than the other wavy patterns. By using the maximum principal elastic strain, the sine wave pattern has the largest percentage difference when comparing to the straight-line (baseline) pattern, which is about 37 times less strain. The nearest values of maximum principal elastic strain and equivalent stress (Von Mises) to the straight-line pattern are the serpentine pattern, which is three times lower with the percentage values of -101.67% and -103.8% respectively. Based on the results in Figures 7 and 8, the correlation between maximum principal elastic strain and Von Mises stress to the percentage difference in Table 7 between baseline and other patterns for both analyses are almost the same. This indicates that the 20% strain and stress exposure on both analyses have similar effects on the conductive ink behaviour between the straight-line (baseline) pattern and other curving patterns.

The FEA results demonstrate that the sine wave pattern has better stretchability as compared to a straight-line pattern. The sine wave pattern behaves like a coil and opens up under stretch whereas the straight line does not have that capability. The results are similar to what is available in the literature (Hsu *et al*., 2010) for a horseshoe type pattern that was not screen printed. The FEA estimates the stretchability of the straight-line pattern to be 37 times worse than the sine wave pattern after 20% of strain exposure. This FEA value assumes an ideal situation with no delamination between the ink and the substrate, no stress cycling, and no variations during the manufacturing process. Nevertheless, the FEA model does validate the assumption and the FEA results that a sine wave pattern tends to behave like a spring coil and exhibits less strain versus a straight-line pattern.

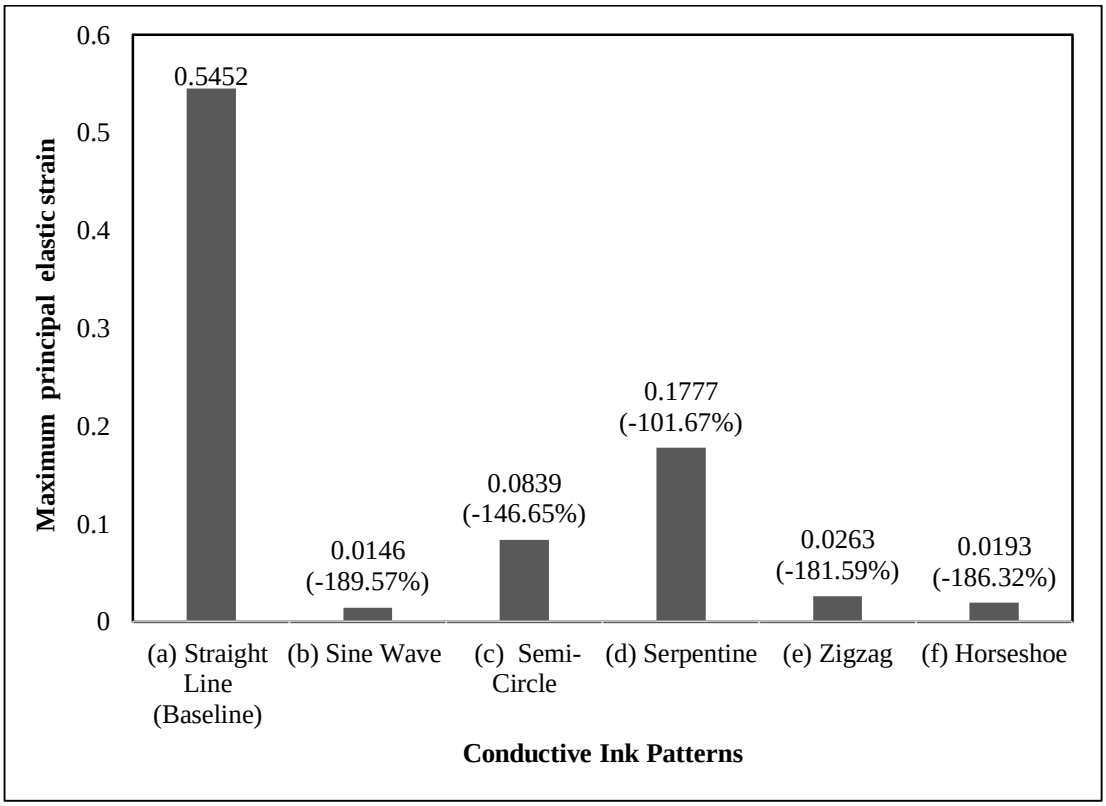

Figure 9: Percentage difference between the straight line (baseline) pattern and other wavy patterns using maximum principal elastic strain.

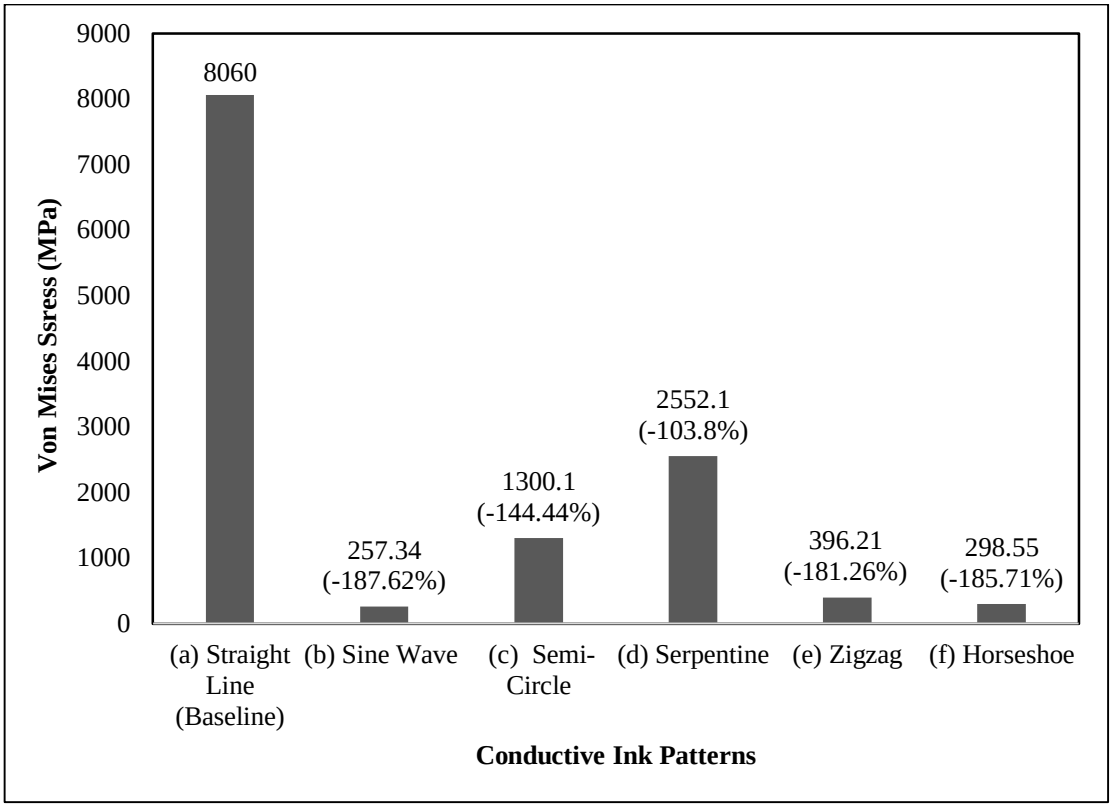

Figure 10: Percentage difference between the straight line (baseline) pattern and other wavy patterns using Von Mises stress.

4. CONCLUSION

The study was carried out successfully in demonstrating the optimal stretchability performance of graphene conductive patterns by using maximum principal elastic strain and Von Mises stress analysis. In terms of maximum principal elastic strain and Von Mises stress, the sine wave pattern provided the best results as the percentage difference from the baseline pattern was the highest with a value of 37 times lower. It is because the sine wave has more edge and depicts the spring-like behaviour. The increased length of the pattern also contributes to stretchability performance. The findings also demonstrated that the optimal screen-printed pattern for stretchability could be designed by using FEA modelling and the maximum principal elastic strain could be used to estimate the increase in the change of resistance during stretching.

ACKNOWLEDGEMENT

Special thanks to the Advanced Manufacturing Centre (AMC) and Fakulti Kejuruteraan Mekanikal (FKM), Universiti Teknikal Malaysia Melaka (UTeM) for providing the laboratory facilities.

REFERENCES

Batakliev, T., Georgiev, V., Ivanov, E., Kotsilkova, R., Di Maio, R., Silvestre, C. & Cimmino, S. (2019). Nanoindentation analysis of 3D printed poly (lactic acid) -based composites reinforced with graphene and multiwall carbon nanotubes. *J. Poly. Sci.*, **136**: 47260.

Ha, M., Lim, S. & Ko, H. (2018). Wearable and flexible sensors for user-interactive health-monitoring devices. *J. Mater. Chem. B*, **6**: 4043-4064.

Hsu, Y.Y., Gonzalez, M., Bossuyt, F., Axisa, F., Vanfleteren, J. & De Wolf, I. (2010). The effect of

pitch on deformation behaviour and the stretching-induced failure of a polymer-encapsulated stretchable circuit. *J. Micromech. Microeng.*, **20**: 075036.

Jahanshahi, A., Gonzalez, M., van den Brand, J., Bossuyt, F., Vervust, T., Verplancke, R. & De Baets, J. (2013). Stretchable circuits with horseshoe shaped conductors embedded in elastic polymers. *Jpn. J. Appl. Phys.*, **52**: 05DA18.

Kamyshny, A. & Magdassi, S. (2019). Conductive nanomaterials for 2D and 3D printed flexible electronics. *Chem. Soc. Rev.*, **48**: 1712-1740.

Karagiannidis, P.G., Hodge, S.A., Lombardi, L., Tomarchio, F., Decorde, N., Milana, S. & Ferrari, A.C. (2017). Microfluidization of graphite and formulation of graphene-based conductive inks. *ACS Nano.*, **11:** 2742-2755.

Longinotti-buitoni, G. & Aliverti, A. (2017). *U.S. Patent No. 9,817,440: Garments Having Stretchable and Conductive Ink.* U.S. Patent and Trademark Office, Washington, DC.

Mohammed, A.A. (2017). *Development of a New Stretchable and Screen Printable Conductive Ink*, Doctoral dissertation, University of Maryland, Maryland.

Olabi, A.G., Abdelkareem, M.A., Wilberforce, T. & Sayed, E.T. (2021). Application of graphene in energy storage device–A review. *Renew. Sust. Energ. Rev.*, **135**: 110026.

Pan, K., Fan, Y., Leng, T., Li, J., Xin, Z., Zhang, J. & Hu, Z. (2018). Sustainable production of highly conductive multilayer graphene ink for wireless connectivity and IoT applications. *Nat Commun*, **9**: 1-10

Saad, H., Salim, M. A., Masripan, N. A., Saad, A. M., & Dai, F. (2020). Nanoscale graphene nanoparticles conductive ink mechanical performance based on nanoindentation analysis. *Int. J.Nanoelectr. Mater.*, **13**: 439-448

Salim, M.A., Dai, F., Saad, A.M., Masripan, N.A., Dmitriev, A. N., Naroh, A. & Akop, M.Z. (2020). Prediction effects on internal resonance wave of metallic conductive ink in rotational motion behaviour *Int. J.Nanoelectr. Mater.*, **13**: 295-304

Shen, C. & Oyadiji, S.O. (2020). The processing and analysis of graphene and the strength enhancement effect of graphene-based filler materials: A review. *Mater. Today Phy.*, **15**: 100257.

Spazzin, A.O., Costa, A.R., Correr, A.B., Consani, R.L.X., Correr-Sobrinho, L. & dos Santos, M.B.F. (2013). Effect of bar cross-section geometry on stress distribution in overdenture-retaining system simulating horizontal misfit and bone loss. *J. Biomech.*, **46**: 2039-2044.

Strehmel, V., Berdzinski, S., Ehrentraut, L., Faßbender, C., Horst, J., Leeb, E. & Wenda, A. (2015). Application of ionic liquids in synthesis of polymeric binders for coatings. *Prog Org Coat*, **89**: 297-313.

Tran, T.S., Dutta, N.K. & Choudhury, N.R. (2018). Graphene inks for printed flexible electronics: graphene dispersions, ink formulations, printing techniques and applications. *Adv Colloid Interfac*, **261**: 41-61.

Yang, W. & Wang, C. (2016). Graphene and the related conductive inks for flexible electronics. *J Mater Chem C*, **4**: 7193-7207.

Young, R. J., Liu, M., Kinloch, I. A., Li, S., Zhao, X., Vallés, C. & Papageorgiou, D.G. (2018). The mechanics of reinforcement of polymers by graphene nanoplatelets. *Compos. Sci. Technol.*, **154**: 110-116.

Yu, H., Fang, D., Dirican, M., Wang, R., Tian, Y., Chen, L. & Zhang, X. (2019). Binding conductive ink initiatively and strongly: transparent and thermally stable cellulose nanopaper as a promising substrate for flexible electronics. *ACS Appl. Mater. Inter.*, **11**: 20281-20290.

Zhang, B., Lei, J., Qi, D., Liu, Z., Wang, Y., Xiao, G. & Chen, X. (2018). Stretchable conductive fibers based on a cracking control strategy for wearable electronics. *Adv. Funct. Mater.*, **28:** 1801683.

Zulkefli, M.A., Mohamed, M.A., Siow, K.S., Majlis, B.Y., Kulothungan, J., Muruganathan, M. & Mizuta, H. (2018). Stress analysis of perforated graphene nano-electro-mechanical (NEM) contact switches by 3D finite element simulation. *Micrisyst. Technol.*, **24**: 1179-1187.

DRAG REDUCTION OF SEPARATE LIFT THRUST (SLT) VERTICAL TAKE-OFF AND LAND (VTOL) COMPONENTS

Zulhilmy Sahwee, Muhd Hariz Asri*, Nadhiya Liyana Mohd Kamal, Norhakimah Norhashim, Shahrul Ahmad Shah & Wan Nursheila Wan Jusoh

Universiti Kuala Lumpur, Malaysian Institute of Aviation Technology, Malaysia

*Email: hariz.asri29@s.unikl.edu.my

ABSTRACT

Vertical take-off and land (VTOL) is a new technology in the unmanned aerial vehicle (UAV) field. Separate lift and thrust (SLT) is identified as the most simplistic design of VTOL UAVs. However, during the forward cruising flight phase, the VTOL component of the UAV will increase the drag. Therefore, the objective of this work is to reduce the drag effect on inactive propulsion system. In order to reduce the drag, several motor fairings and aerodynamic shaft samples was designed and the best design was selected. Each sample was simulated using computational fluid dynamics (CFD) simulation to examine the aerodynamic properties of the design. Subsequently, the samples were tested in a wind tunnel facility to measure the resultant drag. Then, the drag reduction of the designs was analysed and compared to the original design. Based on the results, the most effective design combination was selected to replace the off-the-shelf design. The findings from this work show that the V3.0 motor fairing and forward swept aerodynamic shaft design have the highest drag reduction. The V3.0 motor fairing design has 14.9% drag reduction, while forward swept aerodynamic shaft design has drag reduction up to 25.4%. Therefore, these two designs have been selected to replace the off-the-shelf motor holder and shaft.

Keywords: *Unmanned aerial vehicles (UAV); vertical take-off and lift (VTOL); drag; motor fairing; aerodynamic shaft.*

1. INTRODUCTION

Hybrid vertical take-off and land (VTOL) unmanned aerial vehicle (UAV) is a new fixed-wing UAV platform that has the ability to take off vertically as well as perform hovering motions. This hybrid vehicle is a combination of multirotor and fixed-wing configurations, both of which have advantages and disadvantages (Czyba *et al*., 2018). Multirotor UAVs have the advantage to take-off and land in a confined environment but lack in endurance. On the other hand, fixed-wing UAVs have good endurance but need space and infrastructure for take-off and landing. The hybrid platform will be able to fill the gap between multirotor and fixed-wing UAVs (Stahl *et al*., 2018). It has advantages of both fixed-wing and multirotor UAVs, and to some level, it should be able to eliminate their shortcomings (Abd Rahman *et al*., 2018).

The baseline platform for VTOL UAVs uses the separate lift thrust (SLT) configuration for the vertical lifting propulsion system. This configuration produces more drag than the other types of VTOL UAVs as it uses a separate system for vertical lift, which contributes to additional drag during the forward cruising mode (Hadi *et al*., 2015; Serrano, 2018). Since most of the flight phase of the VTOL aircraft is in forward cruising mode, the performance of the aircraft will be affected. In order to improve the aerodynamic properties of the aircraft, it is important to characterise the drag introduced from the installation of VTOL components and structure. The VTOL structure and components add to the total parasitic drag of the aircraft. The additional VTOL components used are arms, electric propulsion system and propellers. Each of these components adds drag to the aircraft (Stahl *et al.*, 2018).

In developing a VTOL UAV, the challenge is focusing on flight performance and optimising the aerodynamic design of the UAV (Footohi *et al*., 2019). In order to improve the aerodynamic performance of an aircraft, its drag needs to be reduced. Drag is categorised into two groups, which are parasitic drag and induced drag. Parasitic drag is a combination of form drag, interference drag and skin friction drag, whereas induced drag is the drag directly associated with the production of lift. From the study conducted by Goetten *et al.* (2018), an aircraft design needs specific countermeasures to reduce its drag. The study by Stahl *et al.* (2018) aimed to reduce the drag contributed by exposed VTOL rotors to increase aircraft performance. Some other researchers such as Teo *et al.* (2016), explored on propeller blade design to be used specifically for VTOL applications. While several other studies have been conducted to reduce the drag of VTOL components and systems, many of them focus on the propeller drag reduction. Thus, there is a research gap on drag reduction of the vertical lift components.

Therefore, the objective of this research is to reduce the drag of the vertical lift components. A multiple configuration flying wing UAV was chosen as the base platform for this research. It was modified into SLT VTOL configuration that adapts H-frame VTOL arm layout. The drag reduction study is focused on the exposed vertical lift components of the UAV shown in Figure 1. Thus, the drag reduction structures of motor fairing and shaft were designed and tested in this study. Based on the test data, selection of drag reduction structure been made to enfold the exposed vertical lift components.

Figure 1: Vertical lift components of VTOL UAV.

2. VTOL DRAG

It is important that the drag force on an aircraft is minimised to ensure optimum performance of the aircraft (Sahwee *et al*., 2019). In order to minimise drag, it is important to know the drag acting on the aircraft itself. The drag (*D*) of an aircraft is directly proportional with the coefficient of the drag (C_d) of the wing reference area (*S*), dynamic pressure on aircraft, which consist of air density (ρ) and aircraft velocity (*V*). It can be defined by using the following equation (Hoerner, 1965):

$$D = 0.5\, C_d\, S\ \rho\ V^2 \tag{1}$$

In addition to the induced drag of the wings, other components that are in direct contact with airflow will also add drag towards the aircraft. Therefore, C_d consists of the summation of two components which are the lift-induced drag coefficient ($C_{D,i}$)and zero-lift induced drag coefficient ($C_{D,O}$), which is also known as the parasitic drag (Shaffer *et al.*, 2010). C_D is computed using in the following equation:

$$C_D = C_{D,i} + C_{D,O} \tag{2}$$

The variation of drag as a function of airspeed is shown in Figure 2, which indicates that induced drag reduces with airspeed, while parasitic drag increases as airspeed increases.

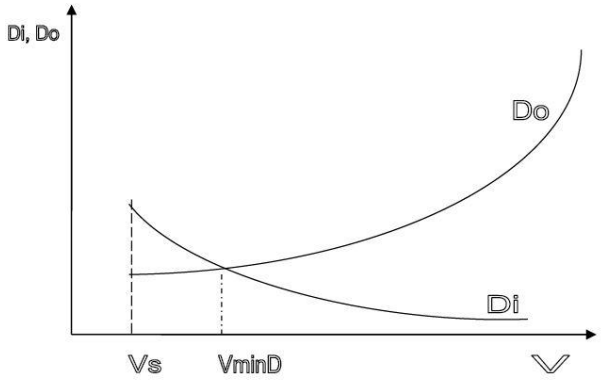

Figure 2: Variations of induced drag (D_i) and parasite drag (D_o) vs velocity (Sadraey, 2009).

Drag can be classified as shown in Figure 3. Induced drag depends on the geometry of the wing, while parasitic drag is influenced by the overall design of the aircraft. In addition, a VTOL aircraft also experiences parasitic drag due to the vertical lifting components of the propulsion system (Asri, Sahwee, & Kamal, 2019).

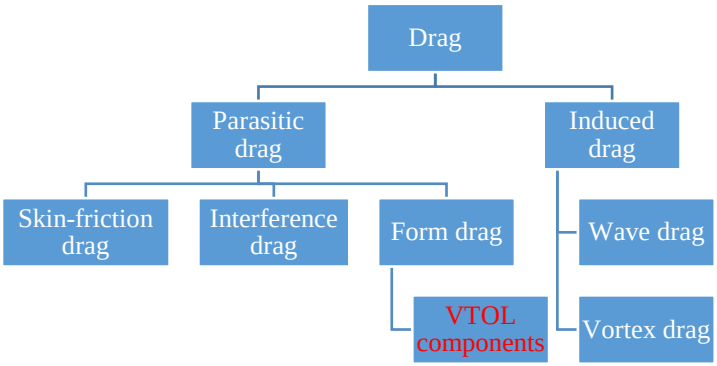

Figure 3: Classification of drag.

The blunt body of the non-lifting component also generates parasitic drag. Since the vertical lift component contributes to the parasitic drag, the drag coefficient is given by Sadraey (2009) based on non-retractable landing gear and strut parasitic drag. The VTOL $C_{D,O}$ is given in the following equation:

$$C_{D,O_{VTOL}} = \sum_{i=1}^{n} C_{D_{VTOL}} \left(\frac{S_{VTOL,i}}{S}\right), \tag{3}$$

where S_{VTOL} is the frontal area of each vertical lift component and S is the wing reference area. The parameter $C_{D_{VTOL}}$ is the drag coefficient of each component, which depends on the design of the VTOL components. The parameter n is the number of vertical components that been used in the UAV. If the diameter of the component is given by d_{comp} and thickness is t_{comp}, the frontal area of component can be computed as follows:

$$S_{VTOL} = d_{comp}\ t_{comp} \tag{4}$$

Equation 4 shows that the design diameter and thickness are major factors that will influence the drag of the vertical lift components. Hence, it is important to analyse each design of the components to enhance the UAV's performance. There are also several researchers that investigate the drag of VTOL components such as Stahl *et al*. (2018), who studied on reducing the drag of an inactive hover rotor by using a rotor storage system. Additionally, Tarnowski *et al*. (2020) conducted research on aerodynamic forces acting on SLT tail boom. The study investigates the effect of wind velocity and angle of attack on the forces generated by and on the tail boom mounted propellers.

In addition to the component drag, there are also other factors that need to be considered in order to improve the overall performance of the UAV (Stahl *et al*., 2018). Therefore, this study will include the additional factors, which are vertical thrust generation and weight to drag ratio.

3. METHODOLOGY

3.1 Flow Simulation

Computational fluid dynamics (CFD) was used in the development process. SolidWorks was used for both meshing and CFD solution. The analysis of CFD comprises of three main stages, which are pre-processing, numerical analysis, and post-processing.

The pre-processing comprises geometry generation and physical modelling (Vasile, 2016). During geometry generation, the computer will calculate the input parameters, which consist of flow conditions, thermal parameters and generation of the mesh network. For the physical modelling, the equations of motion and boundary conditions will be included in the calculation. Then, the second stage includes the numerical analysis or the numerical solutions generation that resolves the partial differential equations iteratively. The last step is the post-processing analysis where it visualises the numerical results or graphs of the solution and generates the final reports. Figure 4 shows the flow trajectory results of the simulation.

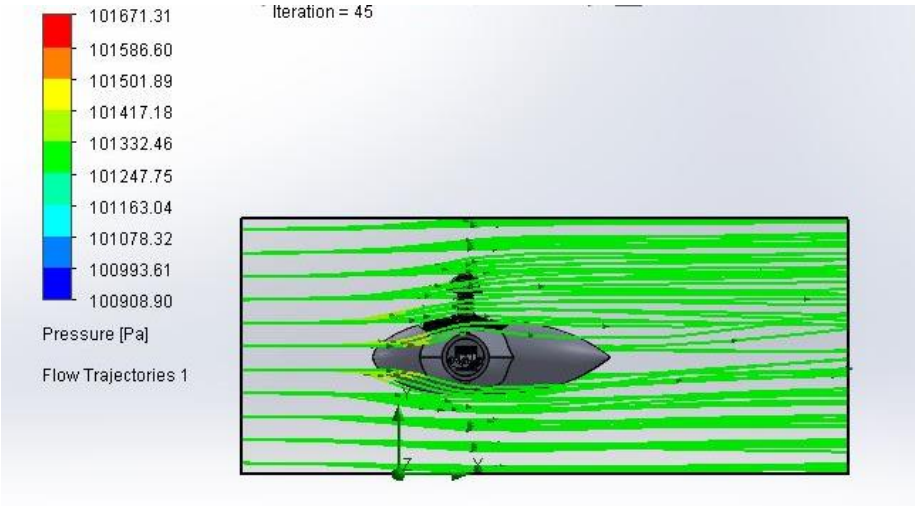

Figure 4: SolidWorks flow simulation test.

3.2 Wind Tunnel Setup and Measurement

The wind tunnel experiment was conducted in the open circuit subsonic wind tunnel in Universiti Kuala Lumpur, Malaysian Institute of Aviation Technology. This wind tunnel is capable of operating at a maximum airspeed of 40 m/s (Sahwee *et al*., 2017). Figure 5 shows the subsonic wind tunnel and its control panel for the experiment.

Figure 5: Subsonic wind tunnel and its control panel.

The test section of the wind tunnel measures 30 x 30 x 30 cm. Measurements were taken for each motor fairing and shaft design by attaching them to the test jig inside the test section. The assembly of the shaft and fairings were mounted on the force balance equipment as shown in Figure 6. This force balance equipment was attached to a load sensor, which enables the drag to be measured in kilogram-force (kgf).

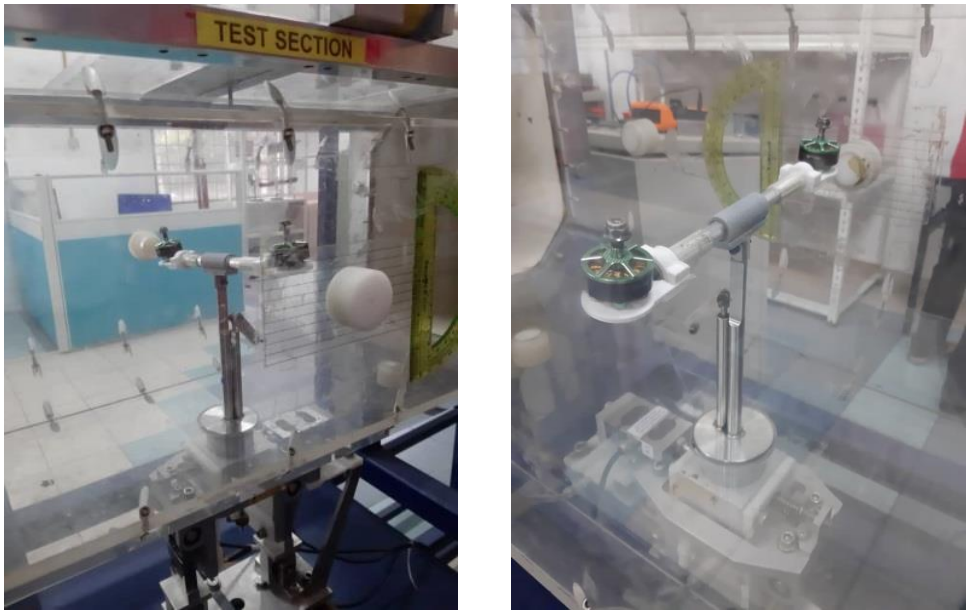

Figure 6: Subsonic wind tunnel test section and test setup arrangement for motor fairings.

4. MOTOR FAIRING

4.1 Design Overview

The effect of drag on five different designs of fairings with various lengths and shapes were investigated as shown in Figure 7. Each of the design has different parameters as tabulated in Table 1. The first three designs, denoted by V1.0, V2.0, and V3.0, were differentiated by their lengths. The other two designs, which were V3.1 and V3.2, are modifications of the V3.0 design, which have smaller surface area and lighter weight. Additionally, there was also a baseline design based on off-the-shelf motor holder.

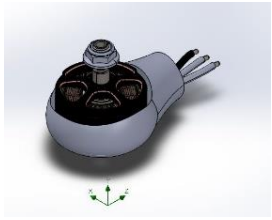

[V 1.0] L = 0.12*d*

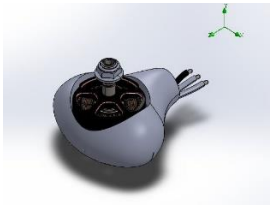

[V 2.0] L = 0.44 *d*

[V 3.0] L = 1.14 *d*

[V 3.1] L = 1.14 *d*(a)

[V 3.2] L = 1.14 *d*(b)

Baseline design

Figure 7: Motor fairing designs used in this study.

Table 1: Fairing design description.

Fairing design	Length	Weight
V 1.0	0.12*d*	6.42 g
V 2.0	0.44*d*	10.5 g
V 3.0	1.14*d*	14.7 g
V 3.1	1.14*d*	13.6 g
V 3.2	1.14*d*	13.6 g
Baseline	-	9.05 g

The length (*L*) of the fairing is shown in Figure 8. It was calculated with respect to the diameter (*d*) of the motor. For example, the V1.0 fairing design was labelled with 0.12*d*, which is defined with 0.12 times the motor diameter. The lengths of the fairings were 0.12*d*, 0.44*d*, 1.14*d*, 1.14*d*(a), and 1.14*d*(b). Other dimensions such as the thickness and width of the fairing were kept constant.

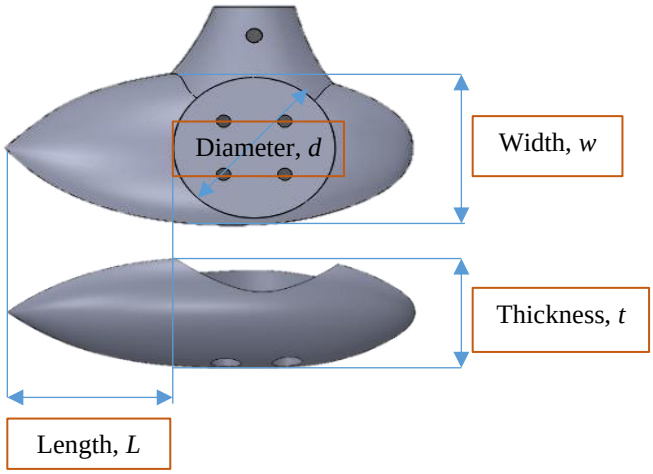

Figure 8: Motor fairing dimension.

In the selection process, all the designs were tested with SolidWorks flow simulation to compare the drag with the baseline motor holder. Later, the desired design was fabricated and tested in the wind tunnel to verify the drag reduction of the design with actual wind condition.

4.2 Flow Simulation Test

Each of the fairing design samples was simulated with varying airspeeds based on VTOL UAV cruising speed, which was between 10 to 20 m/s. The resultant drag exerted towards the fairing was recorded. The boundary condition of the simulation was set to replicate the test section of the wind tunnel. Figure 9 shows that V3.0 with longest fairing length has lowest drag, which is 0.737 N. This indicates that drag is affected by the fairing length. As the fairing length is longer, it reduces the flow separation of the design. The simulation also shows that the drag is directly proportional with airspeeds.

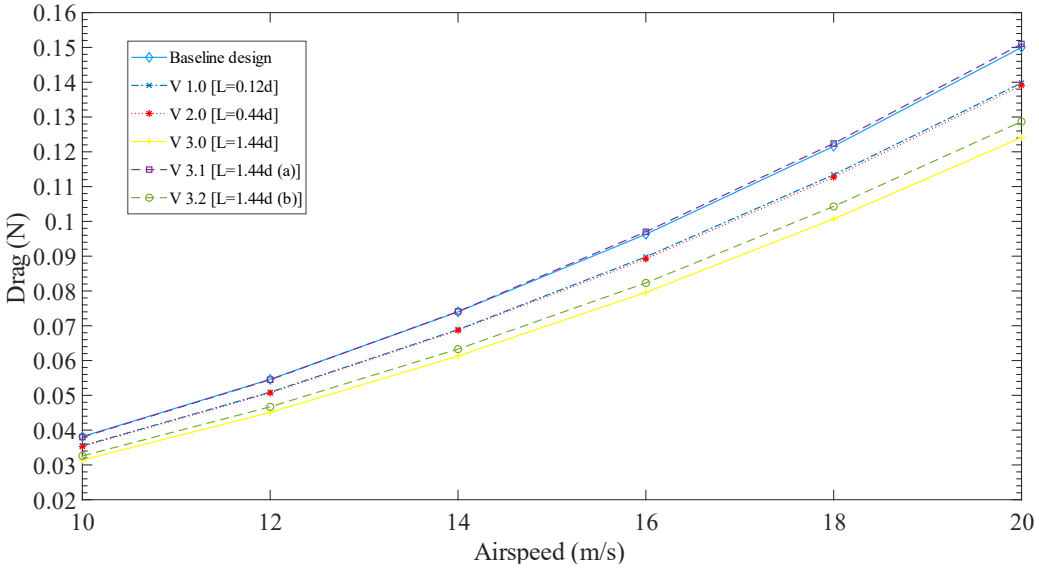

Figure 9: Motor fairing CFD simulation.

Based on the graph in Figure 9, each of the fairing designs shows a reduction in drag as compared to the baseline design. The drag reduction of each design with respect to the baseline design was calculated and shown in Figure 10. V3.0 has the most drag reduction, which reduces 17% of drag. It has been shown that V3.0 has the optimum design to reduce drag on vertical lift motor. This simulation results will then be validated through wind tunnel testing.

4.3 Wind Tunnel Testing

Each of the fairing sample was tested with airspeeds of 10, 12, 14, 16, 18 and 20 m/s. This test replicated the actual flight conditions of the motor fairings. In general, the graph trend in the wind tunnel test results in Figure 11 confirm the simulation results shown in Figure 9. However, there are some inconsistencies in the results for V1.0 and V2.0. V2.0 is found to have the highest drag even though its length is longer than V1.0. This is a slight variation from the simulation results obtained in Figure 9. This is probably caused by some manufacturing tolerance during the fabrication process. As for V3.0 design, both the wind tunnel and simulation show consistent results.

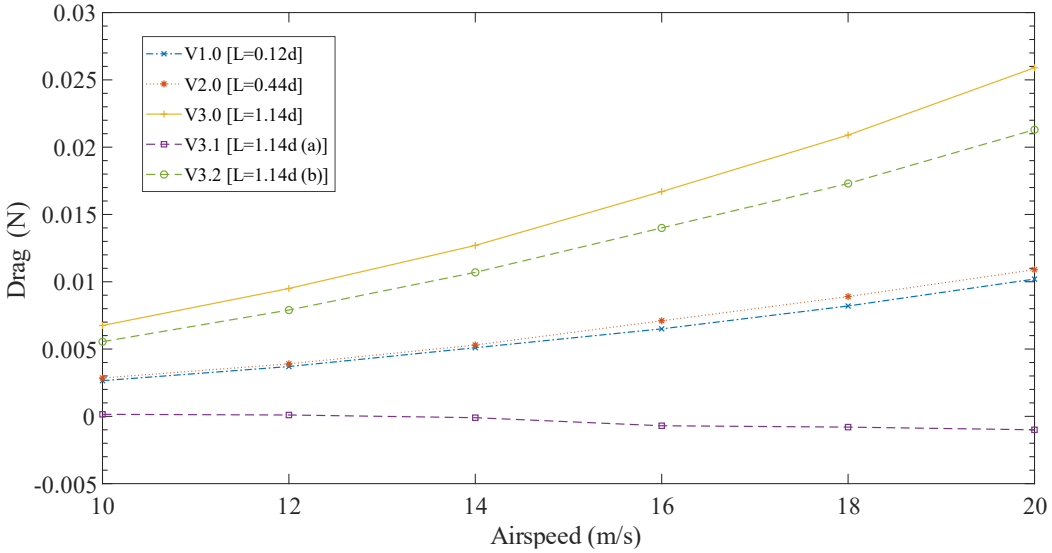

Figure 10: Motor fairing design drag reduction.

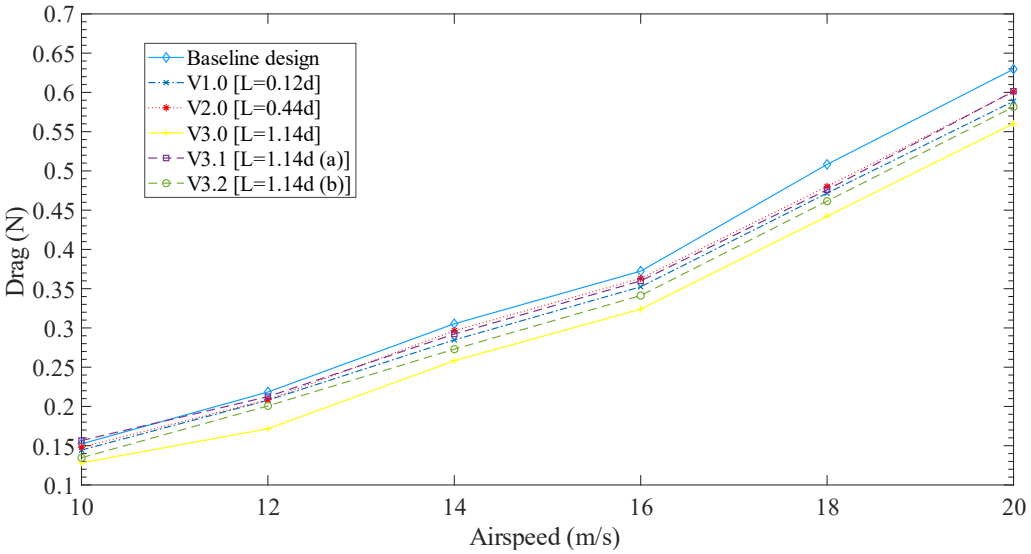

Figure 11: Motor fairing design wind tunnel testing.

The drag reduction of the motor fairing designs with respect to the baseline design is shown in Figure 12. The results show that drag reduction increases with velocity. V3.0 is found to have the highest drag reduction, which is 0.0693 N (14.9%). This proves that the V3.0 design is the optimum design among the other designs.

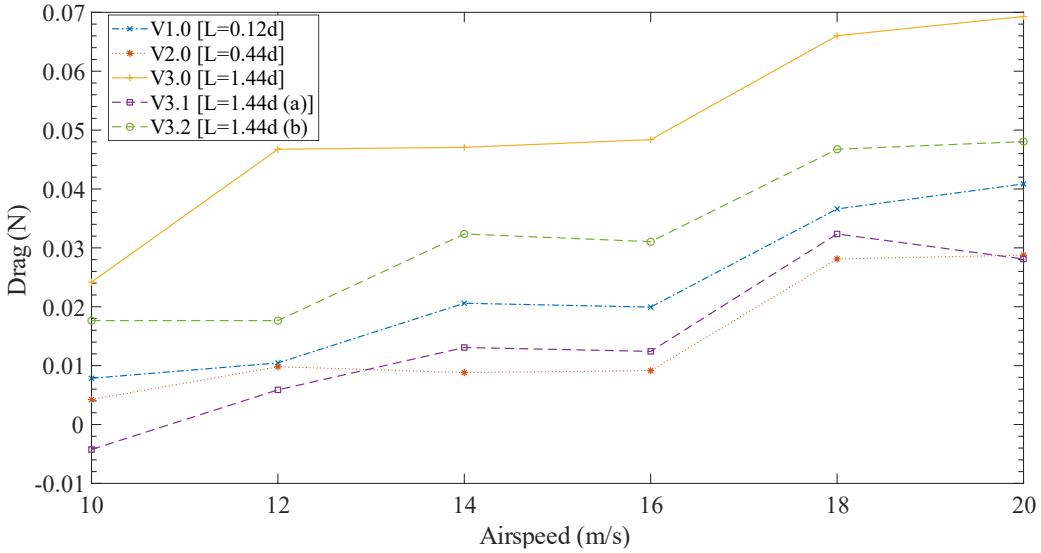

Figure 12: Motor fairing drag reduction.

4.4 Design Consideration

In analysing fairing design performance, apart from drag reduction, there are other factors that need to be considered, which are weight to drag ratio and undesirable effect on vertical thrust generation.

4.4.1 Weight to Drag Reduction Ratio

As discussed in Section 4, a longer fairing length will result in better aerodynamic performance. However, a longer fairing length will add more weight to the UAV. Thus, the ratio between weight of the fairing and drag reduction has been calculated and shown in Figure 13. Low weight to drag reduction ratio indicates a good fairing design.

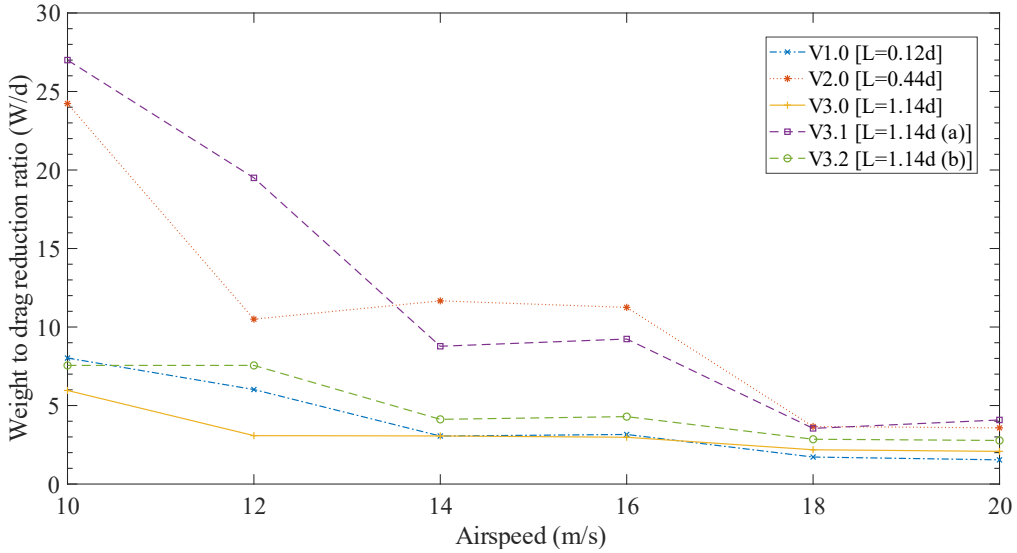

Figure 43: Weight and drag relation.

Based on Figure 13, it is shown that the V3.0 fairing design has the lowest weight to drag reduction ratio. Throughout the airspeed range between 10 to 20 m/s, it has an average ratio of 3.22 as compared to the V1.0 fairing design, which has an average ratio of 3.92. Furthermore, the weight of the design can be further improved by using other manufacturing techniques.

4.4.2 Effect on Vertical Thrust Generation

This consideration is to measure the vertical thrust reduction of each fairing design. This is because surface area of fairing design generates blockage effect in the VTOL configuration. This section details the investigation on thrust reduction percentage of each fairing design with respect to the baseline design. The percentage difference in thrust between each design as compared with the baseline design is recorded in Figure 14. It is found that each fairing design reduces thrust that has been generated by the rotor. However, the thrust difference is minimal, as the highest reduction percentage, recorded by the V3.1 design, was only 6.5%. It is also shown that thrust reduction percentage increases directly proportional with fairing length. As the longer design tends to increase the blockage area below rotor, this will reduce the thrust.

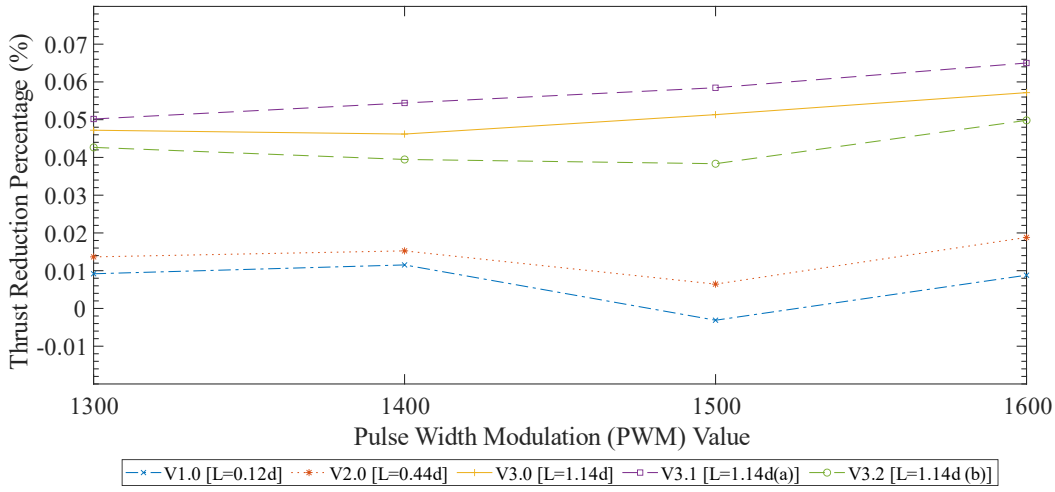

Figure 54: Percentage of vertical thrust generation reduction.

4.5 Fairing Selection

There are several factors that been considered in fairing design selection. The main factor is drag reduction of the component followed by weight to drag ratio and vertical thrust generation effect. As this study focuses on reducing drag on the vertical lift component, the drag reduction factor was given higher priority than other factors, while the other two factors were used to assist in determining the most optimum design selection. The data from the tests conducted were analysed and tabulated in Table 2, where the three factors are divided into specific ratios to indicate the priorities of the factors. The ratios are then multiplied by scores of each design to obtain the cumulative score, which will deduce the most optimum design selection.

Table 2: Design selection table.

Design consideration	Ratio	V1.0	V2.0	V3.0	V3.1	V3.2
Drag reduction	0.5	3	2	5	1	4
Weight to drag reduction ratio	0.4	4	2	5	1	3
Vertical thrust generation	0.1	5	4	2	1	3
Total score		3.6	2.2	4.7	1	3.5

It shown that drag factor has the highest ratio with 0.5. This is because it is crucial to reduce drag on the vertical component during the cruising phase as VTOL UAVs mostly operate in this phase. This is followed by the weight consideration factor, which is to balance out the weight and drag reduction aspects to achieve efficient overall performance of the aircraft. However, the weight difference between fairing designs and baseline design is very small. Therefore, it has less ratio than the drag factor. The vertical thrust generation factor has the least ratio because it is only applied during take-off and landing phase. Thus, it is less crucial as compared to the other factors mentioned before.

Based on the analysis in the table, V3.0 is the most optimum design with cumulative score of 4.7 over maximum score of 5. It has the highest score for first two factors but lower score for the vertical thrust generation factor. However, as the vertical thrust generation difference between each design was minimal, the V3.0 design is not largely affected by this factor. In conclusion, the V3.0 design has been selected as the motor fairing design to replace the off-the-shelf motor holder.

5. AERODYNAMIC SHAFT

Similar to the motor fairing design, the aerodynamic shaft was designed to reduce parasitic drag on VTOL arm shaft during the cruising phase. As this VTOL arm uses a H-frame configuration, it generates high drag during forward flight. Thus, an aerodynamic shaft will cover the conventional shaft from relative wind that will reduce the drag force acting on the VTOL arm shaft.

5.1 Design Overview

The design of the aerodynamic shaft is based on canard and aft tail design on three-surface aircrafts, whereby Kroo (1984) found that this configuration closely approaches the wing tail aircraft configuration performance. Since the base UAV platform used for this study is flying wing configuration with tailless design, an improved VTOL shaft design will be able to increase the performance of the aircraft.

In this paper, three different platforms of VTOL shaft design were tested, as shown in Figure 15. All three designs have same taper ratio of 0.35. These designs were labelled as forward swept tapered, straight tapered and swept back tapered. These designs underwent similar selection process as the motor fairing design. First, CFD simulation was performed, followed by wind tunnel testing to validate the simulation results.

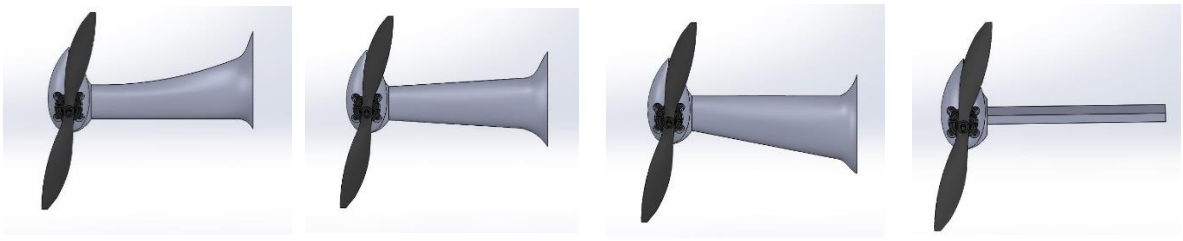

Forward swept Straight Swept back Original shaft

Figure 65: The VTOL shaft designs used in this study.

5.2 Flow Simulation Test

The simulation test used similar setup as the motor fairing CFD simulation. SolidWorks flow simulation was used to replicate the test section of the wind tunnel. The combination of VTOL shaft design samples and previously selected fairing design were used. The resultant drag of each simulation is shown in Figure 16. The graph shows a same trend line with the motor fairing simulation, where the resultant drag increases proportionally with airspeed.

Based on the results in Figure 16, the drag reduction data with respect to the original off-the-shelf shaft design was tabulated and shown in Figure 17. The forward swept shaft design showed the highest drag reduction with 0.29 N at airspeed of 20 m/s. This translated into 20% of reduced drag as compared to the base design.

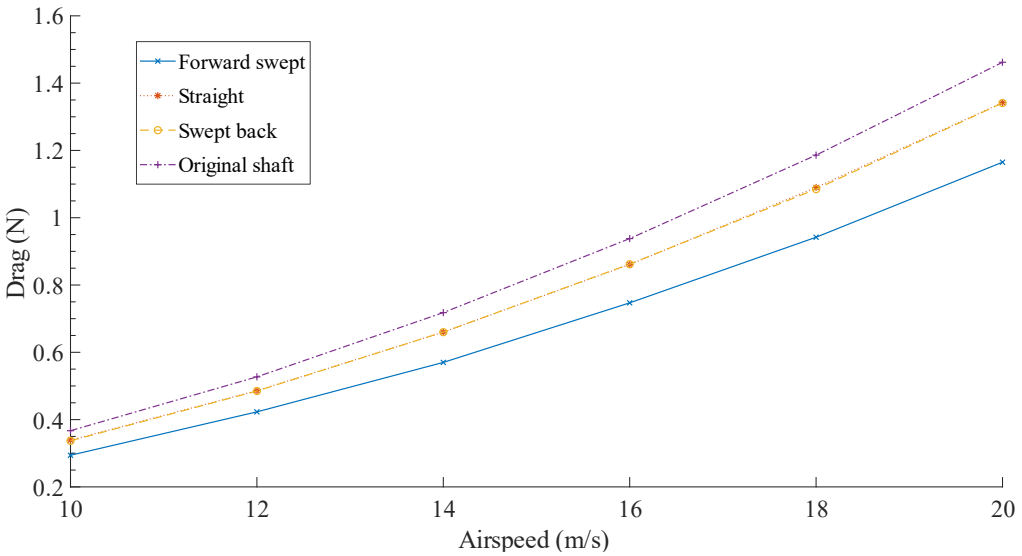

Figure 76: VTOL shaft CFD flow simulation.

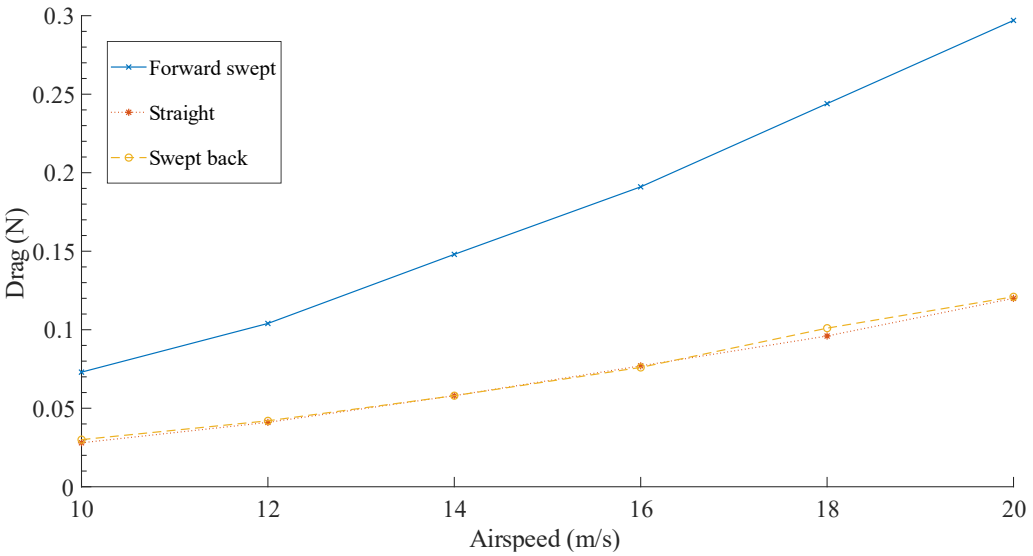

Figure 87: VTOL shaft design drag reduction.

5.3 Wind Tunnel Test

The wind tunnel test was conducted to replicate the flight conditions of the UAV during flight. This test used varying airspeeds of 10 m/s to 20 m/s. The resultant drag of the three shaft designs was measured and shown in Figure 18. The wind tunnel test showed a similar pattern with simulation test results, whereby the forward swept design has the lowest drag, followed by the straight and swept back designs.

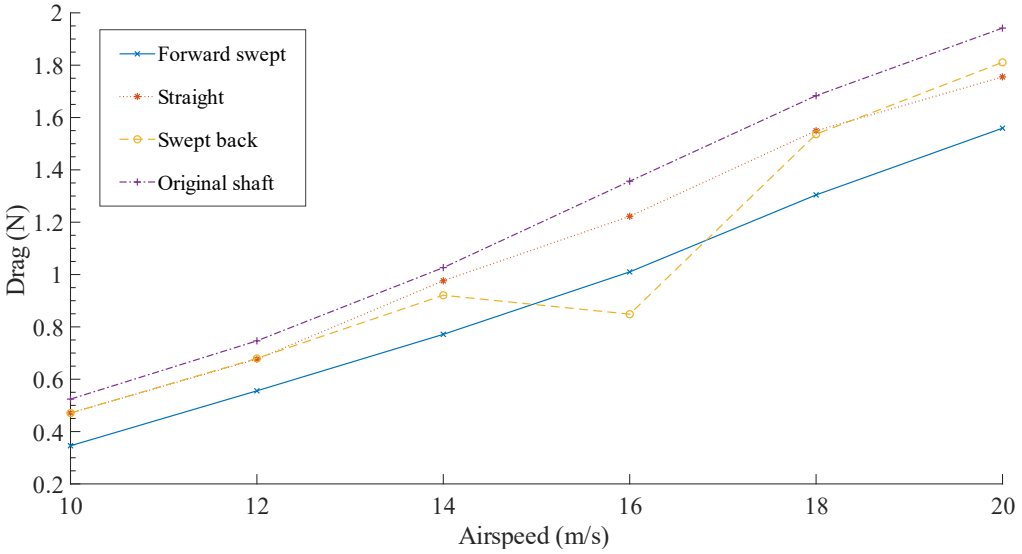

Figure 98: VTOL shaft design result from wind tunnel test.

The drag reduction of each VTOL shaft design was compared with the baseline design and the results are shown in Figure 19. From this graph, it can be seen that the forward swept design reduces the drag up to 0.382 N as compared to the baseline design. This design has the highest average drag reduction percentage with 25.4%.

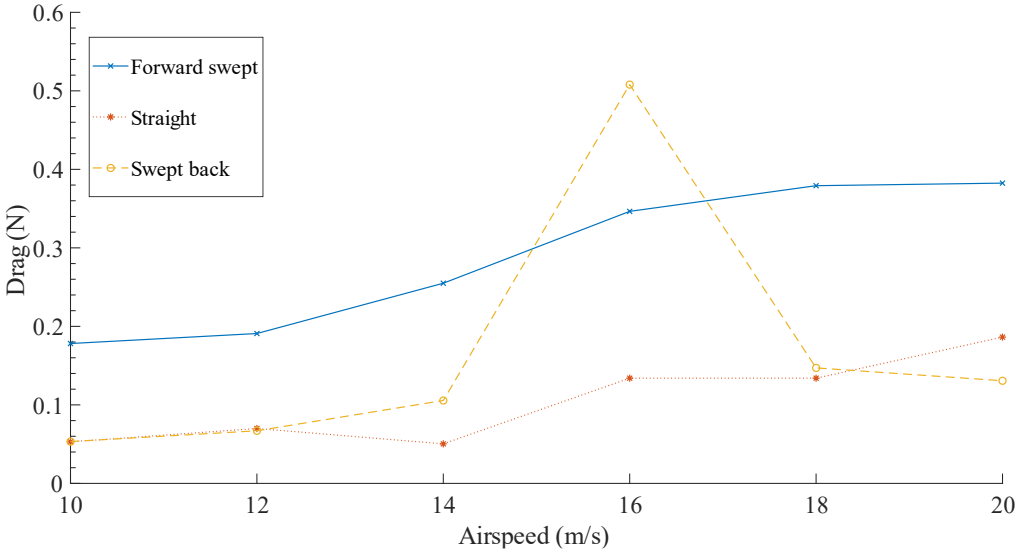

Figure 19: VTOL shaft design drag reduction.

4. CONCLUSION

In summary, each of the design sample was tested in software simulation and validated through wind tunnel tests that replicated the cruising flight phase of VTOL UAVs. The drag reduction was measured by comparing the motor fairing and VTOL shaft design results with an off-the-shelf motor mount and shaft. As to summarise the results, the percentages of drag reductions of the designs are tabulated in Table 3.

Table 3: Drag reduction percentage of each design.

Design	CFD simulation	Wind tunnel
Motor fairing		
V1.0	6.8%	6.0%
V2.0	7.3%	3.8%
V3.0	17.3%	14.9%
V3.1	-0.3%	3.1%
V3.2	14.4%	9.2%
Aerodynamic shaft		
Forward swept	20.2%	25.4%
Straight	8.0%	8.6%
Swept back	8.2%	13.7%

The findings show slight difference in the results between simulation and wind tunnel for the motor fairing design drag tests. These differences are possibly caused by some imperfections during the fabrication process that will slightly changes the aerodynamic characteristic of the samples. However, every tests show that the V3.0 design has the highest drag reduction as compared to the other designs. It can be concluded that V3.0 is the most effective motor fairing design to be installed for VTOL UAVs.

For aerodynamic shaft design, both the simulation and wind tunnel tests show the same trends in their results. From the three VTOL shaft designs that were presented, the forward swept tapered shaft had the highest drag reduction as compared to the off-the-shelf shaft. This indicates that forward swept shaft design is the most suitable shaft design to reduce the resultant drag on the VTOL component.

On the whole, based on the tests that have been conducted, the V3.0 motor fairing combined with the forward swept shaft design have been selected to replace the original off-the-shelf design to improve the aerodynamic performance of the VTOL UAV.

REFERENCES

Abd Rahman, Y.A., Hajibeigy, M.T., Al-Obaidi, A.S.M. & Cheah, K.H. (2018). Design and fabrication of small vertical-take-off-landing unmanned aerial vehicle. *MATEC Web Conf*, **152**: 02023.

Asri, M.H.M., Sahwee, Z. & Kamal, N.L.M. (2019). Propulsion system drag reduction for vertical takeoff and land (VTOL) Unmanned Aerial Vehicle (UAV). *Proc. 2019 Int. Conf. Computer Drone App. (IConDA 2019)*, **1**: 19–22.

Czyba, R., Lemanowicz, M., Gorol, Z. & Kudala, T. (2018). Construction prototyping, flight dynamics modeling, and aerodynamic analysis of hybrid VTOL unmanned aircraft. *J. Adv. Transp.*, **Vol. 2018**: 7040531

Footohi, P., Bouskela, A. & Shkarayev, S.V. (2019). Aerodynamic design of long-range VTOL UAV. *AIAA Scitech 2019 Forum*, 1–17 January 2019, San Diego, California.

Goetten, F., Havermann, M., Braun, C., Gómez, F. & Bil, C. (2018). On the applicability of empirical drag estimation methods for unmanned air vehicle design. *2018 Aviation Tech. Integration Oper. Conf*, 25-29 June 2018, Atlanta , Georgia.

Hadi, G., Budiyono, A., Dewi, P.T., Hadi, G.S., Ramadhan Kusnaedi, M. & Budiyarto, A. (2015). Design of separate lift and thrust hybrid unmanned aerial vehicle. *J. Instrum. Automat. Syst* **2**: 45-51

Hoerner, S.F. (1965). *Fluid-Dynamic Drag*. Hoerner Fluid Dynamics, Bakersfield,California.

Kamal, A.M. & Serrano, A.R. (2018). Design methodology for hybrid (VTOL + Fixed Wing) unmanned aerial vehicles. *Aeron. Aero. Open Access J.*, **2**: 165–176.

Kroo, I. (1984). A general approach to multiple lifting surface design and analysis. *Aircr. Design Syst. Oper. Meet.*, 31 October - 2 November 1984, San Diego, California..

Sadraey M. (2009). *Aircraft Performance Analysis*. VDM Verlag, Saarbrücken, Germany.

Sahwee, Z., Mohd Kamal, N.L., Abdul Hamid, S., Norhashim, N., Lott, N. & Mohd Asri, M. H. (2019). Drag assessment of vertical lift propeller in forward flight for electric fixed-wing VTOL unmanned aerial vehicle. *IOP Conf. Ser.: Mater. Sci. Eng*, **705**: 1

Sahwee, Zulhilmy, Mahmood, A.S., Rahman, N.A. & Sahari, K.S.M. (2017). Wind tunnel evaluation for control transition from elevator to stabilator of small UAV. *J. Eng. Sci. Technol* **12**: 1617–1626.

Shaffer, D.L., Turner, M.S. & Nelson, R.C. (2010). Aerodynamic prediction for low reynolds numbers. Department of Aerospace and Mechanical Engineering, University of Notre Dame, Notre Dame, Indiana

Stahl, P., Rössler, C. & Hornung, M. (2018). Benefit analysis and system design considerations for drag reduction of inactive hover rotors on electric fixed-wing VTOL vehicles. *2018 Aviation Tech. Integration Oper. Conf*, 25-29 June 2018, Atlanta , Georgia.

Tarnowski, A., Goetzendorf-Grabowski, T., Pobikrowska, K., Mechanics, A., Prop, T. & Duct, T. (2020). Wind tunnel aerodynamic investigation of Quadplane. *Aerospace Eu. Conf. 2020*, 25-28 February 2020, Bordeaux, France

Teo, B. S., Weigl, J. D. & Henz, M. (2016). Test and development of efficient blades for use in VTOL aircraft. *2016 11th Int. Conf. Ecol. Vehicles. Renew. Energies. (EVER 2016)*, 6-8 April 2016, Monte Carlo, Monaco.

Vasile, P. (2016). CFD analysis of UAV flying Wing. *Incas Bull.*, **8**: 65–72.

DEVELOPMENT OF VIDEO DATA POST-PROCESSING TECHNIQUE: GENERATING CONSUMER DRONE FULL MOTION VIDEO (FMV) DATA FOR INTELLIGENCE, SURVEILLANCE AND RECONNAISSANCE (ISR)

Muhammad Akmal Asraf Mohamad Sharom*, Mohd Fazuwan Ahmad Fauzi, Abd Razak Sipit & Mohamad Zulkhaibri Mat Azmi

Malaysian Space Agency (MYSA), Ministry of Science, Technology and Innovation (MOSTI), Malaysia

*Email: asraf@mysa.gov.my

ABSTRACT

Full motion video (FMV) is a digital video data format where spatial information is embedded in the video file and is fully compatible to be exploited in standard geographic information system (GIS) environments. FMV, also known as georeferenced video, was initially a military technology that has now been implemented in commercial drone systems. Typically, only high-end industrial and expensive drone systems can be equipped with FMV capabilities. FMV provides many advantages, especially in providing critical information that cannot be obtained from other sources. It adds a fourth dimension to imagery analysis, where the video footprint can be viewed directly on top of maps to provide excellent event fidelity, seamless event progression, and a full context regarding the nature of the location and activities being viewed on the Earth surface. This study aims to research and develop a scientific method to allow the capabilities of FMV technology to be applied into standard video data formats that are captured using consumer drone systems. Consumer drones are the most extensively used drone system nowadays by the private sector, research institutions and even government bodies due to their competitive pricing and easiness to operate. In this paper, a post-processing technique to generate FMV data from standard video data format captured using a DJI Mavic 2 Enterprise drone system is developed and tested for intelligence, surveillance and reconnaissance (ISR) applications.

Keywords: *Drone full motion video (FMV); consumer drones; ArcGIS FMV*; *spatial video; intelligence, surveillance and reconnaissance (ISR).*

1. INTRODUCTION

Drone full motion video (FMV) is recognised as a proprietary technology that is often associated with military applications, where the capabilities to be integrated and analysed in a standard way with other spatial information, such as digital cartographic maps, remote sensing satellite images and other standard geographic information system (GIS) layers, make it a game changer in today's world of tactical information (Mott, 2011; Coffman, 2015; Stone, 2016; Patel & Butler 2020). In general, FMV technology is still seen as an exclusive technology because it is only available in military and high-end industrial drone systems such as Lockheed Martin Indago, Threod Titan and FLIR SkyRanger models, where the cost of the system together with sensor payload is more than USD 50,000 (Smith, 2019; Murtagh *et al.*, 2020).

FMV is a subset of motion imagery that is transmitted at television-like frame rates (24 to 60 Hz) (Coffman, 2015). According to the Motion Imagery Standards Board (MISB), motion imagery is defined as a sequence of images that is collected at a rate of one frame per second (1 Hz) or faster on the same field. MISB makes no formal distinction between motion imagery and FMV. However, MISB does specify that motion imagery must contain metadata associated with the collection. In order

to comply with MISB standard, a motion imagery system must in digital form and produce compliant MPEG-2 transport stream (TS). This does not apply to JPEG 2000 based systems or real-time transport protocol (RTP)/RTCP-based systems. The motion imagery system has to use H.262/MPEG-2, H.264/AVC, H.265/HEVC or JPEG 2000 compression technologies, and produce non-destructive metadata. It also needs to comply with the MISB ST 0902 minimum metadata set and add metadata elements as needed for the task, such as MISB ST 0601 and MISB ST 0801 (NATO Standardization Agency, 2009; Coffman, 2015).

Drones or optical sensors that have FMV capability are equipped with embedded STANAG 4609 metadata. STANAG 4609 is a NATO Standardization Agreement (STANAG) for motion imagery that provides common methods for exchange of motion imagery across systems among NATO nations. It also provides users a clear, consolidated and concise view of the standards they will need to build and operate motion imagery systems (NATO Standardization Agency, 2009). Figure 1 shows a system architecture for how the motion imagery / FMV is created and transmitted wirelessly to the remote client. The metadata (including sensor and other metadata) is collected, processed and then distributed by the aircraft flight computer through the most appropriate interface.

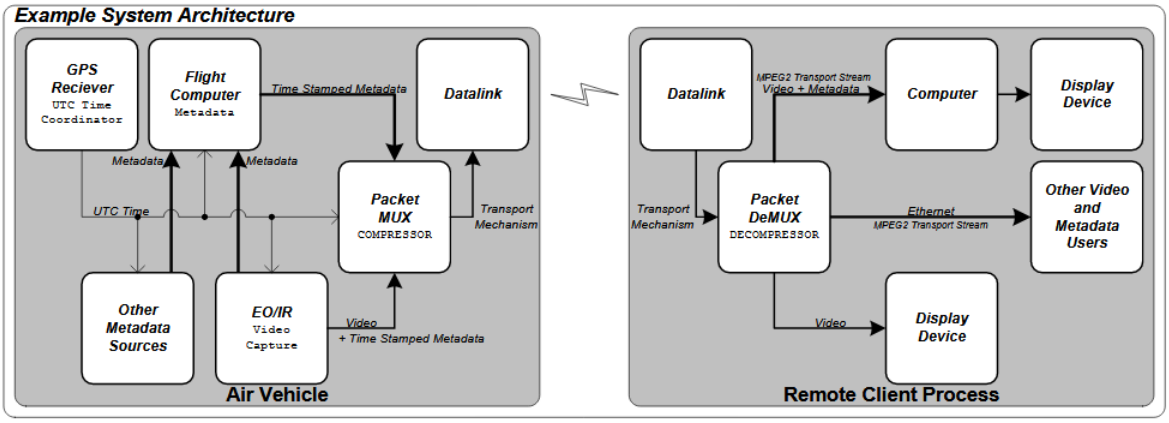

Figure 1: System architecture for FMV creation and transmission.
(Source: NATO Standardization Agency, 2009)

The aircraft flight computer inserts a timestamp, and then merges it with all metadata items and checksums into the unmanned aircraft system (UAS) datalink local data set (LDS) packet where the LDS is sent to the motion imagery encoder / packet multiplexer. The sent LDS packet is merged with the encoded video by the packet multiplexer to produce a unified data stream (MPEG2 TS, transport mechanism, etc.) for off-platform transmission. The remote client decodes and processes the motion imagery / FMV and metadata once received through the communication link (NATO Standardization Agency, 2009; Motion Imagery Standard Board, 2017).

In the past few years, the consumer drone industry has grown significantly due to the rising usage of drones for recreational and commercial purposes. The drone market size was estimated to have generated USD 22.5 billion in 2020 and is anticipated to grow at around 13.8% compound annual growth rate (CAGR) until 2025 (Schroth, 2020). Affordability, easiness to operate, and ability to produce high quality and accurate information in shortest time has motivated many companies to procure and deploy drones in nearly every industry, such as mapping, delivery and industrial inspection (Forni & Meulen, 2017). Among the top players in the consumer drone market at the moment are DJI, Parrot and Yuneec (Global Brands, 2020; UAV Coach, 2020). However, DJI is the most used consumer drone brand worldwide nowadays (Snow, 2019), where around 70% of drone market share in US is held by DJI (Schroth, 2019; Schmidt & Vance, 2020).

Lately, GIS commercial software companies and also open-source communities have embarked on research activities to produce GIS tools for FMV data processing and analysis. As a result, standard digital video formats captured using consumer drones are able to be processed / generated into FMV format. The emergence of this trend is seen as a shift to GIS and remote sensing data analytical capabilities in the near future, where it has potential to produce more realistic, dynamic and versatile analysis outputs. This development is predicted to give advantages to the remote sensing and GIS community as a whole.

Therefore, in this paper, a post-processing technique to generate FMV data from standard video data format captured using a DJI Mavic 2 Enterprise drone system is developed and tested for intelligence, surveillance and reconnaissance (ISR) applications. The rest of the paper is organised as follows: Section 2 provides a brief overview of ISR, followed by Section 3, where the consumer drone video data post-processing technique is developed, which is tested for ISR applications in Section 4. Finally, Section 5 will conclude about this study and highlight the directions for future research.

2. INTELLIGENCE, SURVEILLANCE AND RECONNAISSANCE (ISR)

ISR terminology is commonly associated with military activity. According to the U.S. Department of Defense (DOD), ISR is an integrated operations and intelligence activity that synchronises and integrates the planning and operation of sensors, assets, processing, exploitation, and dissemination systems in direct support of current and future operations (Hoehn & Smagh, 2020; Office of the Chairman of the Joint Chiefs of Staff, 2020).

Geospatial intelligence (GEOINT) is one of the intelligence collections disciplines under ISR (Figure 2). It consists of imagery, imagery intelligence (IMINT) and geospatial information. GEOINT exploitation includes analysis of electro-optical, infrared, and radar imagery; FMV; moving target indicators; geospatial information; and spectral, laser infrared, radiometric, polarimetric, spatial, and temporal data (DOD, 2017).

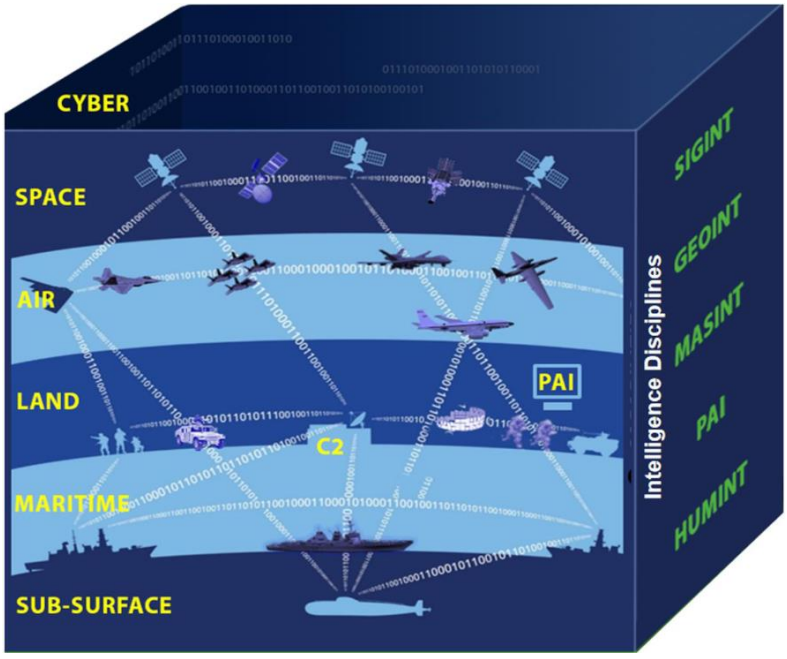

Figure 2: Intelligence collection disciplines and array of multi-domain ISR capabilities. (Source: Hoehn & Smagh, 2020)

Video based data sources such as FMV are able to provide the most recent view of a situation, and also work as auxiliary data to satellite imagery and aerial photos that able provide richer and precise information in regards to the area of interest (AOI) (Mott, 2011). The FMV data is overlayed on the geospatial layers and annotations to obtain more effective intelligence information. Furthermore, object identification on the ground can be performed using FMV data, which is very useful to military analysts (Mott, 2011; Beall, 2017; Fry, 2018; Patel & Butler, 2020).

In civilian applications, the same concept of ISR has been applied for safety and security aspects such as disaster relief, fire-fighting operations, border control and maritime surveillance (Mott, 2011; Masback, 2014; Nicholas *et al.*, 2019). The usage of GEOINT technologies such as drone FMV data in disaster mitigation and relief is able to provide quick and precise information to the relevant authorities during or after the event, in accordance to the type of analysis and information required (Geospatial World, 2013; Coffman, 2015; Lilian, 2017).

3. POST-PROCESSING TECHNIQUE: GENERATING CONSUMER DRONE FMV DATA

In this study, we used ArcGIS FMV software to develop the video post-processing technique. ArcGIS FMV (also known as ArcGIS FMV add-in) is an add-in software developed by Esri. ArcGIS FMV is able to view and analyse FMV data in a standard way together with other geospatial and GIS data. Besides that, ArcGIS FMV has the capability to store and manage FMV files. In order to find and retrieve the archived FMV files, the user simply needs to draw a polygon on the AOI in the ArcGIS basemap before executing the query function. Others functions that can be performed using ArcGIS FMV are video zoom in / zoom out, distance measurement, coordinate point extraction, point of interest (POI) marking and labelling, video mosaicking, metadata extraction, video-metadata multiplexing, and generating reports in PowerPoint format (ESRI, 2018; ESRI, 2019).

The ArcGIS FMV multiplexer geoprocessing tool has similar workflow as the multiplexer / encoder described in Figure 1. The function of the ArcGIS FMV multiplexer geoprocessing tool is to merge the non-MISB compliant video with the associated video metadata file in order to generate a new MISB compliant video file (FMV data) (ESRI, 2019). Another advantage of ArcGIS FMV is the generated FMV data is able to be read and analysed in other FMV software environments.

Overall, the post-processing technique workflow is described in Figure 3. Prior to the FMV data generation process, the 13-columns video metadata file as described in Table 2 must be created in advance. Generally, the video metadata file is created based on parameters that are available in the drone flight log file. Some parameters are taken directly from the drone flight log file while the rest are produced through calculation or determination of a certain constant value according to the type of air platform being used.

The final equation of the sensor horizontal field of view (FOV_H) in Table 2 is originally derived from Equation 1 (ESRI, 2019), where it is further developed and consolidated with other technical information, such DJI video aspect ratio (16:9), diagonal FOV (FOV_D) of the sensor, and focal length of the sensor, where H_{length} is the sensor horizontal length, V_{length} is the sensor vertical length, f is the focal length of the sensor and D_{length} is the sensor diagonal length.

$$FOV_H = 2 \times \arctan\left(\frac{H_{length}}{2f}\right) \quad (1)$$

where:

$$D_{length} = \sqrt{H_{length}^2 + V_{length}^2}$$

$$= \sqrt{{H_{length}}^2 + (\frac{9}{16} H_{length})^2}$$

$$= \sqrt{{H_{length}}^2 + \frac{81}{256} {H_{length}}^2}$$

$$= \frac{H_{length}}{16} \sqrt{337}$$

Thus:

$$H_{length} = \frac{D_{length} \times 16}{\sqrt{337}} \quad (2)$$

where:

$$D_{length} = 2(tan\left(\frac{\text{FOV}_D}{2}\right) \times f) \quad (3)$$

Hence, Equations 2 and 3 are inserted into Equation 1 in order to get the final equation of FOV_H (Equation 4), which is used in Table 2.

$$\text{FOV}_H = 2 \times \arctan\left(\frac{16(2(\tan(\text{FOV}_D/2) \times f))/\sqrt{337}}{2f}\right) \quad (4)$$

Meanwhile, the final equation of the sensor vertical FOV (FOV_V) in Table 2 is originally derived from Equation 5 (ESRI, 2019) where it is further developed and consolidated, with other technical information, such DJI video aspect ratio (16:9), FOV_D of the sensor and focal length of the sensor (*f*).

$$\text{FOV}_V = 2 \times \arctan\left(\frac{V_{length}}{2f}\right) \quad (5)$$

where:

$$D_{length} = \sqrt{{H_{length}}^2 + {V_{length}}^2}$$

$$= \sqrt{(\frac{16}{9} V_{length})^2 + {V_{length}}^2}$$

$$= \sqrt{\frac{256}{81} {V_{length}}^2 + {V_{length}}^2}$$

$$= \frac{V_{length}}{9} \sqrt{337}$$

Thus:

$$V_{length} = \frac{D_{length} \times 9}{\sqrt{337}} \quad (6)$$

Hence, Equations 3 and 6 are inserted in Equation 5 in order to get the final equation of FOV_V (Equation 7), which is used in Table 2.

$$\text{FOV}_V = 2 \times \arctan\left(\frac{9(2(\tan(\text{FOV}_D/2) \times f))/\sqrt{337}}{2f}\right) \quad (7)$$

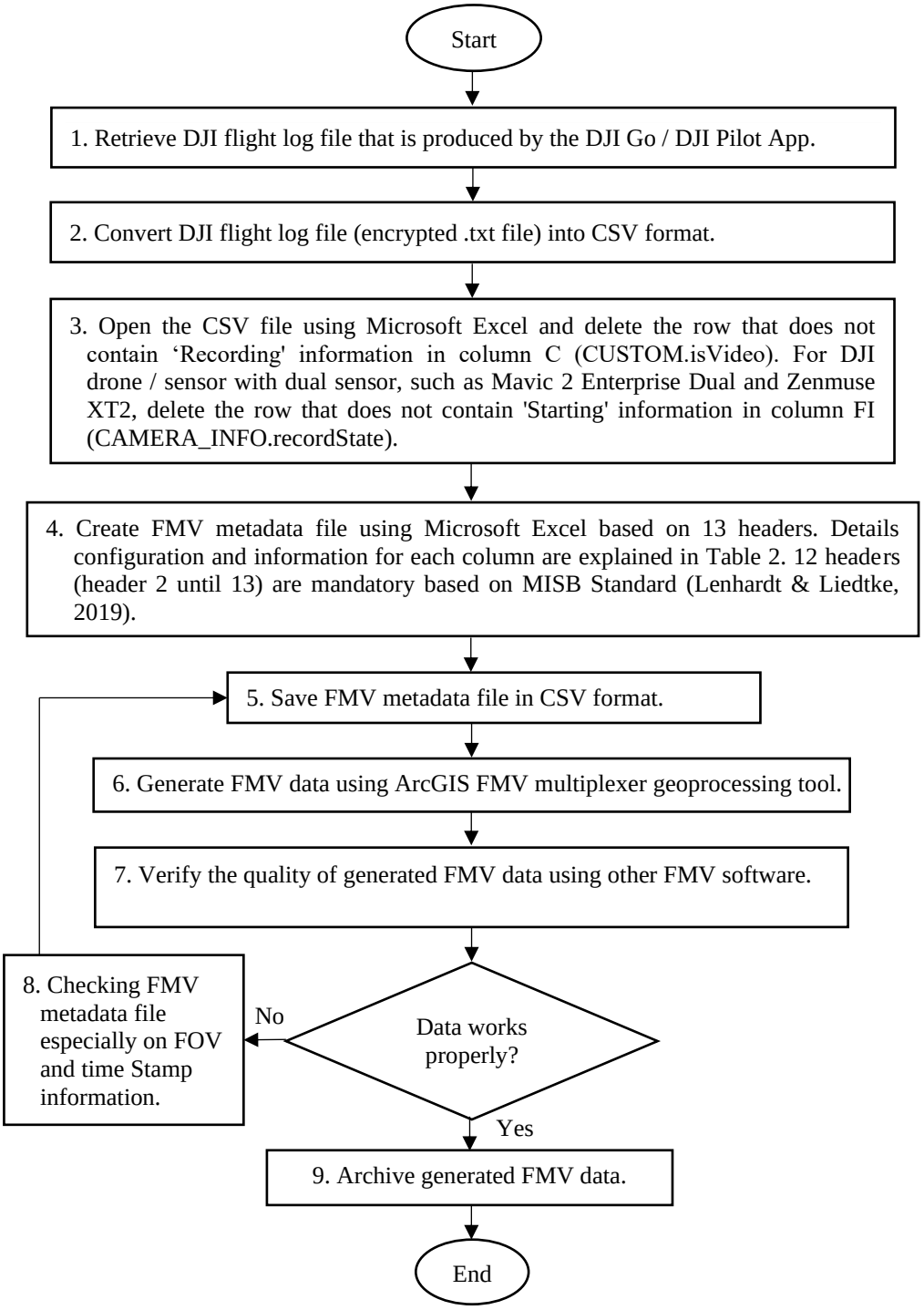

Figure 3: Methodology to generate FMV data using ArcGIS FMV multiplexer geoprocessing tool.

Table 2: Architecture of FMV metadata file.

Column	Header Title	Source of Data / Calculation / Constant Value
1	Date and Time	Extracted from DJI flight log file.
2	Sensor Latitude	
3	Sensor Longitude	
4	Platform Heading Angle	
5	Sensor Relative Elevation Angle	
6	Unix Time Stamp	Converting data in column 1 (Date and Time) into Unix timestamp format using this formula in Microsoft Excel: ([Column 1]-DATE(1970,1,1))*86400000000. The result must be in integer (Lenhardt & Liedtke, 2019).
7	Sensor True Altitude	Calculate: [MSL value from DJI flight log file] – [DEM value]. Refer to AcrGIS FMV user manual (ESRI, 2019) for DEM value extraction process.
8	Sensor Horizontal Field of View	Calculate: $2\times\arctan[(16(2(\tan(FOV_D/2)\times f))/\sqrt{337})/2f]$ (Equation 5) where's the actual value of FOV_D and f is depends on type of drone model. The result must be in degrees.
9	Sensor Vertical Field of View	Calculate: $2\times\arctan[(9(2(\tan(FOV_D/2)\times f))/\sqrt{337})/2f]$ (Equation 7) where's the actual value of FOV_D and f is depends on type of drone model. The result must be in degrees.
10	Platform Pitch Angle	Set to zero value because the aircraft movement has been compensated by the sensor gimbal system.
11	Platform Roll Angle	
12	Sensor Relative Azimuth Angle	Set to zero value because the sensor is fixed on a multirotor platform, which is zero degrees (0º) forward along the platform longitudinal axis. However for DJI Zenmuse payload series, the sensor relative azimuth angle values are obtained by calculate using the formula: $G_{yaw} - P_{yaw}$ Where, G_{yaw} = GIMBAL.yaw value (column BT in DJI flight log file) P_{yaw} = OSD.yaw value (column V in DJI flight log file)
13	Sensor Relative Roll Angle	Set to zero value because the top and bottom edges of the captured data lie perpendicular to the plane created by the sensor relative depression angle axis.

4. GENERATED FMV DATA FOR ISR APPLICATIONS

The generated FMV data are tested and analysed using open-source (QGIS FMV) and commercial (TacitView) FMV software. The position and orientation of the drone, video footprint and spatial metadata information are clearly displayed in the both software interfaces (Figure 4). The comparison of video data information before and after undergoing the multiplexer process are shown in Figure 5. It shows that the geospatial and coordinate information are already embedded into the generated FMV data.

By using TacitView's analysis tools, we able to recognise the characteristics (Figure 6) and track the movement behaviour (Figure 7) of the target. The FMV data are overlaid on raster imagery and elevation data in order to enhanced the capability of intelligence collection process. Therefore, the generated FMV data is able to provide information of the actual situations and activities that occurred on the targeted location, where this kind of intelligence information cannot be obtained from the raster imagery alone.

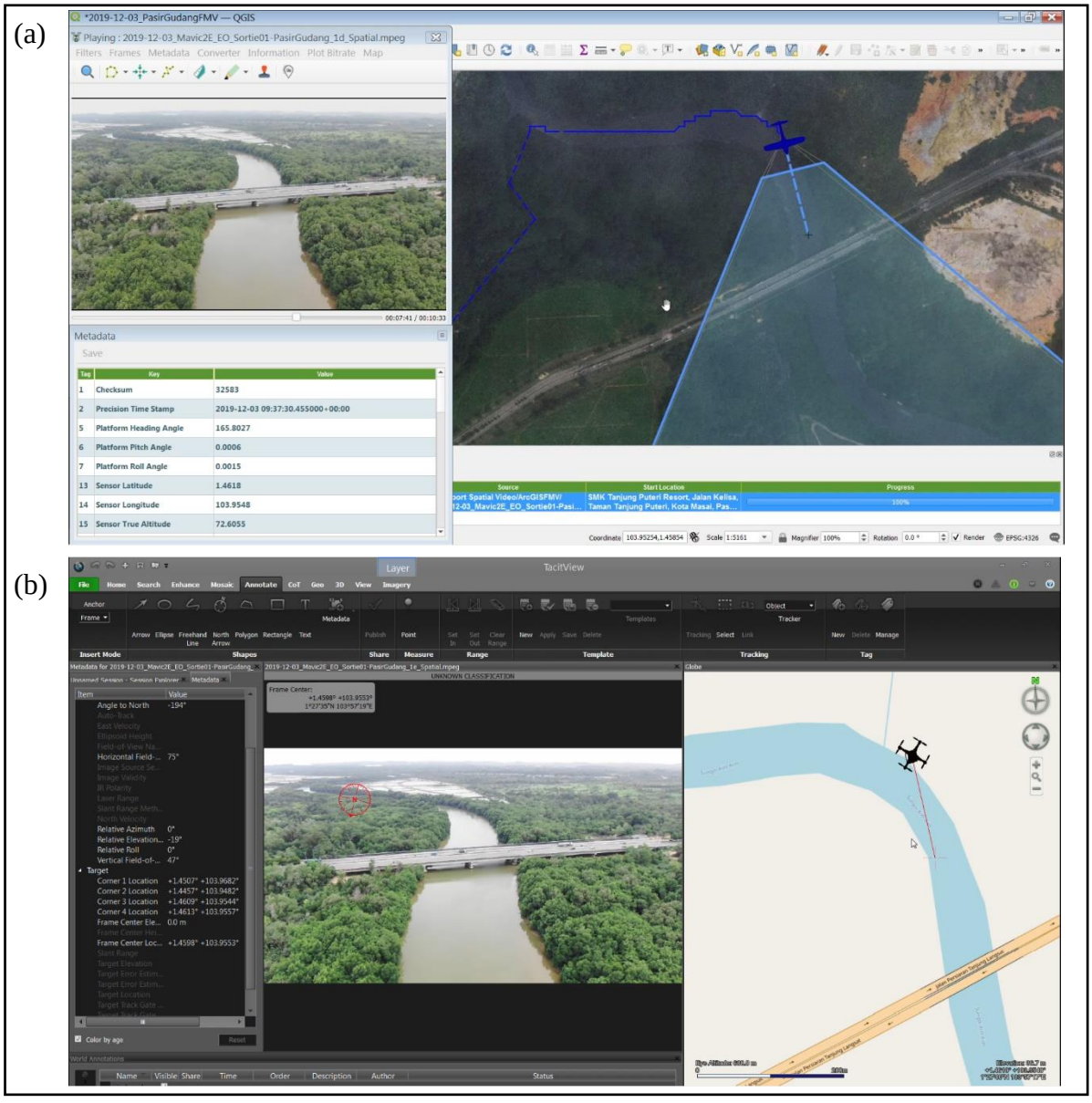

Figure 4: The generated FMV data displayed in (a) QGIS FMV and (b) TacitView.

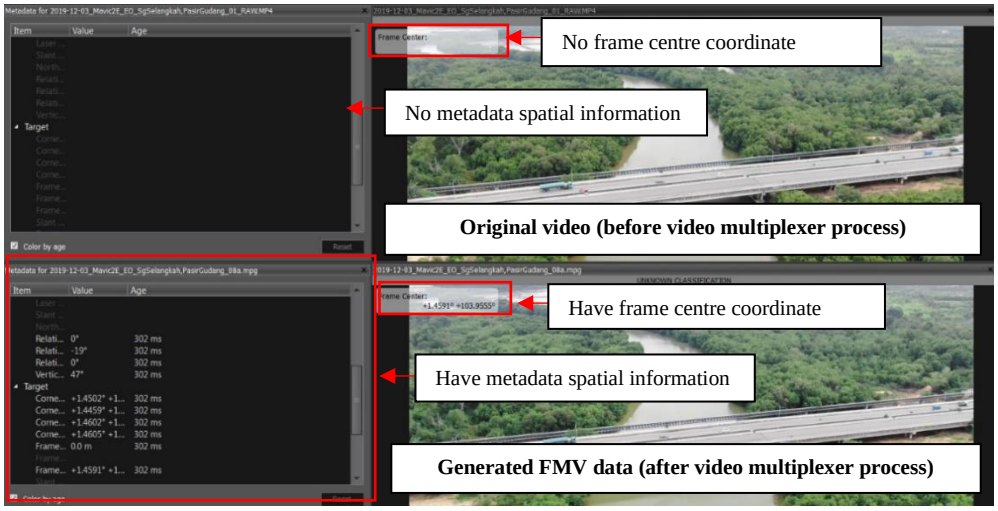

Figure 5: Comparison between (top) the original video before the multiplexer process and (bottom) generated FMV data after the multiplexer process in TacitView.

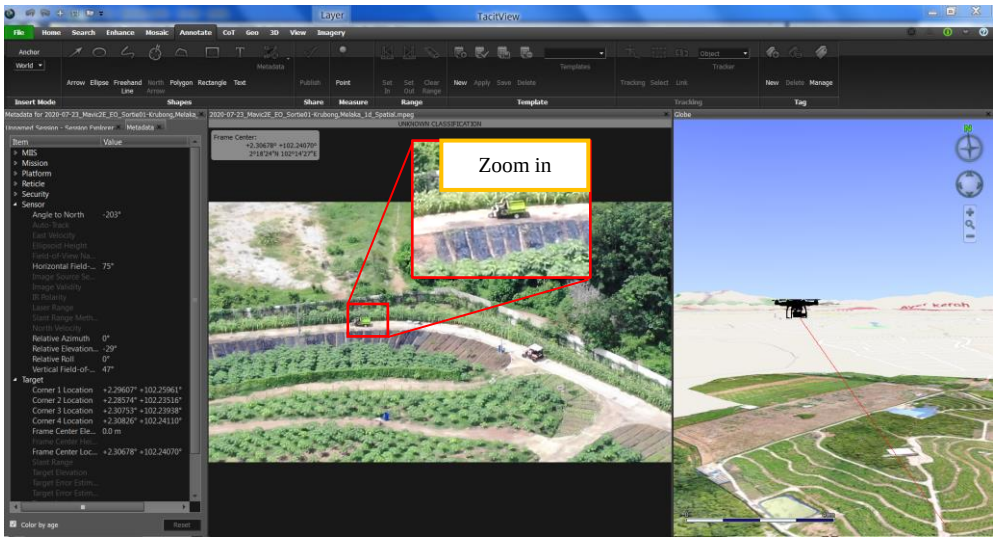

Figure 6: Location and characteristics of the moving target clearly identified.

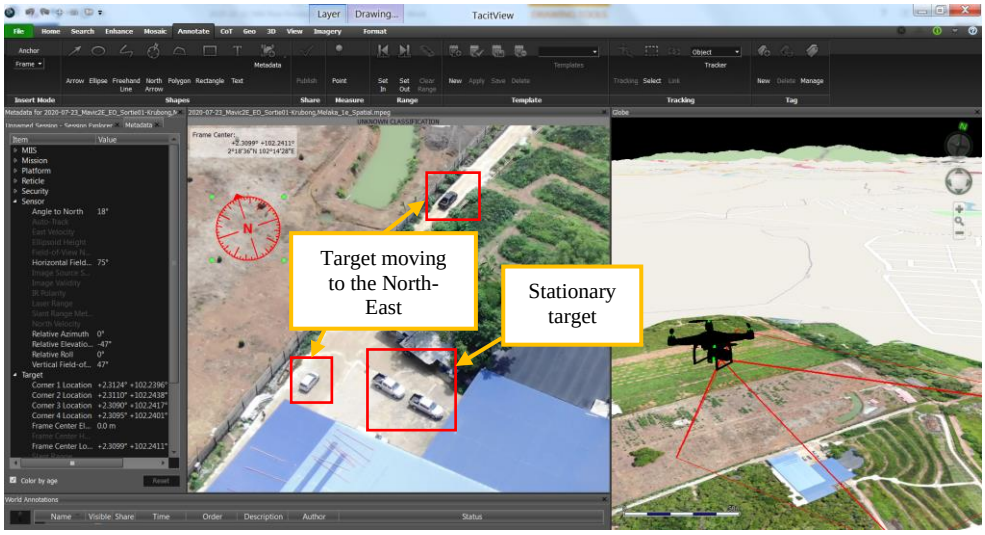

Figure 7: Direction and movement behaviour of the target.

However, measurement on the true or generated FMV data is somewhat less accurate (Lee, 2013). In order to achieve precise results, the FMV data must be analysed together with other geospatial information, such as digital cartographic maps, geo-corrected raster images (satellite / airborne) and elevation / survey data. This is because the accuracy of FMV data solely depends on the accuracy and precision of the aircraft / drone navigation system (latitude, longitude, altitude & etc.) (Taylor & Settergren, 2012; Coffman, 2015; ESRI, 2018; Patel & Butler, 2020) and also the orientation information of the sensor / camera (Inside Unmanned Systems, 2020; Patel & Butler, 2020).

Figure 8 it shows the generated FMV data used for post-event analysis over a homogeneous type of land cover along a river. Through the capability of FMV data, the exact location of the target can be easily identified and extracted. This kind of analytical method is very useful for dynamic temporal intelligence analysis.

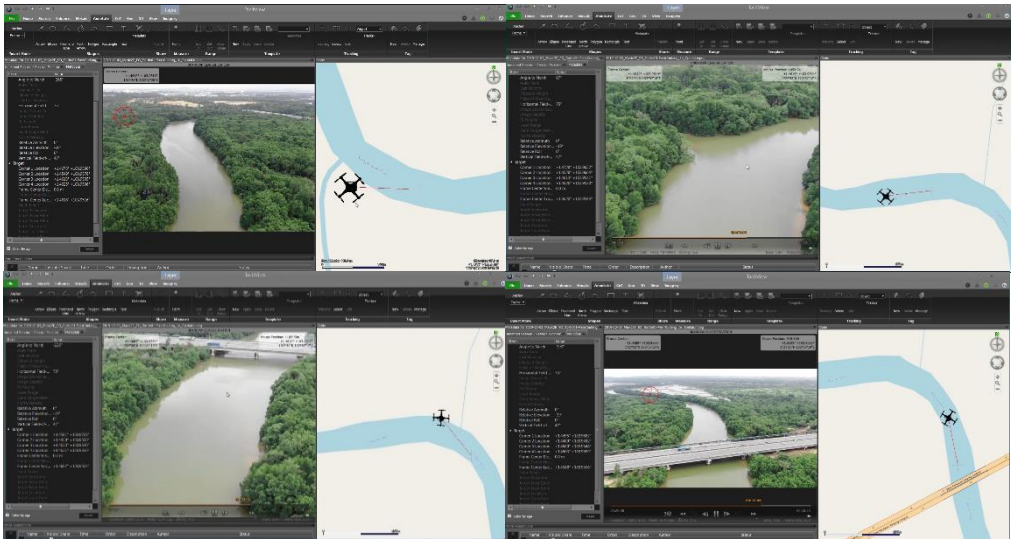

Figure 8: Generated FMV data used in post-event analysis for river and surrounding area monitoring activities.

5. CONCLUSION

This study has shown that the FMV data from DJI drones can be generated using the proposed methodology. The generated FMV data can be used for ISR applications by analysing the FMV data together with other GEOINT data source to obtain richer and precise information in regards to the area of interest. The FMV data adds a fourth dimension to imagery analysis, where the video footprint can be viewed directly on top of maps to provide excellent event fidelity, seamless event progression and full context regarding the nature of the location and activities being viewed on the Earth surface. Furthermore, the generated FMV data using the proposed methodology are compatible with other FMV software.

It should be noted that in this study, the accuracy of FMV data solely depends on the accuracy and precision of the aircraft / drone navigation system. Thus, more studies need to be carried up in the future on improving the accuracy of the generated FMV data.

ACKNOWLEDGMENT

The authors acknowledge the support provided by the Malaysian Ministry of Science, Technology and Innovation (MOSTI), Malaysian Space Agency (MYSA) and Malaysian Armed Forces (MAF).

REFERENCES

Beall, B. (2017). *AMC Names 2017 Innovation Award Winners*. Available online at: http://apgnews.com/community-news/amc-names-2017-innovation-award-winners (Last access date: 8 January 2021).

Coffman, P.N. (2015). *Capabilities Assessment and Employment Recommendations for Full Motion Video Optical Navigation Exploitation (FMV-ONE).* Master Thesis, Information Sciences Department, Naval Postgraduate School, California.

Department of Defense (DOD) (2017). *Joint and National Intelligence Support to Military Operations (JP 2-01)*. Joint Chiefs of Staff, Washington DC.

ESRI (2018). *Full Motion Video Add-In for ArcGIS 10.x: Frequently Asked Questions*. Available online at: https://www.esri.com/content/dam/esrisites/en-us/arcgis/capabilities/full-motion-video/FMV_FAQ%20(2).pdf (Last access date: 13 May 2020).

ESRI (2019). *Using the ArcGIS Full Motion Video Add-In Version 1.4*. Available online at: https://www.esri.com/content/dam/esrisites/en-us/media/pdf/Full_Motion_Video_1.4_User_Manual.pdf (Last access date: 13 May 2020).

Forni, A.A. & Meulen, R.V.D. (2017). *Gartner Says Almost 3 Million Personal and Commercial Drones Will Be Shipped in 2017*. Available online at: https://www.gartner.com/en/newsroom/press-releases/2017-02-09-gartner-says-almost-3-million-personal-and-commercial-drones-will-be-shipped-in-2017 (Last access date: 1 June 2020).

Fry, J. (2018). ArcGIS Full Motion Video. *2018 Esri Federal GIS Conference Proceedings*. 20-21 March 2018, Washington Convention Center, Washington DC.

Geospatial World (2013). *UAS in Disaster Management: Real-Time Videos for Emergency Relief*. Available online at: https://www.geospatialworld.net/article/uas-in-disaster-management-real-time-videos-for-emergency-relief (Last access date: 17 September 2020).

Global Brands (2020). *Top 10 Drone Companies in the world – 2020*. Available online at: https://www.globalbrandsmagazine.com/top-10-drone-companies-in-the-world-2020/ (Last access date: 1 June 2020).

Hoehn, J.R., & Smagh, N.S. (2020). *Intelligence, Surveillance, and Reconnaissance Design for Great Power Competition*. Congressional Research Service (CRS), Washington, D.C.

Inside Unmanned Systems (2020). *Getting It Right for Gimballed ISR*. Available online at: https://insideunmannedsystems.com/getting-it-right-for-gimballed-isr (Last access date: 17 September 2020).

Lee, M.G., (2013). Geospatial Intelligence (GEOINT) and Intelligence Surveillance and Reconnaissance (ISR) Convergence, *Proc. SPIE*, 8740: 9-16.

Lenhardt, J. & Liedtke J. (2019). *Video Multiplexer Tips and Tricks*. Available online at: https://www.esri.com/arcgis-blog/products/arcgis-pro/imagery/video-multiplexer-tips-tricks/ (Last access date: 13 May 2020).

Lilian, B. (2017). *Aeryon SkyRanger Drones Help First Responders in Caribbean After Irma*. Available online at: https://unmanned-aerial.com/aeryon-skyranger-drones-help-first-responders-caribbean-irma (Last access date: 17 September 2020).

Masback, K.J. (2014). *GEOINT and Public Safety*. Available online at: https://trajectorymagazine.com/geoint-and-public-safety/(Last access date: 17 September 2020).

Motion Imagery Standard Board (2017). *Standard UAS Datalink Local Set MISB ST 0601.11*. National Geospatial-Intelligence Agency (NGA), Springfield, Virginia.

Mott, R. (2011). *Motion Video Exploitation*. Available online at: https://eijournal.com/print/articles/motion-video-exploitation (Last access date: 13 May 2020).

Murtagh, C., Amir, O., Bronnenberg, C., Casparro, C. & Linn, B. (2020). *First Responder Robotic Operations System Test (FRROST): Small Unmanned Aircraft Systems for Search and Rescue*. Assessment Report, National Urban Security Technology Laboratory, Science and Technology Directorate, U.S. Department of Homeland Security, New York.

NATO Standardization Agency (2009). *Standardization Agreement (STANAG), 4609 JAIS (EDITION 3) - NATO Digital Motion Imagery Standard. North Atlantic Treaty Organization (NATO)*. NATO Standardization Agency, Brussels, Belgium.

Nichols, R.K., Mumm, H.C., Lonstein, W.D., Ryan, J., J.C.H., Carter, C. and Hood, J.P. (2019). Chapter 10: UAS Intelligence, Surveillance and Reconnaissance (ISR). *In* Nichols, R.K. (Ed.), *Unmanned Aircraft Systems in the Cyber Domain*. New Prairie Press, Manhattan, pp. 210-229.

Office of the Chairman of the Joint Chiefs of Staff (2020). *DOD Dictionary of Military and Associated Term*s. Joint Chiefs of Staff, Washington DC..

Patel, M. & Butler, D. (2020). *Adding Context to Full-Motion Video for Improved Surveillance and Situational Awareness*. Available online at: https://www.aerodefensetech.com/component/content/article/adt/features/articles/36055 (Last access date: 8 January 2021).

Schmidt, B. & Vance, A. (2020). *DJI Won the Drone Wars, and Now It's Paying the Price*. Available online at: https://www.bloomberg.com/news/features/2020-03-26/dji-s-drone-supremacy-comes-at-a-price (Last access date: 1 June 2020).

Schroth, L. (2019). *Drone Manufacturer Market Shares: DJI Leads the Way in the US*. Available online at: https://www.droneii.com/drone-manufacturer-market-shares-dji-leads-the-way-in-the-us (Last access date: 1 June 2020).

Schroth, L. (2020). *The Drone Market Size 2020-2025: 5 Key Takeaways*. Available online at: https://droneii.com/the-drone-market-size-2020-2025-5-key-takeaways (Last access date: 7 January 2021).

Smith, C. (2019). *'It's one of the best of its class': Drone donated to Fredericton Police Force*. Available online at: https://globalnews.ca/news/5078119/drone-donated-fredericton-police (Last access date: 7 January 2021).

Snow, C. (2019). *Seven Trends That Will Shape the Commercial Drone Industry In 2019*. Available online at: https://www.forbes.com/sites/colinsnow/2019/01/07/seven-trends-that-will-shape-the-commercial-drone-industry-in-2019/ (Last access date: 1 June 2020).

Stone, A. (2016). *How full-motion video is changing ISR*. Available online at: https://www.c4isrnet.com/intel-geoint/isr/2016/03/23/how-full-motion-video-is-changing-isr (Last access date: 7 January 2021).

Taylor, C.R. & Settergren, R.J. (2012). Full-Motion Video Georegistration for Accuracy Improvement, Accuracy Assessment, and Robustness. *Proc. SPIE,* 8386: 43-51.

UAV Coach (2020). *The Top 100 Drone Companies to Watch in 2020*. Available online at: https://uavcoach.com/drone-companies (Last access date: 1 June 2020).

ASSESSMENT AND MITIGATION OF MONSOON FLOODS VIA SATELLITE IMAGERY DATA EXTRACTION AND DRONE FULL MOTION VIDEO (FMV)

Muhammad Akmal Asraf Mohamad Sharom*, Mohd Fazuwan Ahmad Fauzi, Mohamad Zulkhaibri Mat Azmi, Syariman Samsudin, Mohd Hakimi Abdul Rahman, Mohammad Azizi Fadzil & Sabrina Shahri

Malaysian Space Agency (MYSA), Ministry of Science, Technology and Innovation (MOSTI), Malaysia

*Email: asraf@mysa.gov.my

ABSTRACT

According to the Disaster Year in Review 2019 by the Centre for Research on the Epidemiology of Disasters (CRED), there were 194 reported occurrences on floods that had affected nearly 31 million people, which caused approximately 5,000 deaths in 2019. In Malaysia, monsoon floods are the most devastating natural disaster that occurs between November to March for the Northeast Monsoon and May to September for the Southwest Monsoon. Malaysia experiences serious flooding, which has a negative impact on several states especially on the economy and to society in general. Floods are natural incidents that cannot be avoided but its impact can be minimised by implementing flood mitigation plans. Actual flood extent and distribution of affected areas are difficult to be estimated and determined using conventional flood monitoring methods such as using manned aircrafts, which is not cost effective and too risky. However, this can be solved using remote sensing technology. By obtaining information through satellite images and drone full motion video (FMV), the cause of the aggravated flood situation can be identified. Through the application of radar satellite imagery and land use information, we are able to extract water bodies and identify the actual flood extent. The generated flood extent information is then overlaid on optical satellite images to identify hotspot areas such as the possible causes of flood situations. In order to acquire more details / real time information on the flood hotspot areas, a quadrotor drone with FMV sensor is used. The captured FMV data is analysed using TacitView for real time and post-event analysis. The combination of remote sensing satellite imagery and drone FMV data through geographical information systems (GIS) analysis can produce critical and useful information for authorities to draw up more effective and efficient flood mitigation plans.

Keywords: *Flood assessment and mitigation; drone full Motion Video (FMV); remote sensing satellite imagery*; *hotspot locations*; *real-time field assessment.*

1. INTRODUCTION

According to the Disaster Year in Review 2019 by the Centre for Research on the Epidemiology of Disasters (CRED), at least 396 natural disasters were reported, that killed 11,755 people, affected 95 million people, and cost nearly USD 130 billion. Based the statistics provided in the review, 49% of the disaster events were floods (194 reported), which contributed to 33% of total number of people that had been affected by natural disasters (nearly 31 million people) and killing approximately 5,000 people (43% of total number of deaths caused by natural disasters) in 2019 (Froment & Below, 2020).

Floods are the most common natural disaster in Malaysia due to heavy rainfall during the monsoon and inter-monsoon periods. Annual monsoon floods normally occur in the states of east coast during the northeast monsoon period from November to March and southwest monsoon period from May to September (Alias *et al.*, 2016; NADMA, 2019). In general, several states in Malaysia have

experienced negative impacts from serious flooding especially on the economy and society. According to the statistics shown in Figure 1, the number of people affected by northeast monsoon floods from 2015 to 2019 is 207,605 (NADMA, 2019).

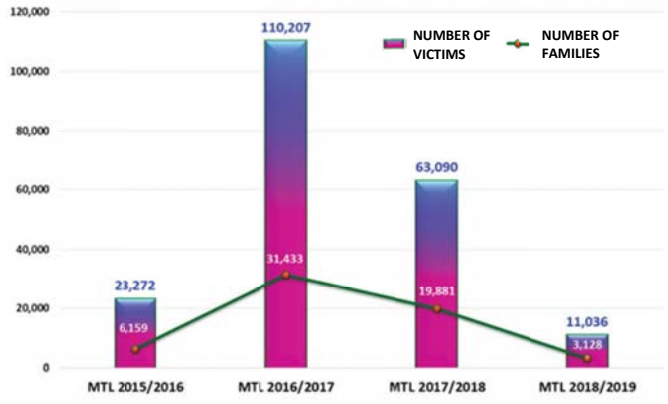

Figure 1: Analysis of flood trends events during the northeast monsoon (MLT) in 2015-2019 (Source: NADMA, 2019)

Floods are natural incidents that cannot be avoided but its impact can be minimised by implementing flood mitigation plans (Sani *et al.*, 2014; Hua, 2015). Therefore, related data for flood disaster management, such as inundated areas as well as locations of access roads and evacuation centres from various sources must be centralised and integrated for easy access by the relevant agencies for fast decision making. In this respect, remote sensing and its related technologies can play an important role in disaster management by providing the required information to various levels of the authorities. In Malaysia, the National Disaster Management Agency (NADMA) is the government agency that is responsible for coordinating the management of national disasters in Malaysia and ensuring that all national disaster management policies and mechanisms are adhered to and implemented at all levels of disaster management. Related government agencies and departments, such as Department of Irrigation and Drainage (JPS), Malaysian Public Works Department (JKR) and Malaysian Space Agency (MYSA), are the departments that assist NADMA in providing strategic information and technical support for natural disaster management in Malaysia.

In this paper, the methodology to extract and map actual flood extent using remote sensing and others related technologies are developed. The extracted flood information is then utilised to identify hotspot locations before real-time field assessment and verification activities are carried out using a drone FMV system. The rest of the paper is organised as follows: Section 2 provides a brief overview regarding drone technology implementation in natural disaster events. In Section 3, the methodology to map actual flood extent using remote sensing is explained, followed by application of drone full motion video (FMV) for real-time flood assessment and verification in Section 4. Finally, Section 5 will conclude about this study and highlight the directions for future research.

2. DRONE TECHNOLOGY IMPLEMENTATION IN NATURAL DISASTER EVENTS

In emergencies situations, decisions should be made within a short period of time. The effectiveness of the decisions largely depends on situational awareness formed by the integration of various reliable sources. United Nations (UN) entities encompass many different space-based technologies and unmanned aerial vehicles (UAVs) / drone technologies as reliable sources during emergencies, such as in disaster management (ESCAP, 2014).

Drones come with various advantages, including (Giordan *et al.*, 2017; Mashfiq, 2017):

i. Ability to fly at low altitudes irrespective of cloud / weather conditions;
ii. Ability to capture high resolution images;
iii. Capability to be equipped with various types of sensors (cameras, laser scanners, navigation / inertial sensors, etc.);
iv. Possibility to acquire imagery with different angles;
v. Cheaper operation cost; and
vi. Flexibility of carrying out small, medium and large-scale monitoring operations.

There are three types of drones, which are fixed wing, rotary wing and hybrid platforms, which the latest concept. While each type has its own advantages and disadvantages, these platforms are suited for being used in emergencies situations. Fixed wing systems are suitable for mapping disaster areas (up to 10 km^2) that need to be covered with high spatial detail but it requires a runway or launcher for take-off and / or landing, which may be limited during natural disaster situations. Rotary wing systems are most applicable for search and rescue operations as well as inspection tasks, as it is able to hover, and take-off and land vertically (Rester *et al*., 2013). Meanwhile for hybrid systems, the combination of fixed wing and rotors allow the system to vertically take-off and land like rotary wing drones, as well horizontal flight like fixed wing drones. This gives it advantages to cover large mapping areas and carry heavier cargo than multi-rotor drones. However, it has disadvantages such as not being as navigable as rotary wing drones, and not having the long range of fixed wing drones. It is also generally more expensive as compared to fixed wing and rotary wing (Samsioe *et al.*, 2017).

Drones are used as complementary to satellite imagery for mapping and monitoring disaster-affected areas by capturing high-resolution aerial images. It also used to stream and transmit live-view video directly to the ground for disaster monitoring, damage assessment, as well as response and recovery operations. Drones are also used for verification or physical field surveys after receiving preliminary assessment of the disaster incident (Geospatial World, 2013; Sun *et al.*, 2016; Lilian, 2017).

During emergencies situations such as rapid response or disaster assessment, the data accuracy direct from observations by drones equipped with Global Navigations Satellites Systems (GNSS) and inertial navigation system (INS) can be enough for fast-response to time-critical events (Remondino *et al.*, 2011; Nex & Remondino, 2014; Sun *et al.*, 2016; Zhou, 2009). Table 1 shows the comparison of drone mapping during emergency and normal situation.

Table 1: Comparison between normal mapping and emergency mapping (Mashfiq, 2017).

No.	Items	Normal Mapping	Emergency Mapping
1	Planning scope	Proper flight plan to capture the required information	None, ad-hoc
2	Production time	Possibility to process the results, come up with results in days	Real-time within hours if not real-time
3	Required location accuracy	High	Low (acceptable)
4	Possibility of complementary mission	Yes	No
5	Bandwidth constraints	Offline upload acceptable	Online preferable
6	Availability of damage assessment experts in the field	Often available	Scarce
7	Focus	Whole regions	Damage zones

Commercial drone technologies have advanced over the years and are now equipped with the capability to capture FMV data, which is a narrow subset of motion imagery that includes geospatial metadata, commercial image formats and playback rates. Motion imagery technically begins at frame rates of 1 Hz (1 frame per second) or higher within a same field. The temporal rates in frames per second must be sufficient to characterise the wanted dynamic situation (NATO Standardization Agency, 2009). This provides the capability to understand the actual activity and most recent view of a situation in regards to the area of interest (AOI) (Mott, 2011).

In order to standardise motion imagery standards, the Motion Imagery Standards Board (MISB) was established under the Department of Defense (DOD) Directive 5105.60 to formulate, review and recommend standards for motion imagery, associated metadata, audio and other related systems for the DOD, Intelligence Community (IC) and National System for Geospatial-Intelligence (NSG). According to MISB, there is no formal distinction between FMV and motion imagery terms, but the board does specify that motion imagery must contain metadata associated with the collection. In order to be compliant to the MISB standard, a motion imagery system must be in digital form and be compliant with MPEG-2 transport stream (TS). This does not apply to JPEG 2000 based systems or real-time transport protocol (RTP) / real-time transport control protocol (RTCP)-based systems. The motion imagery system also needs to use H.262/MPEG-2, H.264/AVC, H.265/HEVC or JPEG 2000 compression technology, and produce non-destructive metadata. In addition, it should comply with the MISB ST 0902 minimum metadata set and add metadata elements as needed for the task, such as MISB ST 0601 and MISB ST 0801 (NATO Standardization Agency, 2009; Coffman, 2015).

FMV data can be analysed using FMV analysis software that is available in the market, such as MotionDSP, TacitView, ArcGIS FMV and QGIS FMV. By using FMV analysis software, users can share their annotations and tagging of objects or events that are found in the video feeds in a standard way. It allows users to search for a specific event, and tagged person or vehicle that is archived and catalogued in the server system. The software also allows users to fuse or overlay satellite images, geospatial and elevation data, as well as multi-source intelligence data with video feeds to conduct in-depth analysis, and also to provide richer and more useful intelligence products. In addition, it has the capability to enhance images or videos that are viewed by users. This is because sometimes the video feeds transmitted by drones can suffer from a number of deficiencies deriving from the shakiness of the platform, standard resolution of its sensor, and dust and haze that are often present. Users can use the FMV analysis software to compare archived videos with real-time videos to conduct change detection analysis (Mott, 2011).

There are two primary methods to exploit FMV in order to extract geolocation coordinates, which are still imagery extraction and call out method. For the still imagery extraction method, the video footage and platform metadata are manipulated through post-processing mechanisms on a geospatial workstation. As for the call out method, the sensor operator physically moves the crosshairs in real time, at which point the coordinates may be read off the FMV display location of the requested objects. This method is faster than the still imagery manipulation, but it is also subject to inherent errors of the drone's GNSS (Coffman, 2015).

3. FLOOD MAPPING USING SATELLITE IMAGERY

With the launch of high-resolution satellites and the advent of synthetic aperture radar (SAR) imaging systems that allow for more repetitive coverage, remote sensing is indeed the technology to be adopted in the establishment of an operational flood management system. ERDAS Imagine is used to process the SAR images, while ArcGIS s used to perform GIS spatial analysis and model development. In addition, eCognition is used to classify wet and dry areas. The flood model comprises of two stages of processes, which are flooded areas extraction and assessment of inundated land use types. Preparing the data is the initial step to provide the essential input to the model. The whole process of the flood model workflow is illustrated in Figure 2.

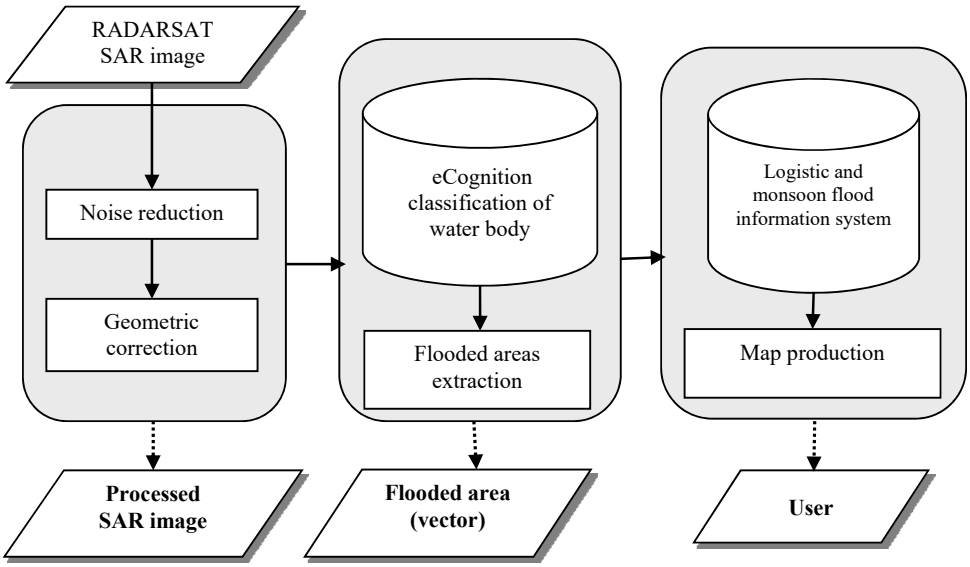

Figure 2: Flood model workflow.

3.1 Application of RADARSAT SAR Images

RADARSAT SAR images are geometrically corrected and registered to Malaysian Rectified Skew Orthomorphic (RSO) for Peninsular Malaysia, and Borneo Rectified Skew Orthomorphic (BRSO) for Sabah and Sarawak. The orthorectification process uses the RADARSAT dry base layer as the reference image. Registration of RADARSAT images is the most time consuming and difficult step, especially the ground control point (GCP) collection for various time series RADARSAT images. However, the time required to register the images can be significantly improved using a set of common well-identified GCPs and a geo-referenced radar image. This data can then be used for image-to-image registration of any new RADARSAT image in future.

3.2 Flooded Areas Extraction

The main input data for the flooded areas extraction includes district boundaries, mountain shadow extent, land use classes and normal water extent. Using the processed SAR image as the input file, the model is performed using eCognition to extract the water extent. The extracted water extent is then masked based on the district boundaries to remove the unwanted areas. Then, the results are converted to vector format to identify and calculate the real flooded areas by district boundaries. Finally, the results are overlaid with district boundaries and normal water extent for flooded areas map production. Based on ground truthing activities and data verification by JPS, the estimated flood map covers 75-85% of actual flood conditions.

3.3 Map Production

The satellite map of the flood is generated using RADARSAT images acquired during flood and dry seasons. ArcGIS was used in the production of the flood map. Water bodies, especially in areas that were submerged can be observed in the image layer. Vector data for roads, flood evacuation centres, district boundaries and names of settlements that are involved the flood are included in the flood map. This map will be submitted to NADMA and other relevant agencies in hardcopy and digital.

4. FLOOD DETAILS AND REAL-TIME INFORMATION EXTRACTION USING DRONE FMV DATA

Based on the generated flood map, NADMA and relevant agencies will examine and identify hotspot areas, and task drones to acquire more detailed and latest information. This information is an important input to the decision-making process to determine the most suitable action plan to be taken.

In this study, a rotary wing drone (quadrotor) equipped with a FMV optical sensor system is used to monitor and collect information in the designated hotspot areas. The recorded FMV data is streamed directly from the drone to the operation command centre for real-time FMV data analysis, which is carried out using TacitView by the drone operators with the support of personnel from NADMA and relevant agencies. In order to maintain the reliability of data streamed to the mobile workstation, a directly wired connection to the drone base station is established to avoid any transmission delays or connectivity problems that usually occur on wireless connections. Figure 3 shows the connection configuration between the drone base station to the FMV live data processing mobile workstation. Optical satellite images and generated flood vector information are uploaded and displayed into TacitView (Figure 4) to enable FMV live data analysis activities to be perform more swiftly and effectively.

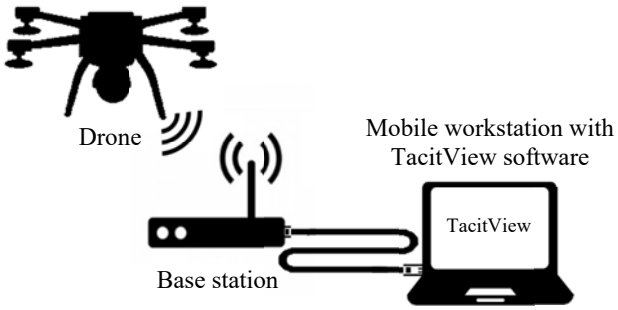

Figure 3: Live FMV data are streamed directly to the mobile workstation through the drone base station.

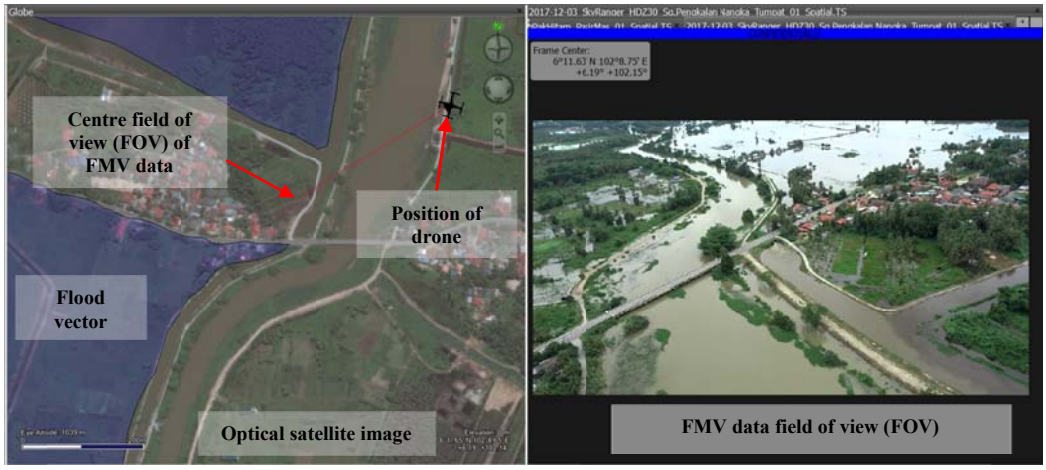

Figure 4: TacitView interface and drone FMV footage.

Generally, the information commonly required by NADMA and relevant agencies during flood event are as follows:

i. Factors that caused the flood overflows;
ii. Factors that caused congestion / bottleneck to the flood water outflows;

iii. Flood condition and water flow pattern; and
iv. Current state of roads that are affected by the floods, especially roads for relief and logistic activities.

This information can be quickly and accurately identified using a combination of remote sensing imagery and FMV drone data, especially for those areas that are difficult to reach. However, the resulting coordinates are dependent on the drone's internal GNSS accuracy, which is sufficient because in emergency situations, decisions should be made within a short period of time (Zhou, 2009; Remondino *et al.*, 2011; Nex & Remondino, 2014; Sun *et al.*, 2016). Figures 5 and 6 show examples of outputs of the call out method analysis made during drone in-flight in designated hotspot areas.

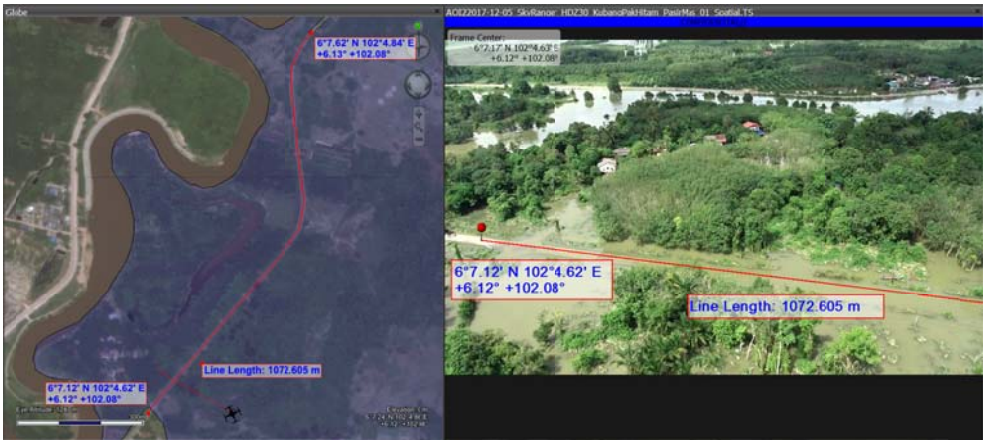

Figure 5: Location and latest condition of roads affected by the flood.

Figure 6: Location of congestion / bottleneck of flood water outflows in the hotspot area.

Based on the provided real-time information by drone FMV data (Figure 5), we able to know the latest condition of roads and estimation length of the roads that have been affected by floods. With this information, disaster management agencies able to determine appropriate action plans, such as finding other access routes to deliver supplies to flood victims.

Furthermore, the coordinates for the locations of congested flood water outflows in hotspot areas can be obtained in real-time by using drone FMV data (Figure 6). With this information, disaster management agencies are able to deploy portable water pumps to increase the flow rate of floodwater out of the stagnant areas to the proper flow channels and increase the number of waterways in hotspot areas in the future.

5. CONCLUSION

The combination of remote sensing satellite imagery and drone FMV data proves to provide the opportunity for fast and precise overview of flooded areas, which delivers very positive impact to the monsoon flood management. NADMA and relevant agencies are able to access to the latest and actual flood situation quickly and accurately as compared to the previous conventional methods. Therefore, the actions taken by the respective disaster management agencies will be more precise and reflect to the root course of the aggravated flood situation. The combination of remote sensing satellite imagery and drone FMV data also has great potential to be utilised in other flood related applications such as post-event disaster damage assessment and flood management infrastructure development plan.

For sustainable monsoon flood management, more research needs to be done in the future in order to develop an integrated system purposely to consolidate flood history information along with other relevant data in order to provide easy and quick access to flood disaster information regardless of time or place. Furthermore, activities for data updating and dissemination to the respective parties can be implemented more swiftly and efficiently.

ACKNOWLEDGEMENTS

The authors acknowledge the support provided by the Malaysian Ministry of Science, Technology, and Innovation (MOSTI), National Disaster Management Agency (NADMA), Department of Irrigation and Drainage (JPS), Malaysia Civil Defence Force (APM), and Malaysian Space Agency (MYSA).

REFERENCES

Alias, N.E., Mohamad, H., Wan, Y.C. & Yusop, Z. (2016). Rainfall analysis of the Kelantan big yellow flood 2014. *J. Teknol.*, **78**: 83-90.

Coffman, P.N. (2015). *Capabilities Assessment and Employment Recommendations for Full Motion Video Optical Navigation Exploitation (FMV-ONE)*. Master Thesis, Information Sciences Department, Naval Postgraduate School, California.

Froment, R. & Below, R. (2020). *CRED Crunch 58 - Disaster Year in Review (2019)*. Centre for Research on the Epidemiology of Disasters (CRED), Brussels, Belgium.

Geospatial World (2013). *UAS in Disaster Management: Real-Time Videos for Emergency Relief*. Available online at: https://www.geospatialworld.net/article/uas-in-disaster-management-real-time-videos-for-emergency-relief (Last access date: 17 September 2020).

Giordan, D., Manconi, A., Remondino, F., & Nex, F. (2017). Use of unmanned aerial vehicles in monitoring application and management of natural hazards. *J Geomat Nat Hazards Risk*, **8**: 1-4.

Hua, A.K. (2015). Monsoon flood disaster in Kota Bharu, Kelantan case study: A comprehensive review. *Int. J. Sci. Eng. Res.*, **3**: 79-81.

Lilian, B. (2017). *Aeryon SkyRanger Drones Help First Responders in Caribbean After Irma*. Available online at: https://unmanned-aerial.com/aeryon-skyranger-drones-help-first-responders-caribbean-irma (Last access date: 17 September 2020).

Mashfiq, K. (2017). *Application of UAV in Emergency Response*. Available online at: http://artsa.gistda.or.th/wp-content/uploads/2017/09/ModA3S4_UAV_In_ER_UNOSAT_ GISTDA.pdf (Last access date: 14 January 2021).

Mott, R. (2011). *Motion Video Exploitation*. Available online at: https://eijournal.com/print/articles/motion-video-exploitation (Last access date: 13 May 2020).

National Disaster Management Agency (NADMA) (2019). *Laporan Tahunan NADMA 2018*. Available online at:

http://www.nadma.gov.my/images/nadma/documents/laporan/Annual_Report_NADMA_18.pdf (Last access date: 10 October 2020).

NATO Standardization Agency (2009). *Standardization Agreement (STANAG), 4609 JAIS (EDITION 3) - NATO Digital Motion Imagery Standard. North Atlantic Treaty Organization (NATO)*. NATO Standardization Agency, Brussels, Belgium.

Nex, F. & Remondino, F. (2014). UAV for 3D mapping applications: A review. *Appl. Geomat.,* **6**: 1-15.

Remondino F., Barazzetti L., Nex F., Scaioni M. & Sarazzi D. (2011). UAV photogrammetry for mapping and 3D modelling – Current status and future perspectives. *Int. Arch. Photogramm. Remote Sens. Spatial Inf. Sci.*, XXXVIII-1/C22: 25-31.

Rester, M., Spruyt, P., De Groeve, T., Van Damme, O. & Ali, A. (2013). *Unmanned Aerial Systems for Rapid Mapping: UASRapidMap 2013*. United Nations Institute for Training and Research Operational Satellite Applications Programme, Geneva, Switzerland

Samsioe, H., Monica Winge, M., Louis Potter, L. & Soesilo, D. (2017). *Unmanned Aerial Vehicles Landscape Analysis: Applications in the Development Context*. United States Agency for International Development (USAID), Arlington, Virginia.

Sani G.D., Gasim M.B., Toriman M.E. & Abdullahi M.G. (2014). Floods in Malaysia: Historical reviews, causes, effects and mitigations approach. *Int. J. Interdiscip. Res. Innov.*, **2**: 59-65.

Sun, J., Li, B., Jiang, Y. & Wen, C. (2016). A camera-based target detection and positioning UAV system for search and rescue (SAR) purposes. *Sensors*, **16**: 1778.

The United Nations Economic and Social Commission for Asia and the Pacific (ESCAP) (2013). *Space Applications for Improving Disaster Management*. Information and Communications Technology and Disaster Risk Reduction Division, Economic and Social Commission for Asia and the Pacific (ESCAP), Bangkok, Thailand.

Zhou, G. (2009). Near real-time orthorectification and mosaic of small UAV video flow for time-critical event response. *IEEE T. Geosci Remote.*, **47**:739-747.

SOLAR IRRADIANCE FORECASTING USING GLOBAL POSITIONING SYSTEM (GPS) DERIVED TOTAL ELECTRON CONTENT (TEC)

Angelin Anthony & Yih Hwa Ho*

Centre for Telecommunication Research & Innovation, Fakulti Kejuruteraan Elektronik & Kejuruteraan Komputer, Universiti Teknikal Malaysia Melaka (UTeM), Malaysia

*Email: yihhwa@utem.edu.my

ABSTRACT

Solar energy is one of the most significant energy sources and the only potential energy source capable of providing the world's required extra energy over the next few decades. Due of its intermittency because of weather variations, the integration of renewable energy (RE), such as solar energy, into the electrical network is a challenge for grid operators. Conversely, the installed capacity of solar photovoltaic (PV) globally continues to rise. In Malaysia, the average monthly daily solar radiation is 4,000-5,000 W/m², with the average monthly sunshine duration ranging from 4 to 8 h. Thus, forecasting is becoming an effective resource for network grid operators to control the output of solar photovoltaic (PV) energy. Solar radiation measurement will decrease when ionosphere total electron content (TEC) decreases. This is because free electrons forming in the ionosphere are strongly dependent on the solar radiation. This study aims to investigate the interaction between TEC and solar irradiance for further use in solar irradiance forecasting. In order to obtain the TEC, GPS data was extracted in order to substitute into the calculations. The interaction between TEC and solar irradiance was done using neural net fitting. The overall correlation coefficient, R obtained is 0.91, which indicates a good fit. In addition, future TEC values were predicted using the auto regressive integrated moving average (ARIMA) and long short-term memory (LSTM) models. The predicted TEC values were further fed into the trained neural network to forecast future solar irradiance. In order to compare the accuracy of model, root mean square error (RMSE) was used to evaluate the results. It was found that the ARIMA model is better for solar irradiance forecasting as it has lower RMSE as compared to the LSTM model.

Keywords: *Global Positioning System (GPS); ionosphere; total electron content (TEC); solar irradiance; time series prediction.*

1. INTRODUCTION

According to a report from the International Energy Agency (IEA), the increase in net renewable electricity capacity additions will be almost 4% higher in 2020 than in 2019. This means that the world is expected to install over 198 GW of renewable energy (RE) capacity this year. Higher additions of wind (+8%) and hydropower (+43%) are expected in 2020, while solar photovoltaic (PV) growth remains stable with more utility-scale PV plants are installed. RE will achieve record expansion in 2021, with almost 218 GW becoming operational (a 10% increase from 2020). With global electricity demand expected to contract this year, the portion of RE in global electricity generation increased and reached 27% in 2020. Electricity generation from renewables will expand by almost 50% in the next five years to almost 9,745 TWh. By 2025, the share of renewables in total electricity generation is expected to be 33%, surpassing coal-fired generation (IEA, 2020a).

Global solar PV capacity additions are expected to reach nearly 107 GW in 2020. Average annual solar PV capacity additions from 2023 to 2025 are expected to range from 130 to 165 GW, accounting for almost 60% of total renewable energy expansion. In the next five years, the generation costs of

utility-scale solar PV are expected to decline another 36%, making PV the least costly way to add new electricity capacity in most countries. The increase in contribution of RE sources into the grid is part of smart grid initiatives. The integration of RE, such as solar energy, into the electrical network is a challenge for grid operators because of its intermittency due to weather variations. Despite this, the installed capacity of solar PV globally continues to increase. Thus, forecasting is becoming an important tool for system grid operators to manage solar PV energy production and satisfy the demand of energy consumers (IEA, 2020b).

Very short-term forecasting, also denoted as intra-hour forecasting or nowcasting, covers forecast horizons from a few seconds to one hour. It is important to assure grid quality and stability, as well as to correctly schedule spinning reserves and demand response (Wan *et al*. 2015). At this time, the main factor causing changes in solar irradiation is the presence of clouds. Cloud generation and movement obey physical rules, but turbulent processes make them appear to be stochastic and very difficult to model (Larson, 2013). Several efforts have been made to understand and predict cloud movement. Bosch & Kleissl (2013) derived cloud speed from data collected at a triplet of sensors at arbitrary position in a PV plant, whereas Chow *et al*. (2015) determined cloud speed and stability using a ground-based sky imaging system. The difficulty of detecting clouds in the Sun region, as well as determining the thickness of clouds has also been reported (Chu *et al.,* 2015; Urquhart *et al.,* 2015). Peng *et al*. (2015) faced the problem of cloud thickness determination using several total sky imagers and established spatio-temporal correlations between them, which proved to be useful.

Nowcasting can be approached via several ways, where models using only endogenous data or meteorological records are dominant. Numerical weather prediction (NWP) is not normally used at this time frame since they lack enough temporal resolution. Information shared from other PV plants has been taken into account in several studies, although for short lead times (less than 15 min) they do not provide satisfactory results due to the low spatial-temporal correlation between plants. It has been found that for short time horizons, developing persistence models is a difficult task (Barbieri *et al.* 2018).

It has been found that solar radiation measurement decreases when the total electron content (TEC) of the ionosphere decreases. This is as the formation of free electrons in the ionosphere strongly depends on the solar radiation (Senapati *et al.* 2020). Lean (2019) used solar irradiance as input to the statistical mode for forecasting the ionosphere's vertical TEC (VTEC). To this end, the interaction between TEC and solar radiation measurement should be further investigated with the objective of forecasting solar radiation precisely by incorporating this parameter. This can be done using a Global Positioning System (GPS) receiver network can provide spatial TEC estimation.

2. METHODOLOGY

2.1 GPS Data Processing

Dual frequency GPS data and solar irradiance measurement were obtained for the location at Universiti Teknikal Malaysia Melaka (UTeM), Melaka, Malaysia (2.314085 °N, 102.318342 °E). The relationship between ionospheric TEC and solar irradiance measurement was investigated for a period of two weeks.

The GPS data was used to calculate the slant TEC (STEC) using the following equation (Ho *et al*. 2019):

$$STEC = \frac{2(f_1 f_2)^2}{K\left({f_1}^2 - {f_2}^2\right)}(P_2 - P_1) \quad (1)$$

where:

f_1 - GPS L1 signal frequency = 1,575.42 MHz
f_2 - GPS L2 signal frequency = 1,227.60 MHz
K - constant value = 40.3
P_1 - code of pseudoranges
P_2 - code of pseudoranges

In order to determine the VTEC, the elevation angle from each satellite was needed as in the following equation (Abdullah *et al*., 2009):

$$VTEC = \left(\frac{STEC - |bR + bS|}{S(E)}\right) \quad (2)$$

where:
bR - receiver bias
bS - satellite bias

$$S(E) = \frac{1}{cos\ x'} \quad (3)$$

with the cos *x'* formula being:

$$cos\ x' = \sqrt{1 + \left(\frac{R_x\ cosx}{R_{x+}h_m}\right)^2} \quad (4)$$

where:
R_x - the mean of radius of Earth
h_m - height of ionospheric layer = 350 km
x - elevation angle of the satellite
x' - $(90^0 - x)$

2.2 Artificial Neural Network (ANN) and Time Series Forecasting

Artificial neural network (ANN) is a machine learning algorithm that allows neurons to learn like a human brain. A neural network consists of input, hidden and output layers. For each layer, there is neuron (also called as node) that is connected in between multi-layer networks. Mathematically, the output of a neuron can be calculated using Equation 5, where x = input, w = weight, b = bias and y = output. Furthermore, different implementation of activation functions, such as sigmoid or hyperbolic tangent sigmoid, can affect the output of the neurons (Grossi & Buscema, 2007). The structure of neuron as shown in Figure 1. In this study, ionospheric TEC is used as the input, x to the ANN, while solar irradiance is used at the output, y.

$$y_j = f\left(\sum_{i=1}^{n} x_i \cdot w_i + b\right) \quad (5)$$

Time series forecasting is a model that forecasts future values based on past values. ARIMA is a time series model that combines autoregression (AR), integration (I) and moving average (MA). ARIMA models that deal with seasonality are known as seasonal ARIMA. Usually, ARIMA models are presented as ARIMA (p, d, q), while seasonal ARIMA models are presented as SARIMA (p, d, q) (Boualit & Mellit, 2017).

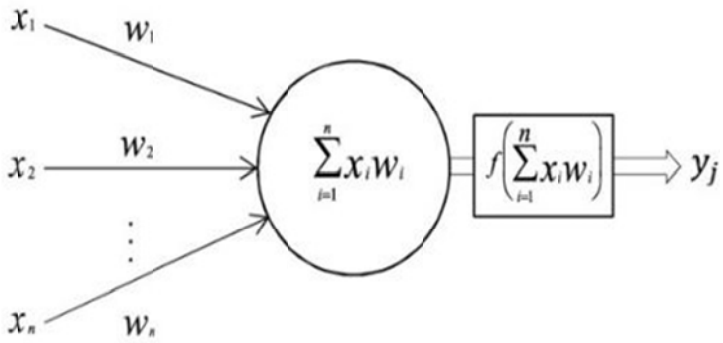

Figure 1: The structure of a neuron (Khatib *et al*., 2012).

The general equation for seasonal ARIMA without constant is as shown in Equation 6 where $\beta_0 =$ intercept, β_1, β_2= linear coefficients, β_{11}, β_{12} = quadratic coefficients, β_{12}= interaction coefficient, X_1, X_2 = parameters, and ε = random error that follows normal distribution with mean of 0.

$$y = \beta_0 + \beta_1 X_1 + \beta_2 X_2 + \beta_{11} {X_1}^2 + \beta_{22} {X_2}^2 + \beta_{12} X_1 X_2 + \varepsilon \quad (6)$$

Long short-term memory (LSTM) is a type of recurrent neural network (RNN) with feedback connections that can learn long-term dependencies between time steps of a sequence data. A LSTM block typically has a memory cell, input gate, output gate and a forget gate, in addition to the hidden state in traditional RNNs. The cell stores values over arbitrary time intervals and the three gates regulate the flow of information into and out of the cell. Figure 2 shows how the weights and biases to the input gate control the extent to which a new value flows into the cell in LSTM block.

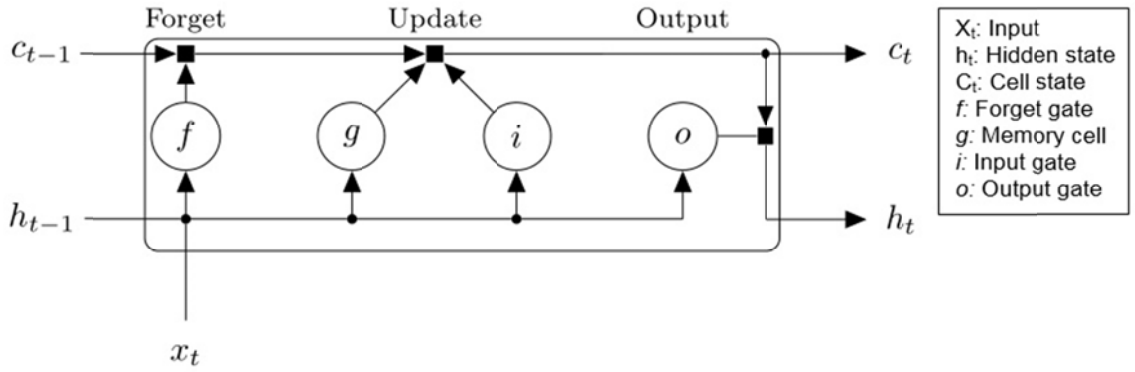

Figure 2: A LSTM block (Hochreiter *et al.* 1997).

4. RESULTS AND DISCUSSION

The TEC and solar irradiance data were trained with a two-layer feedforward network, with a sigmoid transfer function and 10 neurons in the hidden layer, and a linear transfer function in the output layer. The Levenberg-Marquardt backpropagation algorithm is used. This algorithm is used to solve non-linear least squares problems especially in least squares curve fitting (Marquardt, 1963). Its application to neural network training is described in Hagan & Menhaj (1994). Figure 3 shows the regression plots for the network outputs with respect to targets for training, validation and test sets. The output tracks the targets very well for training, testing and validation, with the *R*-value being over 0.91 for the total response.

Both ARIMA and LSTM models were used to predict solar irradiance. In order to compare the performance of these predictions, root mean square error (RMSE) was calculated. RMSE is a metric often used to test the precision of a model's prediction by measuring the differences between the actual and predicted values. From the prediction of TEC using ARIMA and LSTM (Figures 4 and 5), it is found that the RMSE obtained for ARIMA is 0.016212, and 0.041855 for LSTM. As the ARIMA model has lower RMSE, it is a more suitable model for TEC time series prediction.

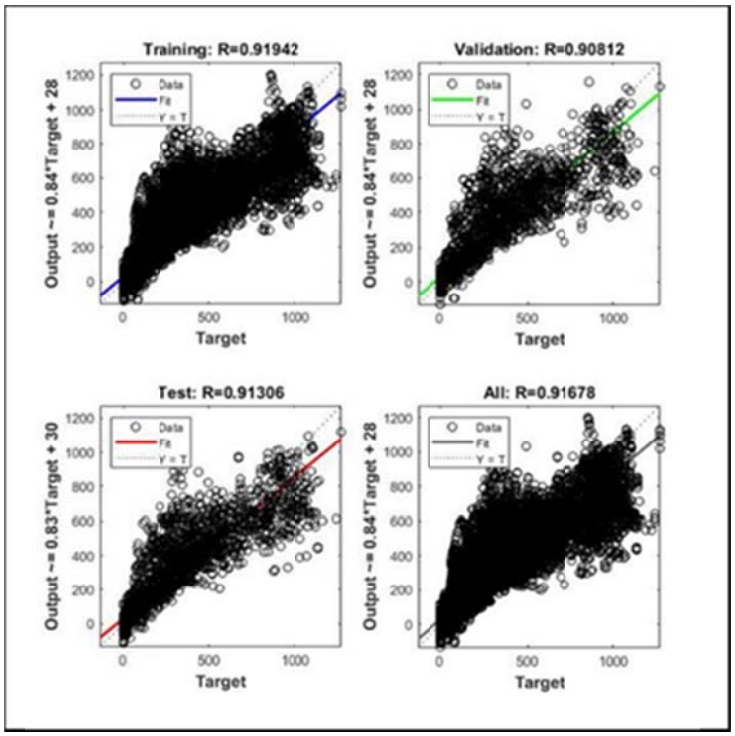

Figure 3: Regression plots for TEC and solar irradiance.

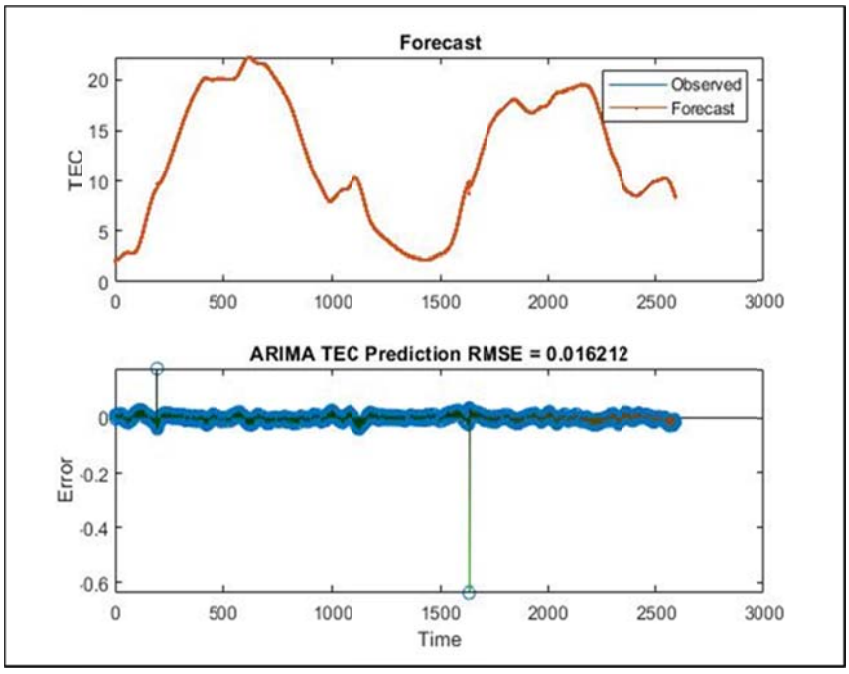

Figure 4: TEC prediction using ARIMA.

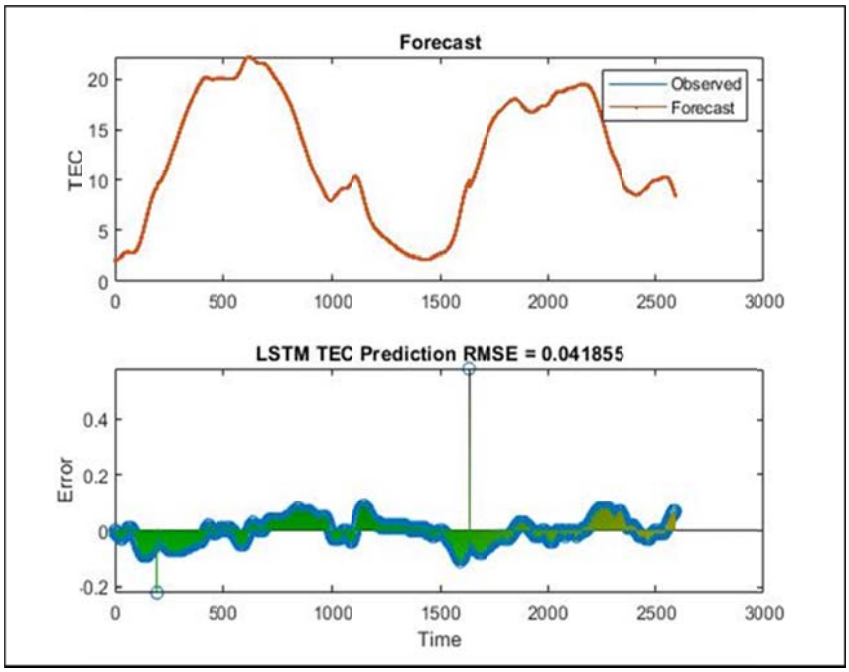

Figure 5: TEC prediction using LSTM.

The predicted TEC using ARIMA and LSTM were fed as inputs into the trained neural network to forecast the solar irradiance. Analysis was done for one hour, three hours and one day ahead forecasting of solar irradiance. Figures 6 - 8 and 9 – 11 show the performance of solar irradiance forecasting using ARIMA and LSTM predicted TEC values respectively.

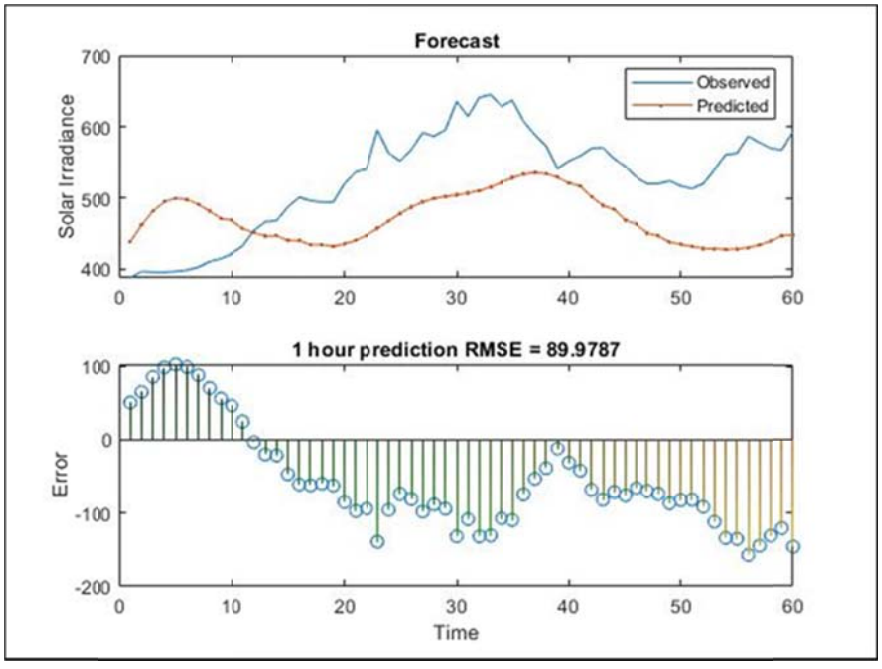

Figure 6: One hour ahead solar irradiance prediction using ARIMA.

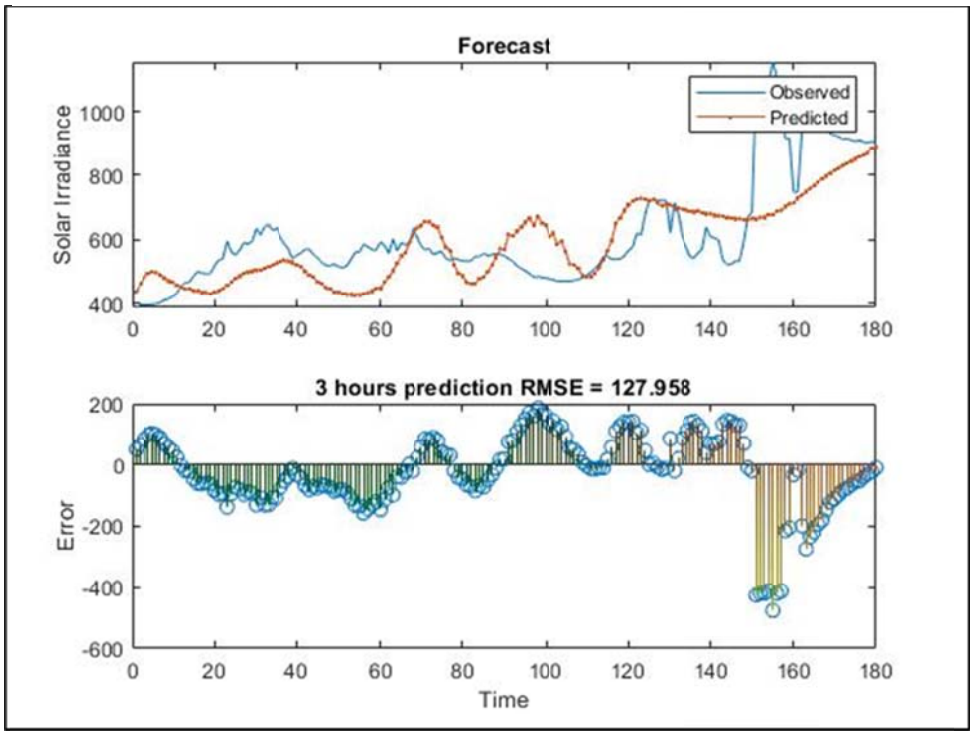

Figure 7: Three hours ahead solar irradiance prediction using ARIMA.

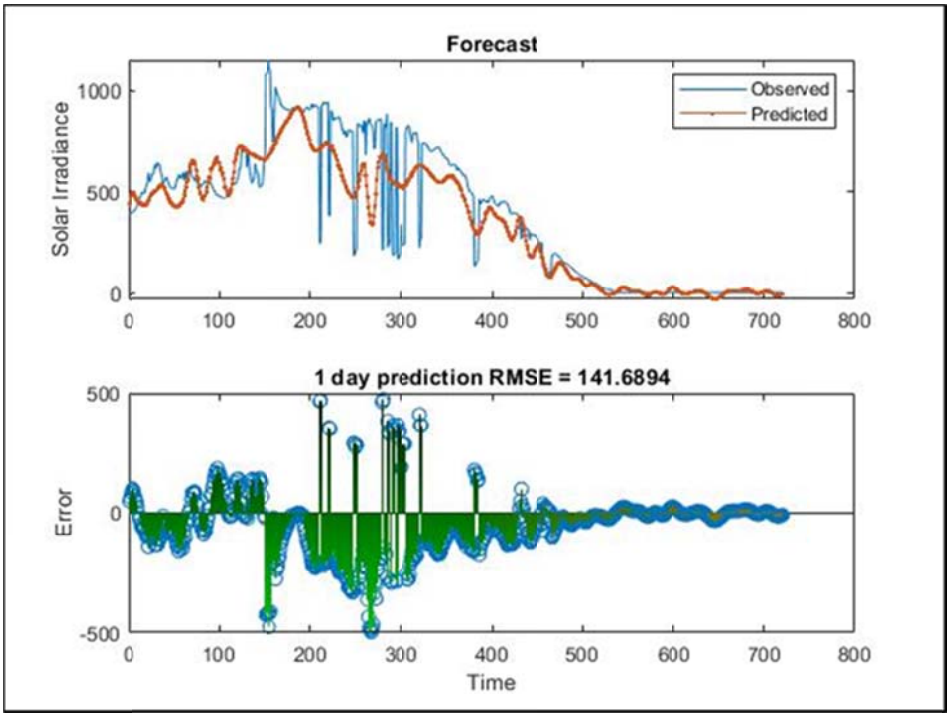

Figure 8: One day ahead solar irradiance prediction using ARIMA.

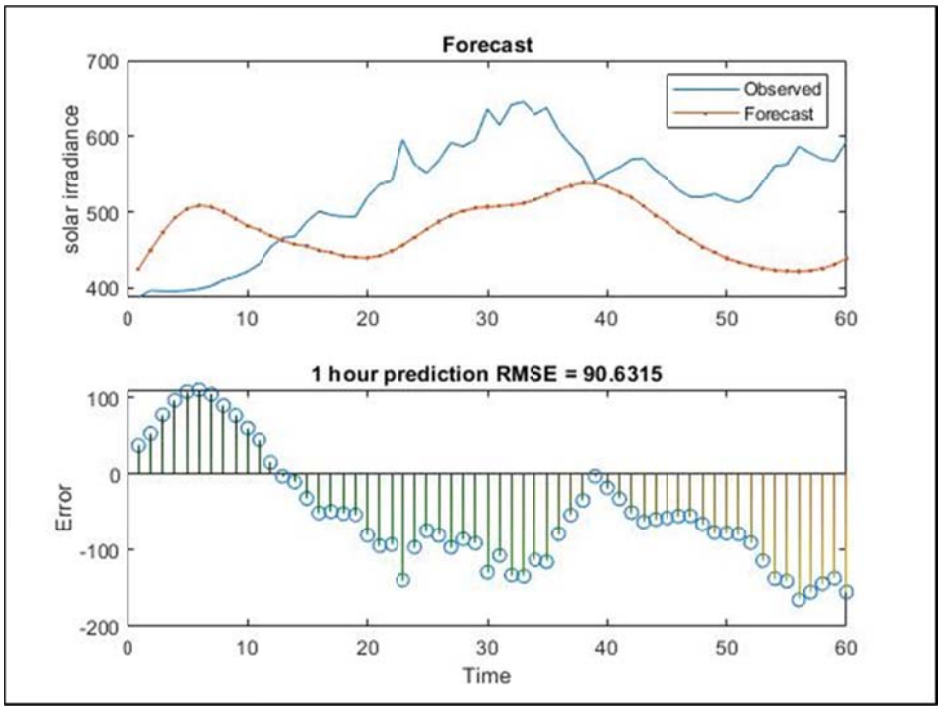

Figure 9: One hour ahead solar irradiance prediction using LSTM.

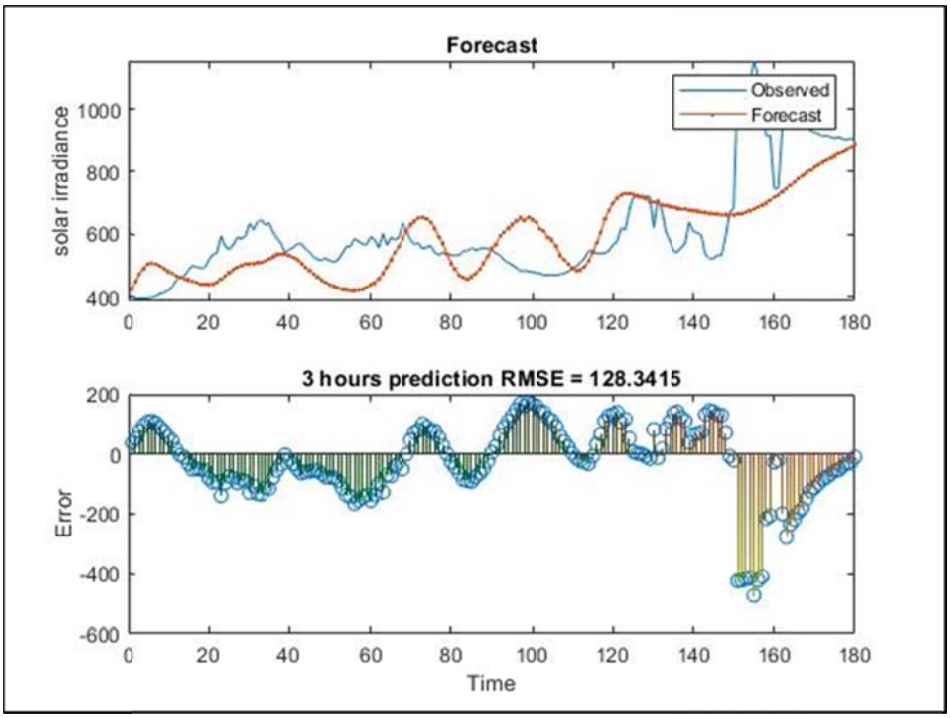

Figure 10: Three hours ahead solar irradiance prediction using LSTM.

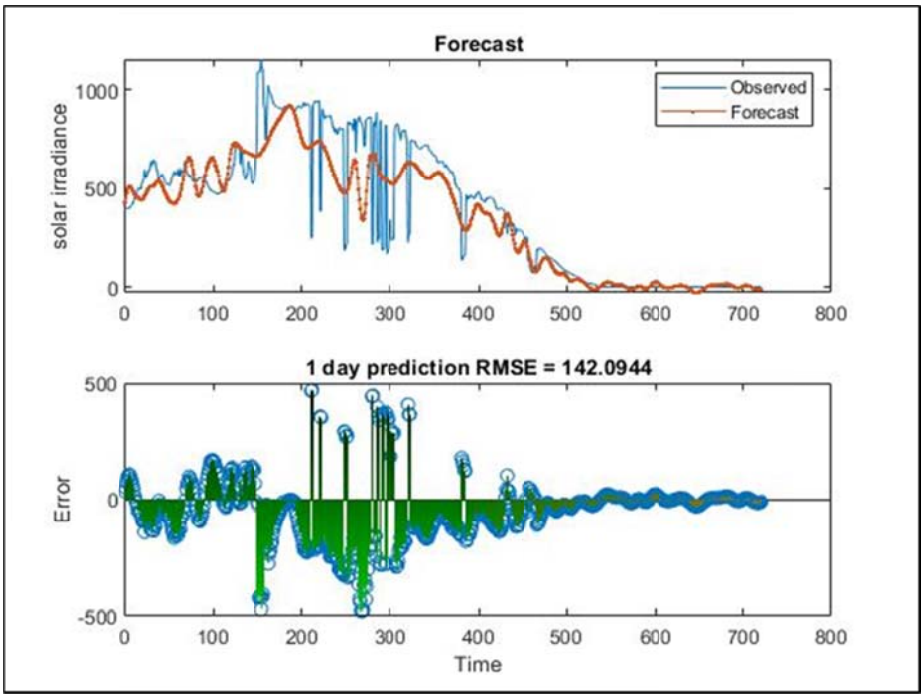

Figure 11: One day ahead solar irradiance prediction using LSTM.

The RMSE values of the two different models were computed and tabulated for one day, three hours and one day ahead for solar irradiance forecasting, as shown in the Table 1. It can be concluded that the RMSE values increased significantly with longer period forecasts for both models. It is found that the ARIMA model had better performance than the LSTM model. This is as all the RMSE values of solar forecasting with the ARIMA model are lower for short- and long-term as compared to the LSTM model.

Table 1: Comparison between solar irradiance forecasting using ARIMA and LSTM predicted TEC values.

Model	Predicted Time	RMSE
ARIMA	One hour ahead	89.9787
	Three hours ahead	127.958
	One day ahead	141.6894
LSTM	One hour ahead	90.6315
	Three hours ahead	128.3415
	One day ahead	142.0944

4. CONCLUSION

In this study, a two-layer feedforward network was trained to forecast solar irradiance with TEC values as the input. The regression analysis showed a very good fit for the model with *R* value of 0.91. ARIMA and LSTM were then used to predict future TEC values. These predicted TEC values were further fed into the trained neural network to forecast future solar irradiances. One hour, three hours and one day ahead solar irradiance forecastings were analysed with both the ARIMA and LSTM model. The results showed that the ARIMA model performed better than the LSTM model in general. However, the reliability of the forecasting model decreased with time.

ACKNOWLEDGEMENT

The authors would like to thank Universiti Teknikal Malaysia Melaka and Ministry of Higher Education Malaysia for funding this research under Fundamentals Grant Scheme (FRGS/2018/FKEKK-CETRI/F00358).

REFERENCES

Abdullah, M, Zain A.F.M, Ho, Y.H. & Abdullah, S. (2009). TEC and scintillation study of equatorial ionosphere: A month campaign over Sipitang and Parit Raja stations, Malaysia. *Am. J. Eng.. Appl Sci.*, **2**: 44–49.

Barbieri, F., Rifflart,C. Vo, B., Rajakaruna, S. & Ghosh, A. (2018). Intra-hour cloud tracking based on probability hypothesis density filtering. *IEEE T. Sustain. Energ.*, **9**: 340-349.

Bosch, J. & Kleissl, J. (2013). Cloud motion vectors from a network of ground sensors in a solar power plant. *Sol. Energy,* **95**: 13–20.

Boualit, S.B. & Mellit. (2016). A. SARIMA-SVM hybrid model for the prediction of daily global solar radiationtime series. *Proc. 2016 IEEE Int. Renew. Sust. Energ. Conf. (IRSEC)*, Marrakesh, Morocco, 14–17 November 2016, pp. 712–717.

Chow, C., Belongie, S., Kleissl, J. (2015). Cloud motion and stability estimation for intra-hour solar forecasting. *Sol. Energ.,* **115**: 645–655.

Chu, Y., Urguhart, B., Gohari, S., Pedro, H., Kleissl, J. & Coimbra, C. (2015). Short-term reforecasting of power output from a 48MWe solar PV plant. *Sol. Energ.*, **112**: 68–77.

Grossi, E. & Buscema, M. (2007). Introduction to artificial neural networks. *Eur. J. Gastroenterol. Hepatol.,* **19**: 1046–1054, 2007.

Hagan, M.T. & Menhaj, M. (1994). Training feed-forward networks with the Marquardt algorithm, *IEEE Trans. Neural Netw. Learn. Syst*., **5**: 989–993.

Ho, Y.H & Leng, Y. P. (2019). Ionospheric earthquake precursor using global positioning system (GPS) data. *Defence S&T Tech. Bull.*, **12**: 281-294.

Hochreiter, S. & Schmidhuber, J. (1997). Long short-term memory. *Neural Comput.,* **9**: 1735–1780.

International Energy Agency (IEA) (2020a). *Renewables 2020: Analysis and forecast to 2025*. Available online at: https://www.iea.org/reports/renewables-2020 (Last access date: 1 Dec 2020).

IEA (International Energy Agency) (2020b). *Solar PV net capacity additions by application segment, 2017-2022*. Available online at: https://www.iea.org/reports/renewables-2020/solar-pv (Last access date: 1 Dec 2020).

Khatib, T.,Mohamed, A., Sopian, K. & Mahmoud, M. (2012). Solar energy prediction for Malaysia using artificial neural networks, *Int. J. Photoenergy*, **2012** (16).

Larson, V.E. (2013). Forecasting solar irradiance with numerical weather prediction models. *In* Kleissl, J. (Eds), *Solar Energy Forecasting and Resource Assessment*. Academic Press, Elsevier, Cambridge, Massachusetts.

Lean, J. L. (2019). One-to 10-day forecasts of total electron content using a statistical model. *Space Weather*, **17**: 313-338.

Marquardt, D. (1963). An algorithm for least-squares estimation of nonlinear parameters. *SIAM J. Appl. Math.*, **11**: 431–441.

Peng, Z., Yu, D., Huang, D., Heiser, J., Yoo, S. & Kalb, P. (2015). 3D cloud detection and tracking system for solar forecast using multiple sky imagers. *Sol. Energ.,* **118**: 496–519.

Senapati, B., Huba, J.D., Kundu, B., Gahalaut, V.K., Panda, D., Mondal, S.K. & Catherine, J.K. (2020). Change in total electron content during the 26 December 2019 solar eclipse: Constraints from GNSS observations and comparison with SAMI3 model results. *J. Geophys. Res. Space Phys.,* **125**: e2020JA028230.

Urquhart, B., Kurtz, B., Dahlin, E., Ghonima, M., Shields, J. & Kleissl, J. (2015). Development of a sky imaging system for short-term solar power forecasting. *Atmos. Measure. Tech*. **8**: 875–890.

Wan, C., Zhao, J., Song, Y., Xu, Z., Lin, J. & Hu, Z. (2015). Photovoltaic and solar power forecasting for smart grid energy management. *CSEE J. Power Energy Syst*. **1**: 38-46.